2012-10-25

An Atomic Source of Quantum Light

MacRae, Andrew

UNIVERSITY OF CALGARY

An Atomic Source of Quantum Light

by

Andrew John MacRae

A THESIS

SUBMITTED TO THE FACULTY OF GRADUATE STUDIES

IN PARTIAL FULFILLMENT OF THE REQUIREMENTS FOR THE

DEGREE OF DOCTOR OF PHILOSOPHY

DEPARTMENT OF PHYSICS AND ASTRONOMY

INSTITUTE FOR QUANTUM INFORMATION SCIENCE

CALGARY, ALBERTA

October, 2012

Abstract

This thesis presents the experimental demonstration of an atomic source of narrowband nonclassical states of light. Employing four-wave mixing in hot atomic Rubidium vapour, the optical states produced are naturally compatible with atomic transitions and may be thus employed in atom-based quantum communication protocols.

We first demonstrate the production of two-mode intensity-squeezed light and analyze the correlations between the two produced modes. Using homodyne detection in each mode, we verify the production of two-mode quadrature-squeezed light, achieving a reduction in quadrature variance of 3 dB below the standard quantum limit.

Employing conditional detection on one of the channels, we then demonstrate the generation of single-photon Fock states as well as controllable superpositions of vacuum and 1-photon states. We fully characterize the produced light by means of optical homodyne tomography and maximum likelihood estimation. The narrowband nature of the produced light yields a resolvable temporal wave-function, and we develop a method to infer this wave function from the continuous photocurrent provided by the homodyne detector.

The nature of the atomic process opens the door to a new direction of research: generation of arbitrary superpositions of collective atomic states. We perform the first proof-of-principle experiment towards this new field and discuss a proposal for extending this work to obtain full control over the collective-atomic Hilbert space.

Table of Contents

List of Tables

List of Figures

Citations to Previously Published Work

Parts of Chapter 1 have been published as

> "Matched Slow Pulses Using Double Electromagnetically Induced Transparency", A. MacRae, G. Campbell and A. I. Lvovsky, *Optics Letters* **33**(22): 2659 - 2661 (2008)

and as

> "Simultaneous Slow Light Pulses With Matched Group Velocities via Double-EIT", A. MacRae, G. Campbell, A. Ordog and A. I. Lvovsky, *Proceedings of Quantum Communication, Measurement and Computing* **1110**(1): 269 - 272 (2008)

Parts of Chapter 3 have been published as

> "Versatile Wideband Balanced Detector for Quantum Optical Homodyne Tomography", R. Kumar, E. Barrios, A. MacRae, E. Cairns, E. H. Huntington and A. I. Lvovsky, *Optics Communications* (2012), DOI:10.1016/j.optcom.2012.07.103

Parts of Chapter 4 have been published as

> "Versatile Digital Ghz Phase Lock for External Cavity Diode Lasers", J. Appel, A. MacRae and A. I. Lvovsky, *Measurement Science and Technology* **20**(5): 055302 (2009)

Parts of Chapter 5 have been published as

> "Tomography of a High-Purity Narrowband Photon From a Transient Atomic Collective Excitation", A. MacRae, T. Brannan, R. Achal, and A. I. Lvovsky, *Physical Review Letters* **109** 033601 (2012)

and

"A Monolithic Filter Cavity for Experiments in Quantum Optics", P. Palittapongarnpim, A. MacRae and A. I. Lvovsky, *Review of Scientific Instruments* **83** 066101 (2012)

Parts of Chapter 6 have been published as

"Quantum-Optical State Engineering up to the Two-Photon Level", E. Bimbard, N. Jain, A. MacRae and A. I. Lvovsky, *Nature Photonics* **4**(4): 243 - 247 (2010)

List of Acronyms

4WM: Four-Wave Mixing

AOM: Acousto-Optic Modulator

APD: Avalanche Photodiode

BBO: Beta-Barium Borate

BHD: Balanced Homodyne Detection

CCD: Charge-Coupled Device

CSE: Collective Spin Excitation

CMRR: Common mode rejection Ration

DLCZ protocol: Duan Lukin Cirac Zoller protocol

ECDL: External Cavity Diode Laser

FSR: Free Spectral Range

FWHM: Full Width at Half Maximum

GEM: Gradient Echo Memory

OHT: Optical Homodyne Tomography

(O)PLL: (Optical) Phase-Locked Loop

PPKTP: Periodically Poled Potassium Titanyl-Phosphate

SPCM: Single Photon Counting Module

SPDC: Spontaneous Parametric Down Conversion

SQL: Standard Quantum Limit

TEM mode: Transverse ElectricoMagnetic Mode

TLA: Three-Letter Acronym

TMSS: Two Mode Squeezed State

Acknowledgements

Approximately 2190 days ago, having finished my undergraduate studies in physics, I was faced with the question of what to do next. After some thought, I realized that I wasn't finished learning physics and that I wanted to somehow keep going. I had heard rumours of something called "grad school" in which one can do physics all day, and get paid to do so[1]. Somewhat hesitantly, I began to stumble across the internet in search of such a school and came across the group of Dr. Alex Lvovsky. After some intense negotiation and a rigorous series of tests, Alex decided to admit me as a masters student. Over the next two years I learned about what it is that physicists do, tried to mimic this behaviour myself, wound up with a thesis on "Double Electromagnetically Induced Transparency" and thought, "well that was fun, what now?" That old feeling of not quite being done crept back and I decided to stay on for a PhD, where I performed the work described in what follows. Here now, finishing up this chapter in my prolonged relationship with physics, that old feeling is back again and so now it's off to a postdoc.

I couldn't have even considered grad school without the support of my family and friends. I first would like to thank my beautiful wife Sheralyn for her selfless support of the somewhat selfish goals of a grad student. Sheralyn encouraged my every step, provided council, wisdom, and balance in the face of my perpetual over-thinking, and to top it off, has been an incredible mother to our son. Sheralyn, thank you for being the solid foundation of our growing little family. Best PhD wife ever. Our son Jackson who came onto the scene roughly at the start of my degree has been a source not only of sleep deprivation, but also of joy and inspiration and is a constant reminder that there is far more to life than work. The local support of Sheralyn and Jackson has been

[1] As it turns out, the primary activity in grad school is the ritual consumption of dangerously high levels of $C_8H_{10}N_4O_2$, the actual work being done in between doses.

augmented by our remote team in Victoria. The list of amazing family and friends is too long to practically list, but being highly impractical by nature, I will attempt a partial list anyway: Thank you Mom and Dad (one day I hope your financial investment in this endeavour will yield a high return), Alex, Heather, Catherine and Paul, Grandmas Margaret and Vera, Grandpas Ian and Art, the HOH (Paul, Asma, Raven, Sage, Shaq and Kele), Lorretta and Caressa, Pelter Place (Marianne, Gary, Katherine Jr. Henry and Marilyn), everyone at Fraser Lake, Pelter Place's Chilean regiment (Katherine and Diego), Aunts: (Holly, Mary, Laurie, Donna, Melody, and Nhi), Uncles: (Alistair, John, Marty, Manolo, Pat, and Peter), Jesse, Chrissy, Fleetwood, Jim, Conner, Tim, Logan, Still, Mil, John Gordon, and the long list of other friends made along the way.

Having mentioned the external department, I now turn to the internal team. First, thank you to my supervisor Alex who provided guidance and direction along the way. Throughout my grad studies I have slowly transitioned from blindly following his wisdom to a healthy skeptical distrust of his suggestions, only to find that after all, he was almost always right. I have had amazing coworkers and mentors in the Lvovsky group. Alphabetically, these are Anna, An-Ning, Boris, Chris F, Chris H, Connor, Dallas, Dmitry, Eden, Erick, Erwan, Jürgen, Katanya, Geoff, Matt, Michael, Mirko, Nitin, Pan, Ranjeet, Roshan, Ryan, Sun Youn, Simon, Travis. I also had the benefit at working at the very active Institute for Quantum Information Science which allowed me to interact with the top caliber physicists working here. Thanks Barry, Christoph, Karl-Peter, and Wolfgang for often challenging and always beneficial conversations.

Finally, thank you to the teachers that inspired me to study physics. Without your energy and enthusiasm, I would never have discovered the pure joy of learning how things work.

For Sheralyn, Jackson, and our family

Chapter 1

Introduction

This thesis describes a new method of generating narrow bandwidth non-classical light. What it means for light to be non-classical will be explained in detail in chapter 2, but for now suffice it to say that the defining non-classical light state is that of the single photon, a Bosonic particle representing a discrete quantum of energy. The photon has always been a controversial [2] and fundamentally interesting state owing, among other properties, to its ability to distribute a highly non-local quantum state over great distances. The famous EPR paradox, of Einstein Podolsky, and Rosen [3] was reformulated [4] and tested [5] in terms of photons. The 1956 discovery of photon anti-bunching by Hanbury Brown and Twiss [6] initiated the concept of characterizing a state from photon statistics and opened the field of quantum optics, although somewhat ironically, since the effect can be fully explained classically. Single photon indistinguishability led to quantum interference effects such as the Hong Ou Mandel dip [7] and counterfactual interaction free measurements [8]. The concept of photon bunching led to the concept of the squeezed states which overcome the limit placed by the Heisenberg uncertainty principle, on the minimum fluctuations allowed for a particular quadrature. In addition, squeezed states can exhibit non-locality in the original sense studied by EPR [9].

In the past few decades, nonclassical light has also become a subject of considerable practical interest. The increased precision possible with squeezed states allowed the possibility of increasingly sensitive atomic time standards [10] and ultra-precise interferometry with application to gravitational wave detection [11]. Another application has come with the advent of quantum communication and computing. It was realized that Moore's law describing the number of transistors which can be placed onto an integrated circuit [12]

must one day fail as the required transistor size approaches atomic dimensions. At this scale, a quantum mechanical description of the circuit elements is required.

The concept of using the laws of quantum mechanics to enhance quantum computation dates back to Feynman who suggested it as a method of overcoming the complexity of simulating quantum systems [13]. Modern day quantum computing processes information using elements of a two-dimensional Hilbert-space known as qubits instead of conventional bits. A good candidate for a qubit is the photon, encoded in one of its degrees of freedom such as polarization or time. Optical qubits can travel over long distances without interacting with its environment. As an added bonus, it does so at the speed of light.

While a quantum computer will not likely ever act as a substitute to a conventional (classical) computer, it could greatly outperform a classical computer for several specific operations such as quantum simulation, database searching, and integer factoring [14]. The last operation is of particular relevance since it would compromise standard RSA encryption. The field of quantum communication solves the potential problem caused by quantum computing by allowing the transfer of a cryptographic key which be shared among two parties with unconditional security. The ability of an optical qubit to travel quickly over long distances places non-classical light at the heart of these applications.

A fundamental difficulty plaguing optical quantum information processing lays in storing, retrieving, and manipulating, the involved states. The 'selling point" that the optical qubit does not interact with other light while travelling creates a challenge, since computing often requires the manipulation of one qubit conditioned on the state of the other. One way around this is to engineer non-linear interactions with atoms that mediate the cross-talk between optical fields, which has been at the focus of much our previous work [15]. Since light-matter coupling generally is mediated by an electronic transition with a finite bandwidth $\Delta\nu$, the bandwidth of the qubit must have comparable

bandwidth and have central frequency equal to that of the atomic resonance. Typical bandwidths range from 10 MHz for bare atoms to several GHz for solid state materials. For classical communication, one generally wants as large a bandwidth as possible in order to transfer maximal information. In contrast for quantum communications, the requirement of compatibility with atoms necessitates a source with a narrow spectral band, on the order of atomic line-widths.

Much of the early progress in generating non-classical light came from a non-linear optical effect known as spontaneous parametric down conversion (SPDC) which efficiently generated single photons [16], and entangled photon pairs [17]. A drawback of this method was that the light produced was not compatible with atomic transitions having typical bandwidth $\Delta\nu_{\text{SPDC}} \approx 10^6 \Delta\nu_{\text{atom}}$. In order to obtain light of suitable bandwidth several approaches have been taken.

SPDC light has been spectrally filtered down to a suitable bandwidth but at the cost of greatly reducing the number of emitted photons per unit time[1] [19]. From this, a figure of merit known as the "spectral brightness" $S(\nu)$ emerged quantifying the intrinsic narrowness of the source. $S(\nu)$ is typically stated in terms of number of emissions, per second, per MHz of bandwidth. By placing the SPDC process in an optical cavity, non-classical light sources of very high spectral brightness have been realized [20, 21]. Employing a third-order nonlinear effect known as four-wave mixing (4WM) in optical fibers has also resulted in a high spectral brightness source [22]. Each of the above are examples of so called heralded sources based on correlated two-photon emission. Detection of one photon of the pair heralds the existence of the other, but the pair generation itself is probabilistic. In contrast, on-demand photon sources, acting as a "photon pistol" have been produced using spatially confined semi-conductor devices known as quantum dots [23], but with relatively low spectral brightness and low collection efficiency.

[1] This has been partially overcome by forming a waveguide-based SPDC system [18]

Perhaps the most natural solution to generating quantum light which is compatible with atoms is to use identical atoms to produce this light, which is the approach taken in this work. Indeed the first demonstration of squeezed light (see chapter 2) was generated with four-wave mixing in atoms by Slusher *et al*[24], but this accomplishment was soon overshadowed by SPDC which produced a higher degree of squeezing and was plagued with much less noise [25]. More recently, the DLCZ protocol for long distance quantum communication (see section 6.3.1) led to the experimental demonstration of an atom-based, on-demand photon source by the groups of J. Kimble and M. Lukin [26, 27]. This was followed by a series of studies of this system by the group of S. Harris [28, 29]. Placing the ensemble of atoms in a high finesse optical cavity, a photon source of unprecedented spectral brightness was demonstrated by the Vuletic group [30]. Coming full circle since the 1986 work of Slusher *et al*, the group of P. Lett demonstrated the efficient generation of squeezed light using 4WM in atoms comparable to that of SPDC [31]. This atomic source had the additional benefit of wide spatial bandwidth allowing for the generation of entangled images [32].

The above photon sources inferred the purity of the generated light using photon statistics conditioned on the arrival of the light. Such statistical methods work well if the detected state is assumed *a priori* to belong to a restricted Hilbert space, but owing to losses and extra noise, this is often not the case [33]. For example, these methods can determine the quality of a single photon state provided that it is produced, but do not infer the probability of generating the state in the first place. By employing a technique known as optical homodyne tomography (see chapter 3), the full density matrix of the light state may be measured, including the probability of its generation. This has been accomplished for SPDC sources [19] and atomic based squeezed states [34, 35] but prior to this work, not for atom-based photon sources.

The method of homodyne tomography is especially important for characterizing more

complex quantum optical states. For example, the recent demonstration of an arbitrary optical "qutrit" $\alpha|0\rangle + \beta|1\rangle + \gamma|2\rangle$ relied heavily on OHT. In this experiment, the SPDC source was combined with auxiliary fields before detection resulting in a controllable superposition of 0, 1, and 2 photons [36]. Verification of the successful production of the desired state, required full knowledge of the measured density matrix which could not be obtained by photon statistics alone.

The generation of non-classical light using atomic ensembles opens up a new possibility: the engineering of atomic superposition states. The on-demand, "photon gun character of the DLCZ protocol mentioned earlier is perhaps slightly dishonest: in order to shoot the photon gun, one must first load it. This loading is accomplished by probabilistically creating a single collective spin excitation (CSE) - that is a single excitation shared across the entire ensemble. After this procedure however, one can in principle produce a photon on demand, any time later[2] by converting the CSE into a single photon. By performing conditional measurements during the loading procedure, a superposition of CSEs may be created, akin to [36]. The collective state of the atomic ensemble could then be written out optically, and measured via OHT. This new horizon has applications in quantum metrology as well as a fundamental study of the interplay between analogous Hilbert spaces of optical and collective atomic excitations.

This thesis is organized as follows: In chapter 2 we provide some basic definitions of the non-classical light studied in this work and give an overview of criteria for labelling a measured state as non-classical. In chapter 3, we describe the method of measuring the quantum state of light employed in this work and describe an iterative algorithm for reconstruction the density matrix from a set of experimental data. Chapter 4 describes our experimental characterization of our source of non-classical light in terms of classical gain, and non-classical properties such as intensity and quadrature squeezing. In chapter

[2]In practice, the ensemble decoheres over some characteristic time, after which the loading procedure must be restarted.

5, we describe the production of high quality narrow-band single photons compatible with atomic Rubidium, and introduce several new methods for inferring the temporal waveform of the produced photons. Finally, chapter 6 presents our progress towards manipulating arbitrary superposition states of a collective atomic ensemble.

Chapter 2

Nonclassical Light

2.1 Quantum Light

Throughout history, light has been considered to be wave-like, particle-like, and in the past hundred years or so, both simultaneously. The wave-particle duality of quantum objects remains a conceptual obstacle to an intuitive picture of their behaviour, but quantum mechanics provides a sound formalism which allows us to calculate physically relevant quantities precisely and thus in some sense forgo the need for an intuitive picture. Quantum optics provides a quantum mechanical description of the electromagnetic field and yields a toolkit for working with light as a quantum object.

Recall that for classical electromagnetism, we can define a spatio-temporal mode $u(\mathbf{x}, t)$ which provides a complete description of the field. A simple example of such a mode is a plane wave of some polarization[1] $u(\mathbf{x}, t) = e^{i(\mathbf{k}\cdot\mathbf{x}-\omega t)}$. More complex modes can be written as a sum of these plane wave modes using the Fourier transform. The quantum state of a single mode[2] of the electromagnetic field is mathematically equivalent to that of the quantum simple harmonic oscillator (QSHO) and we can associate an annihilation operator $\hat{a}$ with a given mode having Hamiltonian:

$$\hat{H} = \hbar\omega \left(\hat{a}^\dagger \hat{a} + \frac{1}{2} \right). \tag{2.1}$$

We can thus identify well-known states of the QSHO from elementary quantum theory

[1] A plane wave however, is unphysical in that a monochromatic beam implies an infinite temporal width via the Fourier transform and infinite transverse extent since diffraction increases with decreasing beam width (see appendix C). Experimentally, a laser beam propagating within its Rayleigh range is a good approximation of a plane wave.

[2] A state is said to be single mode with respect to a given mode decomposition if all modes but one in this decomposition are described by the vacuum state [37] (see sections 2.2 and 2.4).

and explore the optical realization of these states.

2.2 Quantum States of Light

2.2.1 Quadrature States

Although the creation and annihilation operators are of fundamental importance to the theory of quantum optics, they are not Hermitian and therefore not physically observable quantities. We can however, use them to form the Hermitian quadrature operators:

$$\hat{X} = \frac{\hat{a}^\dagger + \hat{a}}{\sqrt{2}} \tag{2.2}$$

$$\hat{P} = i\frac{\hat{a}^\dagger - \hat{a}}{\sqrt{2}} \tag{2.3}$$

which represent the physically observable quadratures of the quantum field. The eigenstates of the quadrature operators[3] are in turn defined such that: $\hat{X}\,|X\rangle = X\,|X\rangle$, $\hat{P}\,|P\rangle = P\,|P\rangle$.

Rewriting the basic Hamiltonian (2.1) in terms of the quadrature operators leads to the expression:

$$\hat{H} = \frac{1}{2}\hbar\omega\left(\hat{X}^2 + \hat{P}^2\right). \tag{2.4}$$

From the canonical commutation relation

$$\left[\hat{a}, \hat{a}^\dagger\right] = 1 \tag{2.5}$$

we find $\left[\hat{X}, \hat{P}\right] = i$ and thus $\hat{X}$ and $\hat{P}$ exhibit the uncertainty relation:

[3]Technically, these quadrature states are not normalizable and belong to the so-called rigged Hilbert space [38] but are included here owing to their mathematical convenience. For example, they form the quadrature wave-functions $\psi(x) \equiv \langle X|\psi\rangle$ which *are* physically measurable and are of high relevance to this work.

$$\left\langle \Delta X^2 \right\rangle \left\langle \Delta P^2 \right\rangle \geq \frac{1}{4}. \tag{2.6}$$

Any state for which equality holds in the above relation is known as a minimum uncertainty state.

2.2.2 Fock States

We define the number operator as

$$\hat{n} \equiv \hat{a}^\dagger \hat{a} \tag{2.7}$$

which represents a physical observable corresponding to the number of excitations of the field. The eigenstates of the number operator are known as *Fock states* $|n\rangle$ defined for $n \geq 0$. The Fock states form an orthonormal basis

$$\langle m|n\rangle = \delta_{mn} \tag{2.8}$$

and form the canonical basis for representing arbitrary quantum optical states in this work. The creation and annihilation operators acting on Fock states add and remove an excitation from the field respectively via:

$$\begin{aligned} \hat{a}^\dagger|n\rangle &= \sqrt{n+1}|n+1\rangle \\ \hat{a}|n\rangle &= \sqrt{n}|n-1\rangle \ldots n > 0 \\ &= 0 \ldots n \leq 0 \end{aligned} \tag{2.9}$$

From the Hamiltonian (2.1) we see that each excitation has energy $\hbar\omega$ and the vacuum state of the field $|0\rangle$ has non-zero energy $\hbar\omega/2$.

The quadrature expectation value for any Fock state is identically zero[4] and the variance is then[5]

$$\left\langle \Delta X^2 \right\rangle = \left\langle \Delta P^2 \right\rangle = \langle n| \, \hat{n} + 1/2 \, |n\rangle = n + \frac{1}{2}. \tag{2.10}$$

Note that the Fock states obey the Heisenberg uncertainty relation, with equality holding only for the vacuum state $|0\rangle$.

In the following sections it will be useful to express the wave-function of a Fock state in a particular basis. In the quadrature basis they are [39]:

$$\psi_n(X) = \langle X|n\rangle = \frac{e^{-\frac{X^2}{2}}}{\sqrt{2^n n! \sqrt{\pi}}} H_n(X) \tag{2.11}$$

where $H_n(X)$ is the Hermite polynomial of order n.

2.2.3 Coherent States

Classically, we expect that the mean quadratures of a harmonic oscillator evolve in time as[6] $\left\langle \hat{X}(t) \right\rangle = \hat{X}(0)\cos(\omega t) + \hat{P}(0)\sin(\omega t)$ and similarly for $\left\langle \hat{P}(t) \right\rangle$. Fock states certainly do not fit this description since the mean quadrature vanishes at all times. We then seek a pseudo-classical quantum optical state which behaves like a harmonic oscillator in the classical limit. Such a state was discovered by Schrödinger [40], fully described in terms of quantum optics by Glauber [41], and is known as a *coherent state*. Formally, a coherent state is defined as an eigenstate of the annihilation operator:

$$\hat{a} \, |\alpha\rangle = \alpha \, |\alpha\rangle \tag{2.12}$$

where α is a complex number describing the amplitude and phase of the state. The coherent state has several important properties which are of relevance to this work.

[4] $\langle n| \, \hat{a} \pm \hat{a}^\dagger \, |n\rangle = \sqrt{n} \, \langle n|n-1\rangle \pm \sqrt{(n+1)} \, \langle n|n+1\rangle = 0$

[5] Using $\left(\hat{a} \pm \hat{a}^\dagger\right)^2 = \hat{a}^2 + (\hat{a}^\dagger)^2 \pm (\hat{a}\hat{a}^\dagger + \hat{a}^\dagger\hat{a}) = \hat{a}^2 + (\hat{a}^\dagger)^2 \pm (2\hat{n} + 1)$.

[6] Where, for example $\hat{X}$ is the rescaled position $m\omega x$ and $\hat{P}$ is the classical momentum p.

First, in contrast to the Fock states, coherent states do not contain a definite photon number, We can express a coherent state in the Fock basis as

$$|\alpha\rangle = e^{-\frac{|\alpha|^2}{2}} \sum_{n=0}^{\infty} \frac{\alpha^n}{\sqrt{n!}} |n\rangle . \tag{2.13}$$

from which we see the photon number probability follows a Poissonian distribution. The mean photon number of a coherent state is:

$$\langle n \rangle_\alpha = \langle \alpha | \hat{a}^\dagger \hat{a} | \alpha \rangle = \alpha^* \alpha \langle \alpha | \alpha \rangle = |\alpha|^2 \tag{2.14}$$

and the photon number variance is[7]:

$$\left\langle \Delta n^2 \right\rangle = |\alpha|^2 . \tag{2.15}$$

Note that the relative uncertainty in photon number decreases monotonically as the mean photon number increases: $\langle \Delta n \rangle / \langle n \rangle = 1/\sqrt{\langle n \rangle}$ which one expects for a classical beam which has a does not experience intrinsic intensity fluctuations. Finally, coherent states are minimum uncertainty states satisfying equality in equation 2.6:

$$\left\langle \Delta \hat{X}^2 \right\rangle_{|\alpha\rangle} = \frac{1}{2} \tag{2.16}$$

meaning that the coherent states can be seen as a vacuum state which has been displaced in phase space. To this end, one can write a coherent state in terms of the displacement operator as $|\alpha\rangle = \hat{D}(\alpha) |0\rangle$, where:

$$\hat{D}(\alpha) = \exp\left(\alpha \hat{a}^\dagger - \alpha^* \hat{a}\right) . \tag{2.17}$$

$\hat{D}(\alpha)$ has the following properties [39]:

[7] $\langle \hat{n}^2 \rangle - \langle \hat{n} \rangle^2 = \langle \hat{a}^\dagger \hat{a} \hat{a}^\dagger \hat{a} \rangle - \langle \hat{a}^\dagger \hat{a} \rangle^2 = \langle \hat{a}^\dagger \hat{a}^\dagger \hat{a} \hat{a} + \hat{a}^\dagger \hat{a} \rangle - \langle \hat{a}^\dagger \hat{a} \rangle^2 = |\alpha|^4 + |\alpha|^2 - |\alpha|^4 = |\alpha|^2$

$$\begin{aligned} \hat{D}(\alpha)^{-1} &= \hat{D}(-\alpha) \\ \hat{D}(\alpha)^{\dagger} \hat{a} \hat{D}(\alpha) &= \hat{a} + \alpha. \end{aligned} \tag{2.18}$$

Coherent states are of high experimental relevance since a standard laser operating above threshold produces a state which is in close approximation, a coherent state. This statement, although widely regarded as fact is still a subject of debate. Poissonian photon number distribution was verified experimentally shortly after the discovery of the laser [42]. In this experiment, photon statistics of a laser source operated well below, near, and well above threshold were observed to make a transition from a thermal to a Poissonian distribution. However this determines only the diagonal terms of the density matrix of the emitted state of light. The off-diagonal coherence terms turn out to be more subtle and objections have been raised [43] as to whether a laser in fact, produces a statistical mixture of photons or equivalently, a phase randomized coherent state:

$$\hat{\rho} = \int_0^{2\pi} |\alpha\rangle \langle\alpha| \, d\theta = e^{-|\alpha|^2} \frac{|\alpha|^{2n}}{n!} |n\rangle \langle n| . \tag{2.19}$$

However, apart from particular cases involving non locality [44] the experimental results do not seem to differ whether equation (2.12) or (2.19) is used since most experiments do not require a particular coherent state with a particular global phase but rather any coherent state. Having thus absolved my conscience of this subtlety, we assume for the remainder of this thesis that a source of coherent states is provided from the lasers in the experiment.

2.2.4 Thermal State

As opposed to the coherent state which is generated from a coherent source and thus contains coherences $\rho_{nm} = e^{-|\alpha|^2} \frac{\alpha^n (\alpha^*)^m}{\sqrt{n!m!}}$, light from a thermal source such as a heated

filament is incoherent and is represented by a statistical mixture of photons. Such a state, known as a thermal state is given by [45]:

$$\hat{\rho} = \frac{1}{G} \sum_{n=0}^{\infty} \left(\frac{G-1}{G} \right)^n |n\rangle\langle n| \tag{2.20}$$

where $G \equiv \bar{n} + 1$, $\bar{n}$ being the mean photon number of the field. The photon number variance of the thermal state is $\langle \Delta n^2 \rangle = \bar{n}^2 + \bar{n}$ and the quadrature variance is $\langle \Delta X^2 \rangle = \bar{n} + 1/2$.[8]

2.2.5 Squeezed State

So far two minimum uncertainty states - namely the vacuum state $|0\rangle$ and the coherent state $|\alpha\rangle$ both satisfy $\left\langle \Delta \hat{X}^2 \right\rangle = \left\langle \Delta \hat{P}^2 \right\rangle = 1/2$. However it is only the product of these two values which are bound by inequality (2.6) - we could have a state with $\left\langle \Delta \hat{X}^2 \right\rangle < 1/2$ as long as $\left\langle \Delta \hat{P}^2 \right\rangle$ is increased accordingly. Any state which for some quadrature $\hat{Q}$ satisfies $\left\langle \Delta \hat{Q}^2 \right\rangle < 1/2$ is known as a squeezed state.

In terms of photon number, a squeezed state consists of pairs of correlated photons. Sources of squeezed states thus involve processes which emits photons in pairs but have suppressed single photon emission. Each photon in a pair can exist in the same spatio-temporal mode, producing a *single-mode squeezed state* or in different modes, yielding a *two-mode squeezed state* (TMSS), described by the operator:

$$\hat{S}_{ab}(\zeta) = exp\left[\zeta \left(\hat{a}\hat{b} - \hat{a}^\dagger \hat{b}^\dagger \right) \right]. \tag{2.21}$$

The TMSS is of particular relevance, not only to this work, but also to fundamental physics since non-local correlations between quadratures may be quickly separated by great distances. In the limit $\zeta \to \infty$, the TMSS becomes the EPR state described by the original paper by Einstein, Podolsky, and Rosen which challenged the validity of the

[8] Derivation of these properties is found in Appendix B.

quantum mechanical description of reality [3]. The non-local character of the quadrature correlations inspires the definition of the so-called joint quadrature operators:

$$\hat{X}_{\pm} = \frac{\hat{X}_a \pm \hat{X}_b}{\sqrt{2}} \tag{2.22}$$

$$\hat{P}_{\pm} = \frac{\hat{P}_a \pm \hat{P}_b}{\sqrt{2}} \tag{2.23}$$

where $\hat{X}_a = (\hat{a}^\dagger + \hat{a})/\sqrt{2}$ is the operator describing the quadrature in mode a etc. The squeezing operator 2.21 transform the creation and annihilation operators according to the Bogoliubov transformation:[9]

$$\hat{S}^\dagger \hat{a} \hat{S} = \hat{a}\cosh(\zeta) - \hat{b}^\dagger \sinh(\zeta) \tag{2.24}$$

$$\hat{S}^\dagger \hat{b} \hat{S} = \hat{b}\cosh(\zeta) - \hat{a}^\dagger \sinh(\zeta)$$

$$\hat{S}^\dagger \hat{X}_{\pm} \hat{S} = \hat{X}_{\pm} e^{\mp\zeta}$$

$$\hat{S}^\dagger \hat{P}_{\pm} \hat{S} = \hat{P}_{\pm} e^{\pm\zeta}. \tag{2.25}$$

A special case of a TMSS state is the so called (two-mode) *squeezed vacuum*: $|\psi\rangle_{ab} = \hat{S}_{ab}(\zeta)\,|0\rangle_a\,|0\rangle_b$ which in the Fock basis, equates to [46]:

$$|\psi\rangle_{ab} = \sum_{n=0}^{\infty} \frac{\tanh(\zeta)^n}{\cosh(\zeta)}\,|n\rangle_a\,|n\rangle_b\,. \tag{2.26}$$

2.3 The Wigner Function

Given a quantum optical state $|\psi\rangle$ described in the last section, one would like to visualize and characterize its properties. Classically, we can characterize a state of a system by its phase space trajectory. Furthermore, given an ensemble of similarly prepared objects, we

[9] See appendix A for derivation of these properties.

can define the classical phase space density function $W_c(X,P)$ which describes the probability of finding the particle in the region R of phase space *via* $P_R = \iint_R W_c(X,P)dXdP$. Having the interpretation of probability, the phase space density function is necessarily real and non-negative. Experimentally, we can measure a coordinate of phase space, say position X repeatedly and observe the statistical distribution of results. For large enough measurement sets, we build up the *marginal distribution* $Pr(X)$ corresponding to the measured coordinate. We can relate the probability density to the marginal distribution through the relation:

$$\begin{aligned} Pr(X) &= \int_{-\infty}^{\infty} W_c(X,P)dP \\ Pr(P) &= \int_{-\infty}^{\infty} W_c(X,P)dX. \end{aligned} \tag{2.27}$$

Note that equation (2.27) also serves to relate the marginal distributions for different coordinates.

In quantum mechanics, we are forbidden to define such a phase space picture since position and momentum are not simultaneous observables and follow the uncertainty relation (2.6). We can however, given an ensemble of identically prepared quantum states, make a series of measurements of a particular coordinate which could be X, P, or in general, a linear combination of the two:

$$\hat{X}_\theta \equiv \hat{X}\cos\theta + \hat{P}\sin\theta = \left(\hat{a}^\dagger e^{i\theta} + \hat{a}e^{-i\theta}\right)/\sqrt{2}. \tag{2.28}$$

From these measurements we obtain the marginal distribution for each angle in phase space. Analogous to the classical case, a function exists which relates the marginal probability distributions of different coordinates as in (2.27).This function, known as the *Wigner function* [47], is defined as:

$$W_\rho(X,P) = \frac{1}{2\pi}\int_{-\infty}^{\infty} e^{iPQ}\left\langle X-\frac{Q}{2}\right|\hat{\rho}\left|X+\frac{Q}{2}\right\rangle dQ. \tag{2.29}$$

The Wigner function shares many similarities with the classical probability density function. The marginal probability distribution for a given coordinate X_θ can be obtained via the *Radon Transform*:

$$Pr(X_\theta) = \int_{-\infty}^{\infty} W(Xcos(\theta) - P\sin(\theta), P\sin(\theta) + X\cos(\theta))dX. \tag{2.30}$$

which is a generalization of (2.27). As in the classical case, the Wigner function is real and normalized: $\int_{-\infty}^{\infty} W(X,P)dXdP = 1$. By definition it is linear with respect to the density matrix so the Wigner function of a statistical mixture of states is represented as the sum of the Wigner functions of the constituent pure states. The Wigner function uniquely defines a quantum optical state, and the density matrix elements in a given basis may be obtained via [39]:

$$\langle n|\,\hat{\rho}\,|m\rangle = 2\pi\int_{-\infty}^{\infty} W_{|\psi\rangle}(X,P)W_{n,m}(X,P)dXdP \tag{2.31}$$

In contrast to the classical probability density function, the Wigner function may take on negative values and thus cannot be interpreted as a probability. Owing to equation (2.30) however, each negative dip must be surrounded by a positive hill so that the resultant marginal distribution is necessarily non-negative.

Given a quantum state ψ written in the Fock basis: $\hat{\rho} = \sum_{n,m}\rho_{mn}\,|m\rangle\,\langle n|$ the Wigner function may by calculated by combining equations (2.11) and (2.29) as

$$\begin{aligned} W_\rho(X,P) &= \sum_{m,n}\frac{1}{2\pi}\int_{-\infty}^{\infty} e^{iPQ}\psi_m^*(X-\frac{Q}{2})\psi_n(X+\frac{Q}{2})dQ. \\ &= \sum_{m,n}\frac{1}{2\pi^{3/2}}\int_{-\infty}^{\infty}\frac{e^{X^2+iPQ+\frac{Q^2}{2}}}{\sqrt{2^{n+m}n!m!\pi}}H_m(X-\frac{Q}{2})H_n(X+\frac{Q}{2})dQ. \end{aligned} \tag{2.32}$$

which may be quickly calculated analytically using a symbolic computing program (or tediously by hand if preferred). Wigner functions corresponding a number of quantum-optical states are shown in figure (2.1):

Although we primarily consider the Wigner function in this work, there are several commonly used quasi-probability distributions in quantum optics. The Glauber-Sudarshan P function [41, 48] is defined as the deconvolution of the Wigner function with the Wigner function of a vacuum state:

$$W_\rho(X,P) = \iint_{-\infty}^{\infty} P_\rho(X',P') W_{|0\rangle\langle 0|}(X-X',P-P')dX'dP'. \tag{2.33}$$

The P function can also be described as the function which diagonalizes the density matrix in the basis of coherent states. This property can be summarized by the optical equivalence theorem[10]:

$$\hat{\rho} = \iint_{-\infty}^{\infty} P(X,P) \left|\alpha\right\rangle \left\langle\alpha\right| dXdP. \tag{2.34}$$

The P function usually exists in highly singular form. From equation (2.33) it is apparent that the P function of a coherent state is a delta function $P_{|\alpha\rangle\langle\alpha|} = \delta^2(\alpha)$ and for many other states P is even more pathological. As a result, there is no convenient way to reconstruct the P function from experimental data, and experimentalists tend to prefer the Wigner function representation.

Another distribution - the Husimi Q function is defined as the convolution of the Wigner function with the Wigner function of a vacuum state:

$$Q(X,P) = \iint_{-\infty}^{\infty} W(X',P') W_{|0\rangle\langle 0|}(X-X',P-P')dX'dP'. \tag{2.35}$$

[10]The are several distinct but equivalent forms of this theorem, the stated version may be found in [39] and others may be found in, ex. [49].

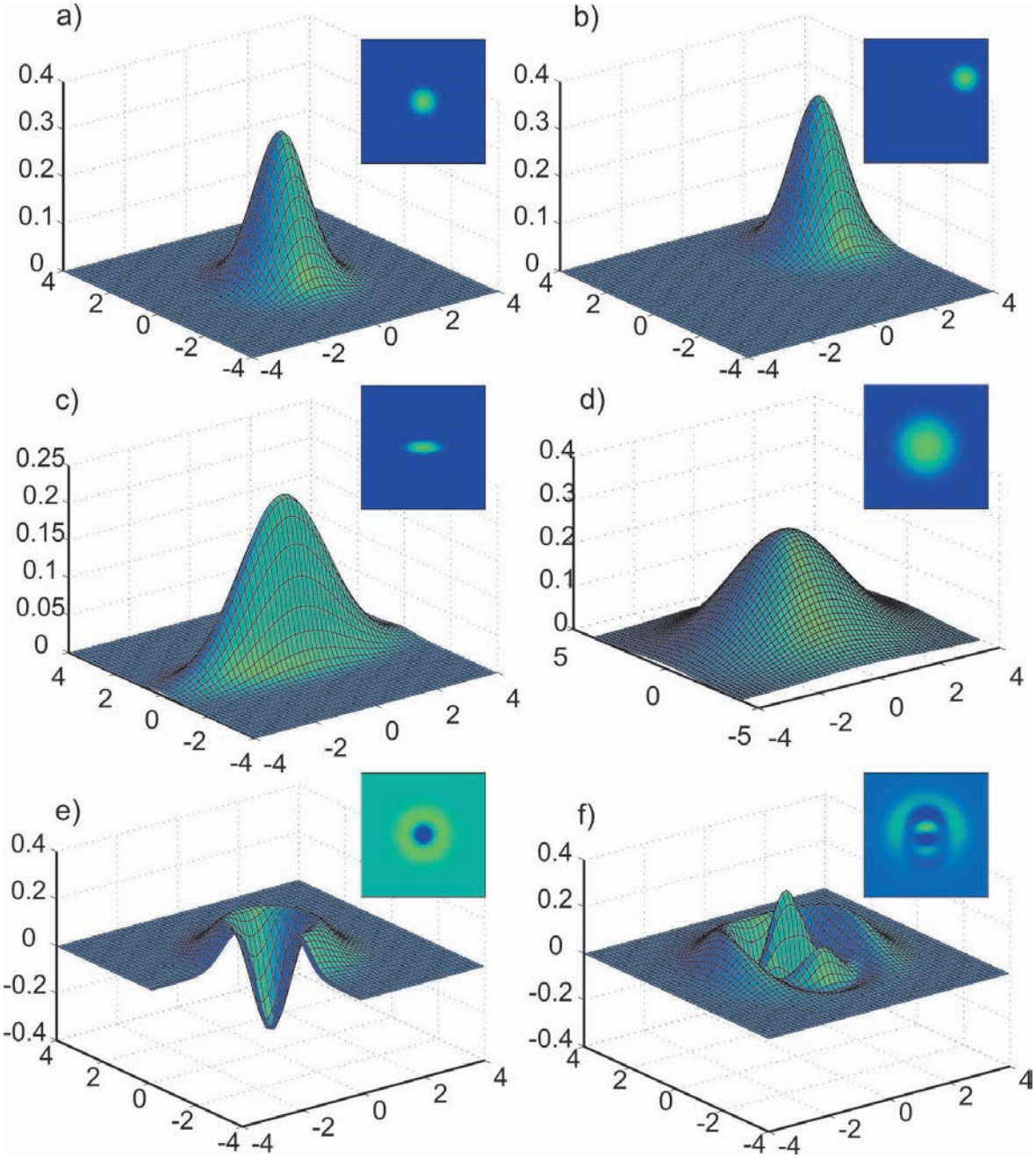

Figure 2.1: Wigner functions of various states discussed in sec. 2.2: (a) Vacuum state $|0\rangle$. (b) Coherent state $|\alpha\rangle$ with $\alpha = 3e^{i\pi/6}$. (c) Squeezed state $\hat{S}(\zeta)\,|0\rangle$ with $\zeta = 2$. (d) Thermal State with $\bar{n} = 2$. (e) Single photon Fock state $|1\rangle$. (f) Arbitrary Superposition state $|\psi\rangle = (1\,|0\rangle + 2\,|1\rangle + 3\,|2\rangle + 4\,|3\rangle)\,/\sqrt{30}$. Insets for each plot are the corresponding density plot.

Unlike the Wigner function, the Q function is non-negative and in fact may be interpreted directly as a probability distribution[11]. The Q function of a state is identical to the Wigner function of the same state that has undergone a 50% loss up to a scaling of the coordinates.

2.4 Quantum Optical Modes

Thus far we have restricted the analysis to a single spatio-temporal mode[12]. In general, full information of a quantum optical state may occupy several eigenstates of a chosen basis and are thus considered *multimode*. For the purpose of this work, light can be multimode in either spatial or temporal degrees of freedom[50]. Spatially multimode light requires more than one orthogonal transverse basis state for a full description. For example, laser light produced in a spherical optical cavity is bound by the orthonormal cavity eigen-modes TEM_{mn} (see chapter 5.2). Often, lasing can occur within several TEM modes producing spatially multimode light.

Continuous wave optical states such as a narrowband coherent state can be well described by a single temporal mode. We can represent this mode by the creation operator for the instant of time t: $\hat{a}(t)$. In a similar fashion we can isolate a particular frequency sideband of the steady state field $\hat{a}(\omega)$. The support of the state in frequency space is described by its spectral power density $S(\nu)$. In contrast to the steady state situation, a heralded quantum state is formed by partial measurement defining an instant of time t at which the state is transformed. Clearly here, the single temporal mode is inappropriate. For such states, the temporal mode is defined by its temporal coherence function

$$\Gamma(\tau) = \left\langle \hat{a}^\dagger(t)\hat{a}(t+\tau) \right\rangle \tag{2.36}$$

[11] See for example chapter 6 in [39]

[12] With the exception of the two-mode squeezed state, for which this medication was straightforward.

which is distributed over some envelope $\psi(t)$. From this weighting function, we can write a pure temporal state corresponding to $\psi(t)$ in terms of instantaneous modes as

$$\hat{a}_\psi \equiv \int_{-\infty}^{\infty} \psi(t)\hat{a}(t)dt. \tag{2.37}$$

Temporal and frequency modes are related through the Wiener-Khintchine theorem which states that the spectral power density is the Fourier transform of the temporal coherence function (2.36):

$$S(\nu) = \int_{-\infty}^{\infty} \Gamma(\tau)e^{-2i\pi\nu\tau}d\tau. \tag{2.38}$$

2.5 Quantum Light vs. Nonclassical Light, Nonclassicality Criteria

Quantum optics deals with a quantum mechanical treatment of the electromagnetic field. In this sense, all states of light in this formalism are quantum states of light but we wish to distinguish states that have a classical analogue and those that do not. To paraphrase Sir Peter Knight [51], who was, in turn, paraphrasing George Orwell [52], "all states are quantum, but some are more quantum than others." As we have seen, the coherent state has the properties one would expect from a classical oscillator and it makes sense that we would classify this as a classical state. In fact, it is *the* classical state of light in terms of the following definition:

Definition. *A quantum optical state is said to be* ***classical*** *is it can be expressed as a statistical mixture of coherent states. A state is* ***non-classical*** *if it cannot.*

2.5.1 Negativity of P function

From the optical equivalence theorem (2.34), it is apparent that an equivalent definition for classicality is a positive definite P function[13] since $P(\alpha)$ then acts as a weighting function for a given coherent state α. Indeed this has been shown more rigorously by Hillery [53] for the case of pure states. As mentioned, P functions are not conveniently inferred from experimental data, and so a number of non-classicality criteria exist which provide sufficient, but not necessary conditions on non-classicality:

2.5.2 The Squeezing Criteria

For the coherent state, $\langle \Delta X_\theta^2 \rangle = 1/2$ for all θ such that (2.6) is satisfied. Squeezed states, while still subject to inequality (2.6), have $\langle \Delta X_\theta^2 \rangle < 1/2$ for some θ. This leads to the following criterion: Any state for which there exist a phase-space coordinate X_θ satisfying $\langle \Delta X_\theta^2 \rangle < 1/2$ is non-classical under the squeezing criterion. For a pure squeezed state this follows from the definition of the P-function: Since the Fourier transform of a convolution of functions is the product of the Fourier transforms of the respective functions, equation (2.33) gives:

$$\mathcal{F}(P_{\mathrm{S}(\zeta)}(X,P)) = \frac{\mathcal{F}(W_{|0\rangle\langle 0|}(X,P))}{\mathcal{F}(W_{\mathrm{S}(\zeta)}(X,P))} \tag{2.39}$$

The Fourier transform of a Gaussian of variance σ^2 is a Gaussian of variance $1/(2\pi\sigma^2)$, and since both the squeezed state and vacuum state have Gaussian Wigner functions, $\mathcal{F}(P_{S(\zeta)})$ must diverge along the (Fourier-transformed) squeezed quadrature and hence is more singular than a delta function[14]. In general since any classical state is a statistical mixture of coherent states each having quadrature variance $\langle \Delta X_\theta^2 \rangle = 1/2$, the sum of all states must have variance $\langle \Delta X_\theta^2 \rangle \geq 1/2$, with equality holding only in the case that each state is identical, i.e. a coherent state. Finally, note that the squeezing criterion does

[13] For the purposes of this thesis, a delta function is considered to be positive definite.

[14] The Fourier transform of a simple delta function is a complex phase e^{ikx_0}

not require a minimum uncertainty state, but only that for at least one quadrature the variance is less than that of a coherent state.

2.5.3 The Intensity Squeezing Criteria

The definition of classicality in terms of coherent states also sets a limit on the level of photon number fluctuations, or equivalently intensity fluctuations, for a classical state. Recall that according to equations (2.14) and (2.15), a coherent state follows Poissonian statistics: $\langle \Delta n^2 \rangle = \langle n \rangle$. A state with $\langle \Delta n^2 \rangle < \langle n \rangle$ follows sub-Poissonian photon number statistics and is said to be non-classical according to the intensity squeezing criterion. In terms of experimentally measurable quantities, the intensity squeezing criterion states that any state for which the photon number fluctuations are lower than that of a coherent state of the same intensity is intensity squeezed. The reason that intensity squeezing is considered to be a non-classical effect can be seen by noting that we can write $\langle \Delta n^2 \rangle = \langle n \rangle + \left(\langle \hat{a}^{\dagger 2} \hat{a}^2 \rangle - \langle \hat{a}^\dagger \hat{a} \rangle^2 \right)$. The rightmost term can be re-expressed in terms of the P function as $\int P(\alpha) \left[|\alpha|^2 - \langle \hat{a}^\dagger \hat{a} \rangle \right]^2 d^2\alpha$ [51] so that:

$$\langle \Delta n^2 \rangle - \langle n \rangle = \int P(\alpha) \left[|\alpha|^2 - \langle \hat{a}^\dagger \hat{a} \rangle \right]^2 d^2\alpha. \tag{2.40}$$

Clearly then, $\langle \Delta n^2 \rangle < \langle n \rangle$ implies that $P(\alpha)$ must take on negative values in at least some regions of phase space and the intensity squeezed state is thus by definition, non-classical.

2.5.4 Negativity of Wigner Function

The Wigner function of a coherent state $\left| \alpha = \frac{X+iP}{\sqrt{2}} \right\rangle$ is a displaced Gaussian centred at (X, P). Furthermore, the linearity of the Wigner function implies that for any classical state $\hat{\rho} = \sum_n c_n |\alpha_n\rangle \langle \alpha_n|$ has a Wigner function which is the sum of Gaussians and is necessarily positive definite. If the Wigner function of a state takes on a negative value at any point (X, P) then that state is non-classical. As an example, the single photon Fock

state is highly negative at the origin $W_{|1\rangle\langle 1|}(0,0) = -\frac{1}{\pi}$. Not all nonclassical states have negative Wigner functions however. For example the squeezed vacuum Wigner function is Gaussian, yet non-classical by the squeezing criterion.

2.5.5 Anti-Bunching Criteria

The intensity squeezing criterion classifies a state as non-classical based on sub-Poissonian statistics. Other non classicality criteria may be formulated in terms of photon counting statistics. This is especially relevant in experimental quantum optics at the few photon level where single photon counting modules are frequently employed[15]. The first is based on the second order correlation function:

$$g^{(2)}(\tau) = \frac{\left\langle \hat{a}^\dagger(t)\hat{a}^\dagger(t-\tau)\hat{a}(t)\hat{a}(t-\tau)\right\rangle}{\left\langle \hat{a}^\dagger(t)\hat{a}(t)\right\rangle^2}. \tag{2.41}$$

which gives the probability of finding a second photon at a fixed delay τ from an initial photon at time t. Here, $\hat{a}^\dagger(t)$ describes the annihilation operator in the mode corresponding to time t, as described in section 2.4. If $g^{(2)}(\tau)$ is at a maximum at $\tau = 0$ then we have photon bunching (i.e. decreasing probability of finding a photon at later times) whereas a minimum $g^{(2)}(0)$ implies photon anti-bunching. Anti-bunching is closely related to sub-Poissonian statistics described in section 2.5.3, but the two criteria are not equivalent [54].

For a coherent state

$$g^{(2)}(0) = \frac{\langle\alpha|\,\hat{a}^\dagger\hat{a}^\dagger\hat{a}\hat{a}\,|\alpha\rangle}{\langle\alpha|\,\hat{a}^\dagger\hat{a}\,|\alpha\rangle^2} = \frac{\alpha^*\alpha^*\alpha\alpha}{(\alpha^*\alpha)^2} = 1. \tag{2.42}$$

which set the classical limit: Any state for which $g^{(2)}(0) < 1$ is said to be non-classical by the anti-bunching criterion. As an example, a Fock state $|n\rangle$ has $g^{(2)}(0) = 1 - 1/n$ whereas for a thermal state, $g^{(2)}(0) = 2$.

[15] See chapter 3.

An equivalent anti-bunching criterion is a negative Mandel Q parameter:

$$Q = \frac{\langle \Delta n^2 \rangle - \langle n \rangle}{\langle n \rangle} < 0. \tag{2.43}$$

To see the equivalence of the above criteria, note that we can re-write (2.41) at zero time delay in terms of photon number as:

$$g^{(2)}(0) = \frac{\left\langle \hat{a}^\dagger (\hat{a}\hat{a}^\dagger - 1)\hat{a} \right\rangle}{\langle \hat{a}^\dagger \hat{a} \rangle^2} = \frac{\langle \hat{n}^2 \rangle - \langle \hat{n} \rangle}{\langle \hat{n} \rangle^2} = \frac{\langle \Delta n^2 \rangle - \langle \hat{n} \rangle + \langle n \rangle^2}{\langle \hat{n} \rangle^2} = \frac{Q}{\langle n \rangle} + 1. \tag{2.44}$$

Clearly then, $g^{(2)}(0) < 1$ if and only if $Q < 0$. From the definition (2.43) it is evident that for sub-Poissonian light, $Q < 0$, for a coherent state $Q = 0$, and for super-Poissonian light, $Q > 0$.

2.5.6 Criteria for Specific Density Matrix Elements

Suppose that we are given a density matrix of an unknown quantum state and we wish to know whether or not it is non-classical[16]. First, the probability of finding a specific number of photons n in a coherent state is non-zero ($\Pr_n = |\langle n|\alpha\rangle|^2 = e^{-|\alpha|^2} \frac{|\alpha|^{2n}}{n!}$). A statistical mixture of coherent states thus has $\Pr_n > 0$. Any state ρ having a vanishing diagonal element $\rho_{nn} = 0$ is non-classical[17]. Consequentially, any non-vacuum state with a finite Fock state decomposition is non-classical.

We can also look at particular density matrix elements. For a coherent state, equation (2.13) gives $\rho_{11} = e^{-|\alpha|^2} |\alpha|^2 = \bar{n} e^{-\bar{n}}$ where $\bar{n} \equiv |\alpha|^2$. Note then $\frac{d}{d\bar{n}} \rho_{11} = (1 - \bar{n}) e^{-\bar{n}} = 0$ when $\bar{n} = 1$, i.e. the highest possible single photon component of a coherent state occurs with a coherent state of mean photon number 1 for which $\rho_{11} = e^{-1} \approx 0.37$. For a statistical mixture, $\rho = \sum_\alpha c_\alpha \rho_\alpha$, $\rho_{11} = \sum_\alpha c_\alpha \rho_{\alpha,11} \leq \max[\rho_{11}] \sum_\alpha c_\alpha = e^{-1}$. Therefore, any state with $\rho_{11} > e^{-1}$ is non-classical.

[16] This is of particular relevance to this work since we extract the density matrix of a quantum optical field from data acquired using optical homodyne detection

[17] The trivial exception being the vacuum state

Chapter 3

Detecting Nonclassical Light: Quantum State Tomography

3.1 Quantum State Detection

3.1.1 Intensity Detection

The simplest way to detect light is by use of a detector which measures photon flux, that is, the number of photons per second incident on the detector's active area. Such a device, known as a photodiode, accomplishes this by converting each incident photon into an electron with probability η, known as the quantum efficiency. In the near infrared band, commercial Silicon PIN photo-diodes have $\eta > 90\%$ with specialized models reaching 99.8% [55]. Since even a small optical power corresponds to a large photon flux[1], a beam of light on a photodetector is measured as a current which may be amplified and measured on an oscilloscope.

The signal from the photodiode is linear only over a small range of input powers, after which saturation causes a reduced response. This linear photo-current is typically weak and furthermore, depends on the impedance of the output load. To circumvent these limitations, a layer of electronics is typically placed between the photodetector and the measurement device. To extend the linear range and to decrease the response time of the diode, a reverse bias voltage is placed across the junction [56]. In order to provide isolation between the photodiode and the measurement device, and to produce a measurable signal level, an amplification stage consisting of a transimpedance amplifier [2]

[1] At $\lambda = 795$nm, each photon has an energy of $hc/\lambda = 1.56$ eV $= 2.50 \times 10^{-19}$J. The conversion factor is then 4×10^{18}photons/second per Watt. The smallest signal detectable by a photo-diode (1 nW or so) still corresponds to about one billion photons per second.

[2] An inverting op-amp with no input resistance is said to be in transimpedance configuration. In this case, the amplifier acts as a current to voltage converter with gain measured in Ohms.

followed by several op-amps is employed. This stage limits the bandwidth to some cut-off frequency f_c avoiding electronic nonlinearities [57], and sets the gain to be constant for all frequencies less than f_c.

In this work, as in many experiments in quantum optics, we were primarily interested in the "noise" of the detected light. What is meant by noise in this context is a fluctuation in some property the light which is quantified by the variance of this property at a given frequency. As mentioned in section 2.5.3, a coherent state exhibits fundamental uncertainty in the number of photons in the field at a given time. When measured on a photodiode, this noise is converted to an electronic signal known as *shot noise*. Of course, the light could contain additional sources of noise due to amplitude or phase modulation of the source. This noise is typically known as technical, or classical noise. The electronics which amplify the photo-current also invariably add some noise to the signal, and it is important to distinguish between shot noise and the technical noise due to the equipment.

The shot, electronic, and technical noise can be measured using two identically constructed photodetectors as depicted in figure 3.1. A beam is split on a 50 : 50 beamsplitter and sent to each detector, where the variance of the sum and difference of the outputs is monitored on a spectrum analyzer. When the light is blocked, the base level of noise gives the electronic noise floor. When the beam is unblocked, the difference port subtracts away all technical noise due to signal modulation and all that is left is the shot noise and electronic noise. Since the electronic and shot noise are uncorrelated, they add in quadrature so that the displayed clearance above electronic noise is the shot noise of the beam. Finally, the sum port is equivalent to directly measuring the signal with a single detector and the clearance above the difference signal gives the technical noise on the beam. A beam for which the sum and difference powers are equal is said to be shot noise limited.

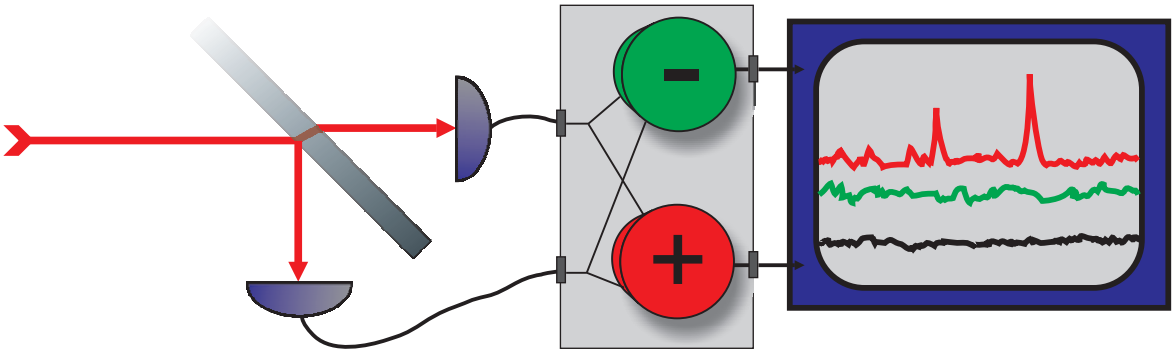

Figure 3.1: Experimental setup to determine the electronic (black), shot (green), and technical plus shot (red) noise components of a signal.

Given a single detector, it is also possible to tell whether or not the beam is shot noise limited based on the scaling of the measured noise with frequency. Recall that for the coherent state, $\langle \Delta n^2 \rangle = |\alpha|^2$, i.e, the variance scales linearly with intensity. In contrast, technical noise is proportional to the electric field amplitude and thus scales quadratically with the electric field. The quadratic component of the scaling of the variance at a given frequency with power therefore determines the amount of technical noise on the beam.

3.1.2 Photon Counting

In order to measure signals below the resolution of the standard photodiode a modification of the above photodiode known as an avalanche photodiode (APD) may be used. In addition to the photosensitive surface region of a photodiode, an APD has a multiplication region in which a strong electric field increases the kinetic energy of the photoelectron to the extent that it will create further electron-hole pairs as it collides with other atoms. The APD is thus a specialized photodetector with an internal gain mechanism controlled by a strong reverse bias. If the reverse bias is placed above the breakdown voltage of the diode, the APD is said to be in "Geiger mode" in which a single photo-electron in the multiplication region will create a self sustaining avalanche. A Geiger mode APD thus

serves as a single photon detector. After an avalanche has started, the current must be quenched so that the detector can respond to the next photon. This is accomplished by reducing the voltage below V_{bias} for a period Δt known as the dead-time. During the dead time, the APD no longer responds to incident photons.

Often, the Geiger-mode APD and the quenching circuitry is placed together forming a single photon counting module (SPCM) which outputs a logical pulse for each photon event. SPCMs can identify individual photon events with a temporal resolution of a few hundred ps and are ideal for heralding the presence of a partner photon in a biphoton pair. Unfortunately, there are two major limitations of SPCMs: First, the quantum efficiency[3] is much less than for a Si photodiode, typically less than 50%. Second, the dead-time places a limitation on the maximum photon flux measurable and there is always a probability of losing information during this time. Finally, SPCMs are not number resolving as the 'S' in the acronym implies. Instead, they detect the presence of *at least* one photon but can not distinguish between 1, 2, or 10 simultaneous photon events.

3.1.3 Quadrature Detection: The Homodyne Detector

Intensity and SPCM measurements described above give information about photon number distributions. In the Fock basis, these measurements determine only the diagonal elements but can not distinguish between the state $|\psi\rangle = \alpha|0\rangle + \beta|1\rangle$ and the mixture $\rho = |\alpha|^2 |0\rangle\langle 0| + |\beta|^2 |1\rangle\langle 1|$. The difference between the two cases lays in the coherence which describes a fixed phase relation between the two states. Since the phase of a typical optical mode oscillates at several hundred THz, we have no hope of measuring the field oscillations directly but rather measure the time averaged field squared, which erases phase information.

[3]Strictly speaking, the quantum efficiency of the diode in the SPCM is as high as mentioned earlier, but the electronic layer leads to a *photon detection probability* of 50% or lower.

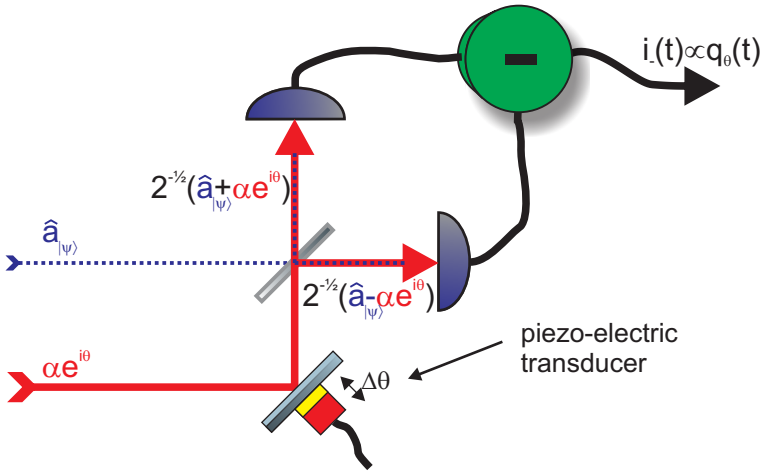

Figure 3.2: Basic configuration for homodyne detection. The state $\hat{a}_{|\psi\rangle}$ is mixed on a 50:50 beam-splitter and each port is monitored by a photodiode. The resultant photocurrent is subtracted producing a signal proportional to the quadrature of $|\psi\rangle$. The piezo-electric transducer attached to the mirror scans the optical phase of the local oscillator.

A clever technique to directly measure the quadratures of a quantum state exists and is known as balanced homodyne detection (BHD). In BHD, a strong classical field is overlapped with the weak quantum state in question on a symmetric beam splitter (figure 3.2). Each output port is aligned incident on a linear photodiode to produce a photocurrent. The photocurrent from each arm of the beamsplitter is then subtracted and the difference in the photocurrent gives a signal that is proportional to the quadrature of the input state. The strong classical field, known as the local oscillator is assumed to be phase stable with the quantum state. We assume a coherent state $|\alpha\rangle = \left||\alpha|\, e^{i\theta}\right\rangle$ for which the phase can be experimentally set by introducing a small delay via a mirror attached to a piezo-electric transducer.

That the BHD measures the quadrature of the quantum state can be seen as follows: first note that as described in the last section, the photocurrent from each detector gives a signal which is proportional to the photon flux of the incident field $\hat{i}(t) = g\hat{n}(t)$. The beamsplitter transforms the input fields as $\hat{a}_{1(2)} \rightarrow 2^{-1/2}\left(\hat{a}_1 \pm \hat{a}_2\right)$. Since the local

oscillator is bright ($|\alpha| \gg 1$) we neglect its fluctuations and describe it solely by its amplitude so that $\hat{a}_{1(2)} \rightarrow 2^{-1/2}(\hat{a} \pm \alpha)$. The number of photons in each channel is thus $\hat{n}_{1(2)} = \hat{a}^{\dagger}_{1(2)}\hat{a}_{1(2)} = \frac{1}{2}\left(\hat{n}_1 + \hat{n}_2 \mp |\alpha|\left(\hat{a}e^{i\theta} + \hat{a}^{\dagger}e^{i\theta}\right)\right)$. Identifying the right-most term as the phase dependent quadrature, the difference in photocurrent $\hat{i}_{HD} \equiv \hat{i}_2 - \hat{i}_1$ becomes:

$$\hat{i}_{HD}(t) = \gamma \hat{q}_{\theta}(t). \tag{3.1}$$

where $\gamma \equiv \sqrt{2}\,|\alpha|\,g$.

Here we see the essential features of BHD. First, the classical noise is completely cancelled out so that technical noise does not pollute the measurement. Second, the local oscillator amplifies the phase of the quantum state to a measurable level so that extremely weak signals ($\langle \hat{n} \rangle < 1$) can be detected. Third, the high quantum efficiency of Si photodiodes allow for low-loss detection of the quantum state. Although the above calculation was on the "hand-wavy" side, more sophisticated treatments yield the same result [58].

There are several experimental caveats that must be made in stating equation (3.1). First, the inefficiency of real photodiodes must be taken into account. Second it may not be possible to perfectly match the spatio-temporal mode of the local oscillator to the quantum state in question. The degree of "mode-mismatch" can be quantified by the visibility $\mathcal{V}$ which is measured by interference contrast[4]. Each of these degrading effects may be modelled as a beam splitter of transmissivity T with vacuum applied to the perpendicular port. For detectors with quantum efficiency η, $T = \eta$ [39], for mode-mismatch, $T = \mathcal{V}^2$ [45].

Equation (3.1) describes an instantaneous measurement of the quadrature correspond-

[4]If two states of equal intensity I_0 occupy the same mode and the relative phase between the two is scanned, the resultant intensity will periodically vary from $I_{min} = 0$ to $I_{max} = 4I_0^2$. If they do not occupy the same mode, the amplitude of intensity modulation will be reduced and perfect cancellation will no longer be present, i.e. $I_{min} > 0$. This can be quantified by the visibility $\mathcal{V} = \frac{I_{max} - I_{min}}{I_{max} + I_{min}}$.

ing to an instantaneous temporal mode described in section 2.4. To reconstruct the quadrature of a temporal mode described by $\phi(t)$, we define the quadrature akin to equation (2.37) as

$$\hat{Q}_\psi \equiv \int_{-\infty}^{\infty} \hat{q}(t)\phi(t)dt. \tag{3.2}$$

From equation (3.1) we can then obtain a quadrature value from integrating the photocurrent by the temporal mode function.

In reality, the relation between the homodyne current is complicated by the presence of electronic noise and limited bandwidth of the detector. The electronic noise current $i_e(t)$ has some variance $\left\langle \Delta\hat{Q}_e^2 \right\rangle$ which adds in quadrature to the photocurrent. The bandwidth is limited by the response function of the detector $r(t)$ in that faster signals become averaged out from the detectors inability to follow the changes. Ideally $r(t)$ is a Dirac delta function but in reality, has some width. The maximum measurable frequency scales as the inverse of this width through the Fourier relation. What is measured on a real detector is then the convolution of the detectors response function with the photocurrent plus the electronic noise.

$$\hat{i}(t) = \int r(t-t')\hat{q}(t')dt' + \hat{i}_e(t) \tag{3.3}$$

If we measure the temporal mode $\psi(t)$, we find

$$\begin{aligned} \hat{Q}_{meas} &\propto \int_{-\infty}^{\infty} \hat{i}(t)\psi(t) \\ &= \gamma \int_{-\infty}^{\infty}\int_{-\infty}^{\infty} \hat{q}(t')\psi(t)r(t-t')dtdt' + \int_{-\infty}^{\infty} \hat{i}_e(t)\psi(t)dt \\ &= \gamma \int_{-\infty}^{\infty} \hat{q}(t')\psi'(t')dt' + \hat{Q}_e \end{aligned} \tag{3.4}$$

where $\psi'(t') \equiv \int_{-\infty}^{\infty} \psi(t)r(t-t')dt$ and $\hat{Q}_e = \int_{-\infty}^{\infty} \hat{i}_e(t)\psi(t)dt$. From this, we see that if we choose a temporal mode $\phi(t)$ such that $\psi'(t) = \phi(t)$, we can completely correct for

the degrading effects of limited bandwidth. This deconvolution is difficult to perform accurately for arbitrary response functions. However, if our detector bandwidth is much larger than the inverse time scale of the quantum state's temporal mode, $r(t)$ approximates a delta function and does not significantly alter the measured state. The efficiency of reconstructing the state with true temporal mode $\psi(t)$, in some mode $\phi(t)$ is given by [59]:

$$1 - \eta_{bw} = \frac{1}{N} \left| \int_{-\infty}^{\infty} \psi'(t)\phi(t)dt \right| \tag{3.5}$$

where $N = \int_{-\infty}^{\infty} |\psi'(t)|^2 \, dt$. Figure (3.3a) displays η_{bw} for a quantum state of Gaussian temporal shape $\psi(t) = e^{-\left(\frac{t-t_0}{\sqrt{2}\sigma}\right)^2}$, in this mode ($\phi(t) = \psi(t)$) as a function of detector bandwidth. We see that in order to faithfully reconstruct the quantum state, we need a bandwidth at least the same order of magnitude as the inverse temporal width of the signal.

Electronic noise also reduces the effective measurement efficiency of the reconstructed state. With signal and electronic noise variance $\left\langle \Delta\hat{Q}^2 \right\rangle$ and $\left\langle \Delta\hat{Q}_e^2 \right\rangle$ respectively this quantified as

$$1 - \eta_e = \frac{\langle \Delta Q_e^2 \rangle}{\langle \Delta Q^2 \rangle}. \tag{3.6}$$

Experimentally we can view the electronic and photocurrent at all frequencies by monitoring the homodyne output on a spectrum analyzer. To the extent that the spectrum of the detector is constant over the bandwidth of the detector, we can write equation (3.6) as (see appendix E.1) as:

$$1 - \eta_e = \frac{S_e(\nu_0)}{S(\nu_0)}. \tag{3.7}$$

where ν_0 is within the bandwidth of the detector.[5] The quantity on the right hand side

[5]If the electronic noise is not constant, equation (3.7) provides an lower bound on the efficiency.

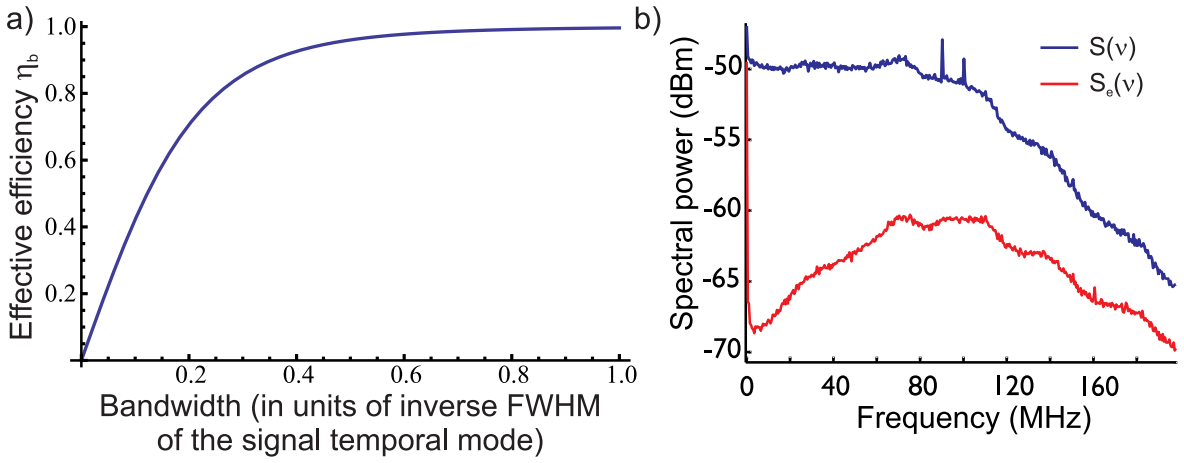

Figure 3.3: (a) The detection efficiency of a wide-band state with a limited bandwidth detector. In order to accurately measure a signal, the response of the detector should be at least as fast as the inverse signal bandwidth. (b) The spectrum of the homodyne detector used in the single photon experiments of chapters 4 and 5. The clearance ranges from 10 dB to 18dB over the 100 MHz bandwidth. The peaks around 100 MHz correspond to classical noise peaks which were not fully suppressed by the detectors common mode rejection ration (CMRR).

is known as the clearance. The clearance increases as the square root of local oscillator power[6] and so the degrading effects electronic noise become less significant with increasing local oscillator strength. However, the saturation intensity of the photodiodes puts an upper bound on the maximum obtainable clearance. In practice, the local oscillator intensity is set just below saturation[7].

From equation (3.7) we see that the degradation of the precision of a real homodyne detector is simply the inverse shot to electronic noise ratio, and as such special care needs to be taken to minimize electronic noise in the circuit. The additional requirement of high bandwidth is often incompatible with low electronic noise so homodyne detector design is a careful balance of bandwidth and low-noise amplification [59].

[6]Note that in the parlance of the last section, we are simply measuring the shot noise.

[7]Of course, saturated or not saturated isn't a binary question, but we can place a limit on the acceptable degree of nonlinearity. The data sheet for the particular photo-diode will state the *saturation intensity* for which the deviation from linearity is below a stated value.

Figure (3.3b) shows the performance of the detector used in the experiments described in chapters 4 and 5. The detector has a 3 dB bandwidth of approximately 100 MHz with a flat response over this range. In this trace a 12 mW local oscillator was split at a polarizing beam splitter yielding a clearance ranging from 10 dB to 18 dB over the spectral support of the detector. From equation (3.7) this corresponds to an efficiency η_e of 0.90 to 0.98.

3.2 Iterative Maximum Likelihood Estimation of Quantum States

Homodyne detection gives us the marginal distribution $\Pr(q_\theta)$ corresponding to any phase angle θ. From this set of projections, we then need to faithfully reconstruct the original state that produced them. Historically, this was accomplished by tomographic reconstruction akin to medical computed tomography (CT) scanning where a three-dimensional object is reconstructed from a set of two-dimensional projections [60].

In optical homodyne tomography we are given a set of marginal quadrature distributions, and aim to invert the Radon Transform (2.30) to extract the Wigner function [61]. From the Wigner function, the density matrix in any basis is directly computed from the Fourier relation (2.31). A drawback to this method is that numerical implementations of the inverse Radon transform must invoke low-pass filtering owing to a singularity of the integration kernel [33]. This filtering necessarily results in the loss of accuracy and the chosen cut-off frequency is somewhat arbitrary. This can be partially overcome by the method of pattern functions [62] in which individual density matrices are directly sampled from the quadrature data. The cut-off is now applied directly to the maximum photon number of interest rather than the spatial frequency which is usually the more well-known quantity. This method however contains another serious drawback: since the density matrix elements are individually sampled, the resultant density matrix as a

whole can be unphysical, often containing negative diagonal elements.

To avoid the drawbacks of the above inverse transform techniques, a method of statistical inference may be used known as maximum likelihood estimation. Very roughly, maximum likelihood determines the physically observable density matrix that fits the observed data with the highest probability. From the density matrix, the Wigner function may be directly computed from equation (2.29). Maximum likelihood guarantees a physical density matrix which does not suffer from numerical artifacts associated with filtering and experimental fluctuations.

3.2.1 Maximum Likelihood Estimation

Suppose we have a source of pure single photons that are transmitted across a long optical fiber. Either the photon makes it through the fiber, in which case $\rho = |1\rangle\langle 1|$, or it does not, $\rho = |0\rangle\langle 0|$. The optical state at the output of the fiber may then be described as a mixture $\rho = (1-\eta)\,|0\rangle\langle 0| + \eta\,|1\rangle\langle 1|$, for some $0 \leq \eta \leq 1$. We then perform homodyne measurement and determine the marginal distributions along each quadrature[8] and ask, what is the density matrix of my state? We can try different values of η and eventually we could find a good fit but experimental uncertainties will guarantee that we will never find a perfect fit. We thus seek a function which quantifies the "goodness" of our guess.

One such function is known as the likelihood function. The likelihood supposes that each measurement x_i is drawn from some distribution (the sum of vacuum and single photon marginals in the above example) which is described by some set of parameters (η here): $\Pr_\eta(x)$. Assuming independent measurements, the probability that the distribution $\Pr_\eta(x)$ produced the measurements $\{x_i\}_i$ is just the product of the individual probabilities:

[8] Actually, any quadrature will give the same distribution in this example so we need not check them all.

$$L(\eta) = \prod_{i=1}^{N} \Pr_{\eta}(x_i). \tag{3.8}$$

The principle of maximum likelihood provides a estimation of the parameters of the parent distribution which maximize the likelihood of the measured data. The parameter set η which maximizes L is called the estimator. In practice the log-likelihood is maximized which converts the product to a sum. For simple cases as above, the analytic expression for the estimator may be obtained directly by differentiation with respect to η. For an n-dimensional density matrix with order n^2 parameters the condition for maximum likelihood estimator must be found numerically.

3.2.2 An Iterative Algorithm Maximum Likelihood Estimation of Homodyne Data

An optical homodyne detection measurement samples the continuous variable q_θ at a fixed angle θ which is also continuous over $[0, 2\pi]$. To calculate the measured probability distribution at a given quadrature angle, we distribute the data over N_θ bins and calculate probability for the quadrature corresponding to the j^{th} bin as the frequency of occurrence of a quadrature measurement laying in this range:

$$f_{j,\theta} = \frac{N_{\theta,j}}{N_\theta}. \tag{3.9}$$

The experimental data we wish to estimate then consist of a quadrature histogram $\{N_j\}$ for each angle θ. The log-likelihood is thus:

$$\ln\left[L(\rho)\right] = \ln\left[\prod_{j,\theta} \Pr_{\theta,j}^{N_{\theta,j}}\right] = \sum_{\theta,j} N_{\theta,j} \ln\left(\Pr_{\theta,j}\right) \tag{3.10}$$

Note that the theoretical probability of a measurement of quadrature laying in the range $[q_j, q_{j+1}]$ given a density matrix ρ is

$$pr_{j,\theta} = \int_{q_j}^{q_{j+1}} pr_\theta dq = \int_{q_j}^{q_{j+1}} \mathrm{Tr}\left[\rho \left|q_\theta\right\rangle\left\langle q_\theta\right|\right] dq = \mathrm{Tr}\left[\hat{\rho}\hat{\Pi}_{\theta,j}\right] \tag{3.11}$$

where $\hat{\Pi}_{\theta,j} \equiv \int_{q_j}^{q_{j+1}} \left|q_\theta\right\rangle\left\langle q_\theta\right| dq$ is the projection operator of the quadrature onto the interval $[q_j, q_{j+1}]$.

Following previous developments [63], we note that the density matrix may be written as $\hat{\rho} = \hat{\sigma}^\dagger\hat{\sigma}$ where $\hat{\sigma}$ is represented by lower triangular matrix. Maximizing the likelihood with respect to $\hat{\rho}$ is then equivalent to maximizing with respect to $\hat{\sigma}$. The rationale behind this representation is that $\hat{\rho}$ is completely determined by its upper triangular elements since it is self-adjoint. Allowing $\rho_{i,j}$ and $\rho_{j,i}$ to be determined independently may result in unphysical density matrices.

The maximum likelihood condition is also constrained to physically realizable density matrices such that $\mathrm{Tr}(\rho) = 1$. We can then formulate the condition for maximum likelihood for realistic density matrices as a Lagrange multiplier problem:

$$\frac{d}{d\hat{\sigma}}\left[\ln L\left(\left(\hat{\sigma}^\dagger\hat{\sigma}\right) - \lambda\left(\mathrm{Tr}\left(\hat{\sigma}^\dagger\hat{\sigma}\right) - 1\right)\right]\right. . \tag{3.12}$$

To determine λ we carry out the differentiation[9] to find

$$\begin{aligned} \frac{d}{d\hat{\sigma}}\left(\sum_{\theta,j} N_{\theta,j} \ln\left(\Pi_{\theta,j}\hat{\sigma}^\dagger\hat{\sigma}\right)\right) &= \lambda\frac{d}{d\hat{\sigma}}\left(\mathrm{Tr}\left(\left(\hat{\sigma}^\dagger\hat{\sigma}\right)\right)\right. \\ \sum_{\theta,j}\frac{N_{\theta,j}}{pr_{\theta,j}}\Pi_{\theta,j}\hat{\sigma} &= \lambda\hat{\sigma} \\ \sum_{\theta,j}\frac{N_{\theta,j}}{pr_{\theta,j}}\Pi_{\theta,j}\hat{\rho} &= \lambda\rho. \end{aligned} \tag{3.13}$$

[9]Note that if $\hat{A}$ and $\hat{B}$ are matrices, $\frac{d}{d\hat{A}}\mathrm{Tr}(\hat{A}\hat{B}) = \hat{B}^T$[64].

Tracing both sides we find

$$\begin{aligned} \sum_{\theta,j} \frac{N_{\theta,j}}{pr_{\theta,j}} \mathrm{Tr}\left[\Pi_{\theta,j}\hat{\rho}\right] &= \lambda \mathrm{Tr}\left[\rho\right]. \\ \sum_{\theta,j} N_{\theta,j} = N &= \lambda \end{aligned} \tag{3.14}$$

Having found λ, equation (3.13) now reads

$$\left[\sum_{\theta} \frac{N_\theta}{N} \sum_{j} \frac{f_{\theta,j}}{pr_{\theta,j}} \Pi_{\theta,j}\right] \hat{\rho} \equiv \hat{R}_{\hat{\rho}}\hat{\rho} = \hat{\rho} \tag{3.15}$$

Clearly for the maximum likelihood estimator ρ_0, $\hat{R}_\rho = \hat{\mathbb{1}}$. In a similar manner $\hat{\rho}\hat{R}_\rho = \hat{\rho}$ so that since $\hat{R}_\rho = \hat{R}_\rho^\dagger$,

$$\hat{R}_\rho \hat{\rho}_0 \hat{R}_\rho = \hat{\rho}_0. \tag{3.16}$$

If we managed to guess the correct estimator $\hat{\rho}_0$, equation (3.16) holds and the estimator is unaffected. If however our estimator does not maximize the likelihood, the operation $\hat{R}_\rho\hat{\rho}\hat{R}_\rho$ will produce a density matrix $\hat{\rho}'$ that is a closer approximation to $\hat{\rho}_0$. Intuitively, we can see how this works: if for a given angle, $\hat{\rho}$ overestimates the j$^{\text{th}}$ bin, we will have $f_{\theta,j} < pr_{\theta,j}$ and the projection operator for the corresponding bin in $\hat{\rho}'$ will be given less weight. Conversely, an underestimate in $\hat{\rho}$ leads to an increased weight for the projection operator for the corresponding $\hat{\rho}'$ bin. This is the principle behind the iterative approach to maximum likelihood estimation of a quantum state. Starting with an initial guess, we compute

$$\hat{\rho}^{(i+1)} = \left[\hat{R}_{\rho^{(i)}} \hat{\rho}^{(i)} \hat{R}_{\rho^{(i)}}\right] \mathcal{N} \tag{3.17}$$

until termination[10]. Here, $\mathcal{N}$ normalizes to a unitary trace which preserves positivity of the density matrix.

[10]Termination here could mean (i) a fixed number of iterations, (ii) A threshold likelihood, (iii) sufficiently low $|\hat{\rho}^{(i+1)} - \hat{\rho}^{(i)}|$, (iv) impatience.

The above algorithm is not guaranteed to converge and at least one counterexample has been concocted [65], but in our experience with real homodyne data, convergence is quickly reached. Furthermore, since the likelihood for quantum tomography is a convex function, if a maximum is found it is a global maximum so if after a number of steps the estimator is unchanged, there is a high probability that the correct estimator has been found. In order to test the validity of a particular reconstruction, the estimated density matrix may be used to simulate the quadrature data via equation (2.30) which are then compared to the experimentally acquired data.

Chapter 4

Producing Nonclassical Light: Four-Wave Mixing in Rb Vapour

In this chapter, we describe a source of nonclassical light known as Four-Wave Mixing (4WM) in atomic vapour. We first characterize the spectroscopic properties of the system in terms of experimentally accessible parameters. We then go on to describe and demonstrate the generation of relative-intensity squeezed and quadrature squeezed light. The demonstration of a high degree of squeezing in this system was recently reported elsewhere [31, 32, 66] and provided the initial motivation to use this system to produce arbitrary superposition states of light as has been done with SPDC [36].

4.1 Four-Wave Mixing

Under conditions of a propagating electromagnetic field oscillating at a frequency far from any atomic resonance, the response of a gas of atoms may be treated as a linear dielectric [67], having response[1],

$$\mathbf{P} = \varepsilon_0 \chi \mathbf{E} \tag{4.1}$$

χ being the electric susceptibility of the medium [67]. In the vicinity of atomic resonance, the response of the medium to an electric field is no longer linear. To accommodate this nonlinearity, the susceptibility can be treated as a tensor which describes the response to a given electric field as a function of external fields:

[1]Technically, no medium can respond instantaneously to an applied field so the correct form of (4.1) is $\mathbf{P}(t) = \varepsilon_0 \int_{-\infty}^{t} \chi(t-t')\mathbf{E}(t')dt'$ [68]

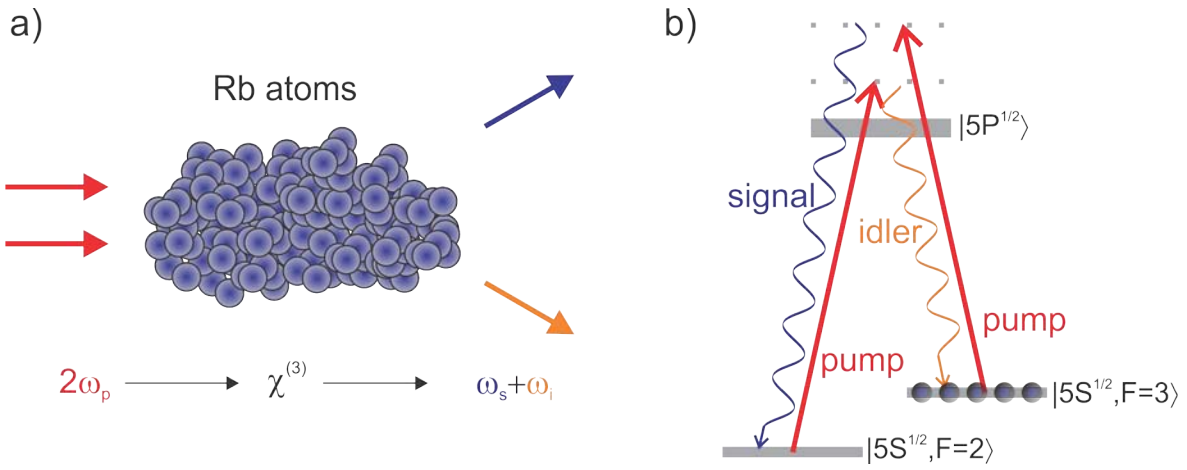

Figure 4.1: (a) Photon picture of 4WM process. Two pump photons are spontaneously annihilated, creating a signal and an idler photon. (b) Atomic level diagram showing the relative frequencies of the pump, signal, and idler photons. Note that both pump beams are derived from the same laser.

$$\mathbf{P} = \varepsilon_0 \tilde{\chi}^{(1)}\mathbf{E} + \varepsilon_0 \tilde{\chi}^{(2)}\mathbf{E}\mathbf{E} + \varepsilon_0 \tilde{\chi}^{(3)}\mathbf{E}\mathbf{E}\mathbf{E} + \cdots = \varepsilon_0 \sum_{n=1}^{\infty} \tilde{\chi}^{(n)}\mathbf{E}^n \tag{4.2}$$

where $\tilde{\chi}^{(n)}$ represents a tensor of rank n.

Since an isotropic medium such as an atomic vapour has a vanishing second order susceptibility [68] the first non-linear term is third order:

$$\mathbf{P}_i(\omega) = \varepsilon_0 \sum_{ijkl} \chi^{(3)}_{ijkl}\mathbf{E}_j(\mathbf{r}_j, t)\mathbf{E}_k(\ \mathbf{r}_k, t)\mathbf{E}_l(\mathbf{r}_l, t) + c.c. \tag{4.3}$$

where $\chi^{(3)}_{ijkl}$ is the third order susceptibility tensor for field $\mathbf{E}_i$, given fields $\mathbf{E}_j$, $\mathbf{E}_k$, and $\mathbf{E}_l$.

Equation 4.3 contains myriad terms[2], but the terms responsible for individual processes can be isolated based upon energy and momentum conservation. From figure (4.1), we see that conservation of energy for this process demands that

[2]In general $\chi^{(3)}$ contains 81 terms, each of which is a sum of 48 independent sums [69].

$$\omega_i = 2\omega_p - \omega_s. \tag{4.4}$$

and in terms of momentum:

$$\mathbf{k}_i = 2\mathbf{k}_p - \mathbf{k}_s. \tag{4.5}$$

Since we can write $\mathbf{E}_j(\mathbf{r},t) = \mathbf{E}_j e^{i(\mathbf{k}_j\cdot\mathbf{r}-\omega_j t)}$, we therefore identify the term describing the creation of the idler field from equation 4.3 as:

$$P_i(\omega_i) = \varepsilon_0 \chi^{(3)} \mathbf{E}_p^2 \mathbf{E}_s^* \tag{4.6}$$

where $\chi^{(3)} = \chi^{(3)}_{pps}$.

We assume that the electric field takes on the form of a plane wave with a slowly varying envelope amplitude along the z-axis $\mathcal{E}(z)$. Also, without loss of generality for our purposes, we neglect the tensor nature of $\chi^{(3)}$ and treat P and E as scalars. We therefore write $E_j(\mathbf{r},t) = \mathcal{E}(z)_j e^{i(k_j z-\omega_j t)}$. Equation (4.7) then can be written as:

$$P_i(\omega_c) = \varepsilon \chi^{(3)} \mathcal{E}_p^2 \mathcal{E}_s^* e^{i((2k_p-k_s)z-\omega_c t)} \tag{4.7}$$

where we have used equation (4.4) and assumed propagation in the z-direction for each field[3].

In order to study the dynamics of the system, we apply the paraxial wave equation.[4] solved in the steady state (all time derivatives are identically zero:)

$$\partial_z \mathcal{E}_i = i\frac{k_i}{2\varepsilon_0}\chi^{(3)} \mathcal{E}_p^2(z) \mathcal{E}_s^*(z) e^{i(2k_p-k_s-k_i)z} \tag{4.8}$$

[3]Experimentally, the fields propagate at a small angle with respect to one another but collinearity is assumed here for simplicity.

[4]i.e. we write the wave equation $(\nabla^2 - \partial_t^2)E = \frac{1}{c^2\varepsilon_0}\partial_t^2 P$ under the assumption that $\partial_z\mathcal{E} \ll k\mathcal{E}$, $\partial_t\mathcal{E} \ll \omega\mathcal{E}$ so that the second derivatives vanish.

We assume that the pump is sufficiently strong that the depletion (due to converted photons) is insignificant and so $\partial_z \mathcal{E}_p = 0$. Defining the phase mismatch $\Delta k \equiv 2k_p - (k_s + k_i)$ and the constant $\kappa \equiv \frac{k_i \chi^{(3)}}{2c\varepsilon_0} \varepsilon_0 c \mathcal{E}_p^2 = \frac{k_i \chi^{(3)}}{c\varepsilon_0} I_p$, we arrive at

$$\partial_z \mathcal{E}_i = i\kappa \mathcal{E}_s^* e^{i\Delta k z}. \tag{4.9}$$

Next we assume[5] that $k_i \approx k_s$ and write the equivalent equation for the signal beam (by swapping i with s) to arrive at the coupled amplitude equations for $\Delta k = 0$:

$$\begin{aligned} \partial_z \mathcal{E}_i &= i\kappa \mathcal{E}_s^* \\ \partial_z \mathcal{E}_s &= i\kappa \mathcal{E}_i^*. \end{aligned} \tag{4.10}$$

Differentiating the first equation and plugging in the second yields:

$$\partial_z^2 \mathcal{E}_i = |\kappa|^2 \mathcal{E}_i \tag{4.11}$$

yielding the solutions:

$$\begin{aligned} \mathcal{E}_i(z) &= Ae^{i|\kappa|z} + Be^{-i|\kappa|z} \\ \mathcal{E}_s(z)^* &= Ae^{i|\kappa|z} - Be^{-i|\kappa|z}. \end{aligned} \tag{4.12}$$

Solving for the constants A and B in terms of $\mathcal{E}_{i,s}(0)$, and defining $|\kappa|z \equiv \zeta$, we arrive at:

$$\begin{aligned} \mathcal{E}_i(\zeta) &= \mathcal{E}_i(0)\cosh(\zeta) + \mathcal{E}_s^*(0)\sinh(\zeta) \\ \mathcal{E}_s(\zeta) &= \mathcal{E}_s(0)\cosh(\zeta) + \mathcal{E}_i^*(0)\sinh(\zeta). \end{aligned} \tag{4.13}$$

[5]This approximation is valid since $\lambda_p \approx \lambda_i \approx \lambda_s$ in the system under study ($\frac{\lambda_s - \lambda_i}{\lambda_p} \approx 10^{-5}$)

Note that by replacing the field amplitudes with annihilation operators, we arrive at the two-mode squeezing transformation (A.5). However, in contrast to the classical case in which the unseeded process results in no signal or idler output fields, vacuum fluctuations can drive the process spontaneously leading to non-zero photon number in each field even in the absence of input fields. The classical picture is used when considering macroscopic properties such as gain and spectral characteristics, whereas the quantum formulation is required to predict squeezing and heralded state preparation.

Equation (4.13) implies that if we seed the process by sending a weak beam into the signal channel, this beam experiences amplification and an idler beam appears in the direction which satisfies phase-matching. According to equation (4.4), the signal and idler beams will occur at equal and opposite sides of the pump beam, separated in frequency by twice the ground state splitting.

Note that in the case of seeding the process with a weak seed beam ($\mathcal{E}_s(0) \equiv \mathcal{E}_0$, and $\mathcal{E}_i(0) = 0$) the intensity of the seed is increased by a factor $\cosh^2(\zeta) \equiv G$ producing an amplified idler, and a signal is created with intensity $I_s = \sinh^2(\zeta) I_0 = (G-1) I_{seed}$. The ratio of idler to signal intensities is thus:

$$\frac{I_i}{I_s} = \frac{G-1}{G}. \tag{4.14}$$

4.2 Classical Characterization of the System

The first step in the work described in this thesis was to obtain evidence that we had a system described by the above analysis. To this end we set up an experiment to observe gain and idler beam creation in a hot atomic vapour cell. The simplified experimental diagram is shown in figure 4.2. A weak coherent state seeds the process by overlapping with the pump at a small angle throughout the atomic vapour cell. This angle was chosen

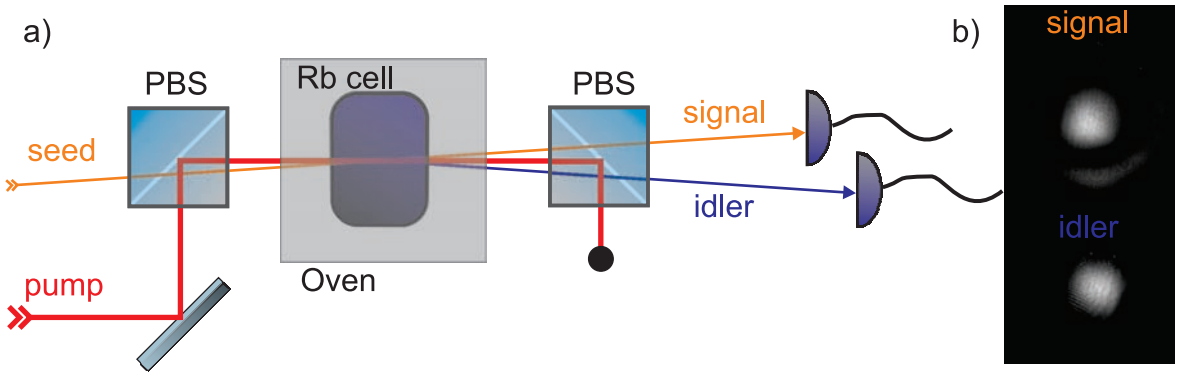

Figure 4.2: (a) Simplified diagram of experiment to detect four-wave mixing. The pump is derived from a titanium sapphire Laser while the seed originates from an ECDL. (b) CCD image of signal and idler beams produced in the vapour cell.

large enough to spatially separate the signal and idler fields but small enough that residual Doppler effects were negligible and phase-matching was met (discussed below). The cell contains isotopically pure ^{85}Rb vapour and is maintained at a temperature of roughly 130°C inside an insulating oven. The windows are antireflection coated for $\lambda = 795$ nm and the length of 12 mm is chosen so that the seed and pump interact throughout the entirety of the cell. The pump by was derived from a Coherent MBR 110 titanium sapphire laser (Ti:Sa) which was fiber coupled from a separate laboratory. The e^{-2} radius of the pump beam was 500 μm and the power was varied from 200 mW to 1W. The seed beam was generated with an external cavity diode laser (ECDL) which we constructed in the lab [70]. The beam was orthogonally polarized to the pump with radius 350 μm and had a power on the order of 100 μW. The beams were combined on a polarizing beam splitter and overlapped at an angle of 5 mrad at the centre of the vapour cell.

Figure 4.3a shows the spectrum of the signal beam after passing through the medium as in figure 4.2a. The pump was tuned ≈ 1 GHz red of the $\left|5S^{1/2}, F = 2\right\rangle \rightarrow \left|5P^{1/2}, F'\right\rangle$ transition[6]. The signal beam experienced standard absorption from the two ground to

[6]Due to Doppler broadening, the hyperfine levels of the 5P excited state are not resolved individually.

excited state transitions. However, whenever the magnitude of the frequency difference between pump and probe equaled the ground state splitting of approximately 3 GHz, sharp gain peaks were observed which are accompanied by the creation of an idler beam in the phase-matched direction (eq. (4.5)).

The phase-matching condition caused the gain peak to be sensitive to alignment. Since the idler is automatically generated in the phase-matched direction, a natural question to ask is, "what does it mean to be phase matched here"? Defining $\theta_{s(i)}$ to be the angle between the pump and the signal (idler) and noting $ck = n_\omega \omega$, phase matching implies that:

$$\begin{aligned} n_i \omega_i \sin\theta_i &= n_s \omega_s \sin\theta_s \\ n_i \omega_i \cos\theta_i &= 2 n_p \omega_p - n_s \omega_s \cos\theta_s \end{aligned} \tag{4.15}$$

are both simultaneously satisfied. This occurs for particular values of $n_{i,s,p}$ which are in turn functions of frequency and pump power. As opposed to nonlinearities in crystals and cavities where generation can be obtained for a very small range of angles, the phase-matching condition in the hot vapour cell was less stringent. This was primarily due to the large Fresnel number[7] configuration of our setup. The Rayleigh range of our beams were on the order of 100 times longer than the vapour cell so that beam divergence could be neglected and the process could be stimulated for a large range of angles. To obtain a rough estimate of this angular range, note that approximating $|\mathbf{k}|_p \approx |\mathbf{k}|_s \approx |\mathbf{k}|_i$ and $\theta_s \approx -\theta_i$, the phase matching condition $\Delta k L \ll 1$ reads

[7]The Fresnel number is defined as the ratio of interaction length to the beam waist.

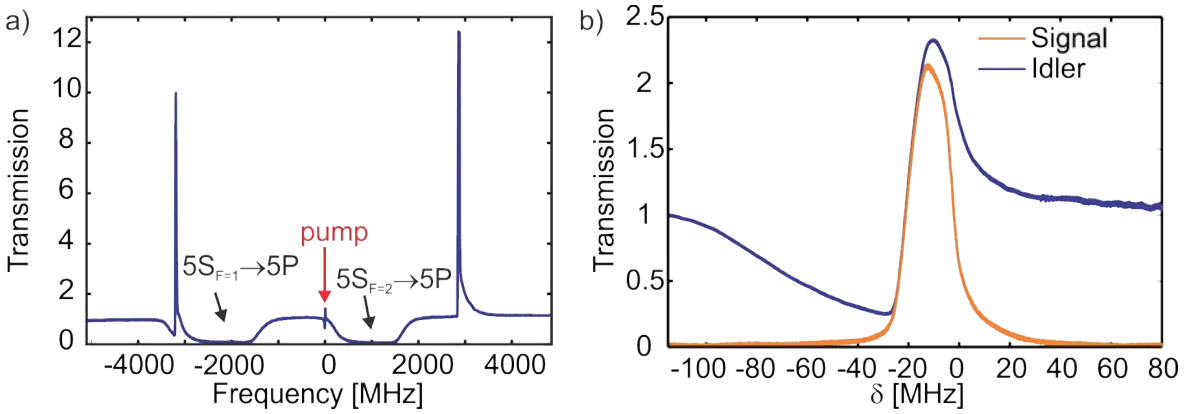

Figure 4.3: (a) Measured spectrum of the probe experiencing four-wave under high gain conditions ($T_{atoms} = 135°\text{C}$). The two gain peaks at a frequency difference with the pump of the hyperfine ground-state splitting.(b) Simultaneous monitoring of the signal gain and idler creation for lower gain conditions ($T_{atoms} = 110°\text{C}$).

$$\begin{aligned} 1 &\gg 2kL(1-\cos\theta) \\ &\approx 2kL(1-(1-\theta^2/2) \\ &= \frac{2\pi L}{\lambda}\theta^2 \end{aligned} \tag{4.16}$$

so that the approximate angular phase-matched range is thus

$$\theta_{pm} \approx \sqrt{\frac{\lambda}{2\pi L}}. \tag{4.17}$$

With our parameters, this corresponds to $\theta = \pm 5$ mrad. This is consistent with our observations in which we found that gain was present anywhere between $\theta_s = 1$ mrad to around 10 mrad, with maximal gain occurring at $\theta_s \approx 5$ mrad.

Ideally, the gain increases dramatically with temperature: the susceptibility is linearly proportional to number density [69], but the gain is exponential in $\chi^{(3)}$ and number density increases approximately exponentially with temperature (see figure (4.4a)), predicting super-exponential scaling. Experimentally however we found that the gain initially

increased exponentially, but tapered off at a temperature of about 150 °C corresponding to a number density of 10^{14} cm^{-3} at which point additional nonlinear interactions began to dominate. One such interaction was self focusing of the pump [71], which destroyed the phase-matching as has been reported elsewhere [72].

A dramatic additional nonlinear effect was the appearance of pump-induced, incoherent blue fluorescence starting at around $T = 130$ °C. We first noticed the effect when exploring the scaling of idler power with temperature and found that near atomic resonance, a pump with power of several hundred mW was completely absorbed. When viewing the oven to see if anything was obscuring the beam, we noticed the pump depletion was accompanied by an omnidirectional blueish glow. Spectroscopic measurements determined that the fluoresced light had a wavelength of 422 ± 4nm which was consistent with the $6P^{3/2} \rightarrow 5P^{1/2}$ transition at 420 nm. One puzzling aspect of this generation is that there is no transition in the neighbourhood of 397.5 nm, so our laser could not be directly driving a two photon excitation. This effect has also been seen in a separate experiment in our lab and has been mentioned in the supplementary information in [73]. The dependence on high temperature suggests the process is due to collisional-enhanced multi-photon excitation. In this case, the excited atom cascades back down to the ground state through $6P^{3/2} \rightarrow 5P^{1/2}$. This phenomenon, known as an energy pooling process was studied in Rubidum in 1983 by Barbier and Cheret [74], and has been exploited to produce coherent 420 nm generation [75, 76].

From equation (4.14), we could infer the gain by noting the resultant output powers. However, if we simply measure P_{signal}/P_{seed} we would underestimate the 4WM gain owing to the residual absorption from atomic resonance. The idler beam however was created much farther off resonance, did not suffer this absorption, and was thus a more reliable indicator of 4WM gain. Ideally, the idler power was directly proportional to input power $P_i = (G-1)P_{seed}$.

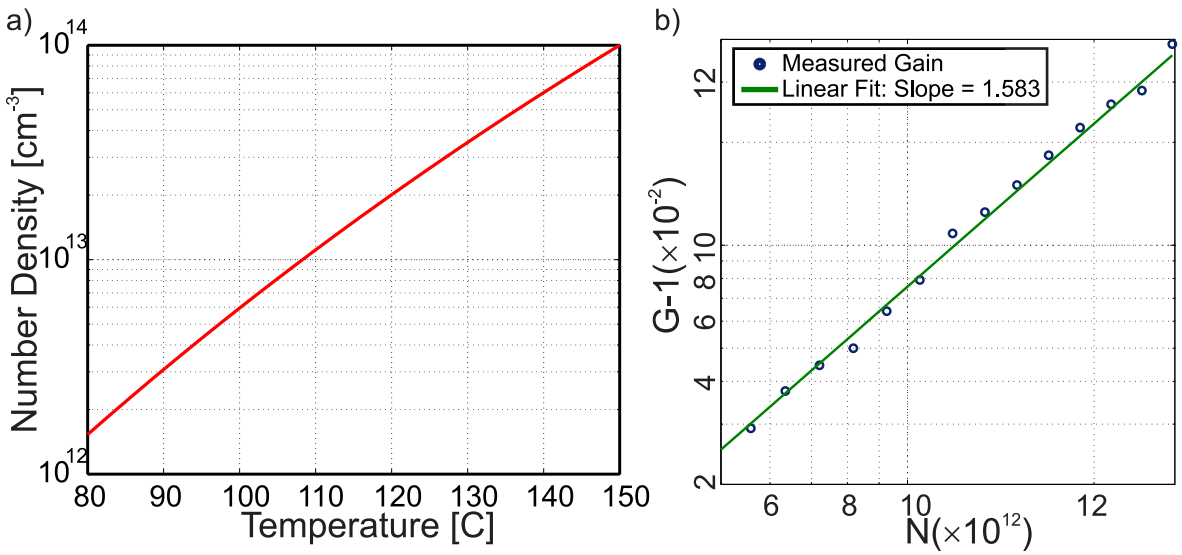

Figure 4.4: (a) The expected scaling of number density with temperature, where the ideal gas approximation was assumed and the vapour pressure was modelled as described in [1]. (b) The scaling of gain with number density over the range of temperatures used in the experiment. Gain was inferred by the idler power and number density was obtained as in (a).

As mentioned, one naively assumes super-exponential scaling of the 4WM gain with temperature. However, additional process discussed above which degrade the effective gain of the system also become more pronounced with number density and we expect less dramatic scaling in a realistic setting. In order to quantify this scaling experimentally, we monitored the measured gain via the idler beam power as a function of temperature. From the temperature we could calculate the number density, as shown in figure 4.4a[8]. Figure 4.4b shows the measured scaling which, on a log-log plot, gives approximately linear behaviour with slope 1.58. Over the range of temperatures accessed in the experiment, the gain thus scaled roughly as: $G - 1 \approx N\sqrt{N}$.

The dispersive nature of the lower frequency gain peak in figure 4.3 was due to the

[8]We use the Clausius Clapeyron relation with constants stated in [1] to determine the vapour pressure in the liquid phase as a function of temperature. We then determine the number density directly from the ideal gas relation $N \equiv n/V = P/k_B T$, k_B being the Boltzmann constant.

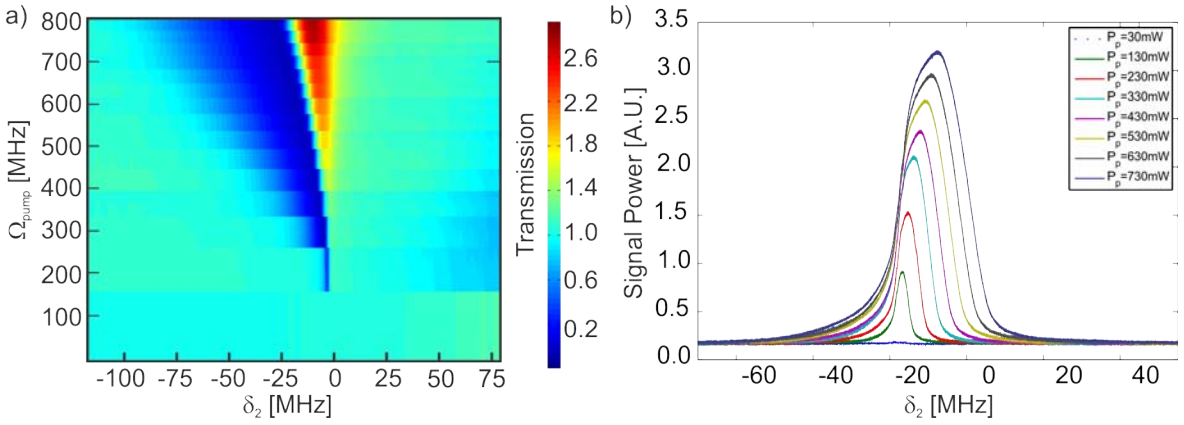

Figure 4.5: (a) The transmission profile of the seed(idler) for increasing pump intensity. The red region displays the gain peak while the dark blue region is Raman absorption. (b) The transmission spectrum of the created signal where each trace corresponds to a horizontal slice of (a).

interplay between four-wave mixing gain and Raman absorption [31], indicative of the complicated interplay of effects present in the setup. The higher frequency gain peak was farther from atomic resonance and did not exhibit the same complicated profile. This implied that for the observation of correlations between signal and idler photons, it was preferable to seed the process at a slightly higher frequency than two-photon resonance in order to minimize the loss in the system.

The most accessible experimental parameter controlling the gain was the pump power. Increasing the pump Rabi frequency[9] Ω_p more efficiently drove coherence between the ground-states and overcame the degrading effects of population exchange. On the other hand, the Rabi frequency broadened the line-width of two-photon transitions, which was detrimental for the generation of quantum light compatible with atomic transitions. In figure 4.5a, the signal spectra for a range of pump Rabi frequencies is displayed. The gain peak is seen to shift as a result of the AC-stark effect and the Raman absorption dip

[9]The Rabi frequency for the $|i\rangle\langle j|$ transition is given by $\Omega = \frac{\mathbf{d}_{ij}\cdot\mathbf{E}}{\hbar}$, $\mathbf{d}_{ij}$ being the transition dipole moment for the given atomic transition.

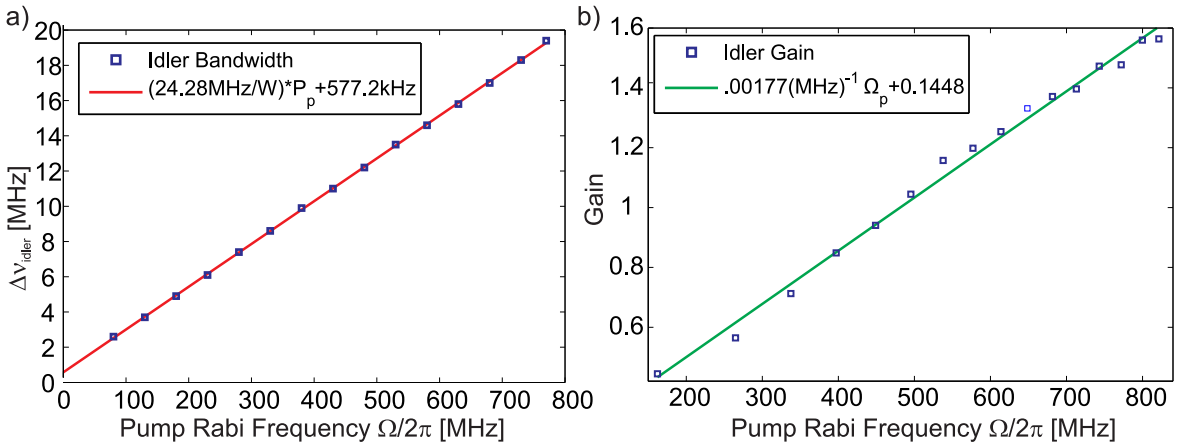

Figure 4.6: (a) The idler bandwidth was seen to increase linearly with pump Rabi frequency. Here the bandwidth is defined to be the full width at half-max of the idler profile (fig 4.5b). (b) Similarly, the gain was seen to increase linearly with pump Rabi frequency. This is in contrast with the theoretical prediction of $G \propto e^{c_0 \Omega_p^2}$ implying the presence of additional processes such as self-focusing.

becomes significantly broader. Figure 4.5b shows the generated idler spectrum for each pump power. It is apparent that the idler creation is attenuated as a result of Raman absorption of the signal and thus becomes asymmetric. The bandwidth of the generated field is also seen to increase with pump power. This is an important measurement since it is the width of the signal gain peak that ultimately determines the bandwidth of the system. This is quantified in figure 4.6, where both the gain and the bandwidth are seen to be linear in pump Rabi frequency. Converting the Rabi frequency back to optical power of the 500 μm pump beam shows that the bandwidth increases as 24.28 MHz per Watt of pump power.

Owing to the fact that the process was operated far off atomic resonance, the gain was fairly insensitive to the one-photon detuning of the pump beam. This is fortunate as it implies that the light generated by the 4WM system was tuneable. Although the signal was produced far off resonant to the ^{85}Rb system it was created in, it could be made directly resonant to the $\left|5S^{1/2}, F = 1\right\rangle \rightarrow \left|5P^{1/2}, F'\right\rangle$ transition of ^{87}Rb by tuning the

pump red- instead of blue-detuned from the excited manifold. This was the configuration which produced the most squeezing but the photon experiment was optimized for the blue-detuned case. Consequentially, the light generated could be directly interfaced with resonant atom-based quantum memories and logic gates employing ^{87}Rb.

4.3 Relative Intensity Squeezing

4.3.1 A Brief Theoretical Description

The standard quantum limit (SQL) for intensity noise is set by the Poissonian limit: $\langle \Delta n^2 \rangle \geq \bar{n}$. The ultimate violation of this limit is the Fock state for which $\langle \Delta n^2 \rangle = 0$. For two separate beams occupying modes a and b respectively, the *relative intensity noise* between these modes is:

$$\left\langle \Delta(n_a - n_b)^2 \right\rangle = \left\langle \Delta n_a^2 \right\rangle + \left\langle \Delta n_b^2 \right\rangle - 2\mathrm{cov}(n_a, n_b), \tag{4.18}$$

where $\mathrm{cov}(n_a, n_b) = \langle n_a n_b \rangle - \langle n_a \rangle \langle n_b \rangle$ is the covariance between the photon number in each channel. For uncorrelated modes, this covariance vanishes and the relative intensity noise is the sum of the individual beams' intensity noise. Two coherent states in separate modes thus behave as a coherent state with $|\alpha|^2 = |\alpha|_a^2 + |\alpha|_b^2$ and define the two mode SQL for intensity noise.

Relative intensity squeezing was first observed in 1987 in which an optical parametric oscillator resonant to two separate modes produced bright twin beams with relative intensity squeezing of 1.55 dB below the SQL [77]. Relative intensity squeezed beams have a number of practical applications include quantum imaging [78], high sensitivity spectroscopy [79], and measurement of extremely weak optical attenuation [80].

Operationally, our 4WM system amplifies the seed beam by scattering one pump photon into the signal channel and another into the idler channel. Whereas the mean

photon number is increased, the relative intensity noise is unaffected since the added light is, loosely speaking, a "two-mode Fock state" $|n_a, n_b\rangle$.

To get a quantitative understanding, we assume that the signal channel is a coherent state of mean photon number $|\alpha|^2$, the idler channel is initially vacuum, and proceed in the Heisenberg picture:

$$|\psi\rangle = \hat{S}_{si}(\zeta)\hat{D}_i(\alpha)\,|0_i\rangle\,|0_s\rangle\,. \tag{4.19}$$

Using the properties of the two-mode squeezing operator in equation (A.5) and the displacement operator in equation (2.18), we find (see appendix D for details):

$$\begin{aligned} \langle\hat{n}\rangle_i &= |\alpha|^2\cosh^2(\zeta) + \sinh^2(\zeta) \\ \langle\hat{n}\rangle_s &= (|\alpha|^2 + 1)\sinh^2(\zeta) \end{aligned} \tag{4.20}$$

In the limit of large mean photon number (even a humble 100 μW laser beam has $|\alpha|^2 \approx 10^{10}$) this reduces to equation (4.14) from the classical calculation with $G \equiv \cosh^2(\zeta)$. However, as opposed to the classical derivation the mean photon number in each channel is nonzero and is given by $\sinh^2(\zeta) = G - 1$ in the absence of input coherent state. This vacuum-stimulated 4WM process leads to squeezed vacuum discussed in the next section and forms the basis of the narrowband photon source presented in chapter four.

Proceeding with the calculations of the individual terms in equation (4.18), the individual variance of each channel is:

$$\begin{aligned} \langle\Delta\hat{n}_i\rangle^2 &= |\alpha|^2\cosh^2(\zeta)(\cosh^2(\zeta) + \sinh^2(\zeta)) + \cosh^2(\zeta)\sinh^2(\zeta) \\ \langle\Delta\hat{n}_s\rangle^2 &= |\alpha|^2\sinh^2(\zeta)(\cosh^2(\zeta) + \sinh^2(\zeta)) + \cosh^2(\zeta)\sinh^2(\zeta). \end{aligned} \tag{4.21}$$

Note that for large α, $\langle\Delta\hat{n}_i\rangle^2 = |\alpha|^2 G(2G-1)$ whereas for a coherent state of the same optical power, $\langle\Delta\hat{n}\rangle^2 = |\alpha|^2 G$. Therefore, the amplified seed beam itself is no longer a

minimum uncertainty state in terms of intensity, and carries an extra factor $2G-1$ of extra noise. In the case of no seed $|\alpha| = 0$, $\langle \Delta \hat{n}_s \rangle^2 = \langle \Delta \hat{n}_i \rangle^2 = \cosh^2(\zeta) \sinh^2(\zeta)$.

Computing the covariance term in (4.18) and computing the sum yields:

$$\left\langle \Delta (n_s - n_i)^2 \right\rangle = |\alpha|^2 \tag{4.22}$$

This is the root of the relative intensity squeezing effect - the total noise on the difference signal is equal only to that of the input beam. Since the process results in gain, the optical power can be much greater than that of the input state while the noise is equivalent to that of a coherent state of much less power. In order to quantify this effect, we can compare the noise of the twin beams to that of a coherent state of equal optical power and obtain the relative intensity noise normalized to the standard quantum limit for intensity noise:

$$RI = \frac{\langle \Delta (\hat{n}_s - \hat{n}_i)^2 \rangle}{\langle \Delta \hat{n}_{CS}^2 \rangle}. \tag{4.23}$$

Using $\langle \Delta \hat{n}_{CS}^2 \rangle = (2G-1) |\alpha|^2$ from eq. (4.20), we obtain for the 4WM process:

$$RI = \frac{1}{2G-1}. \tag{4.24}$$

Note that a value of $RI < 1$ implies non-classicality (see section 2.5.3), an effect known as relative intensity squeezing. Since $G \geq 1$, the process always results in squeezing, provided that there is no extra noise and the channels experience no loss. Under these assumptions the squeezing is monotonic with gain. This is not the case when losses are present since in the presence of gain, the individually noisy channels are carefully balanced. Loss in one channel breaks this balance and for large gains the excess noise quickly grows above the noise level of a coherent state of the same optical power. Loss $L \equiv 1 - \eta$ can be modelled by a beam splitter with transmissivity $\eta_{s(i)}$ in the signal (idler)

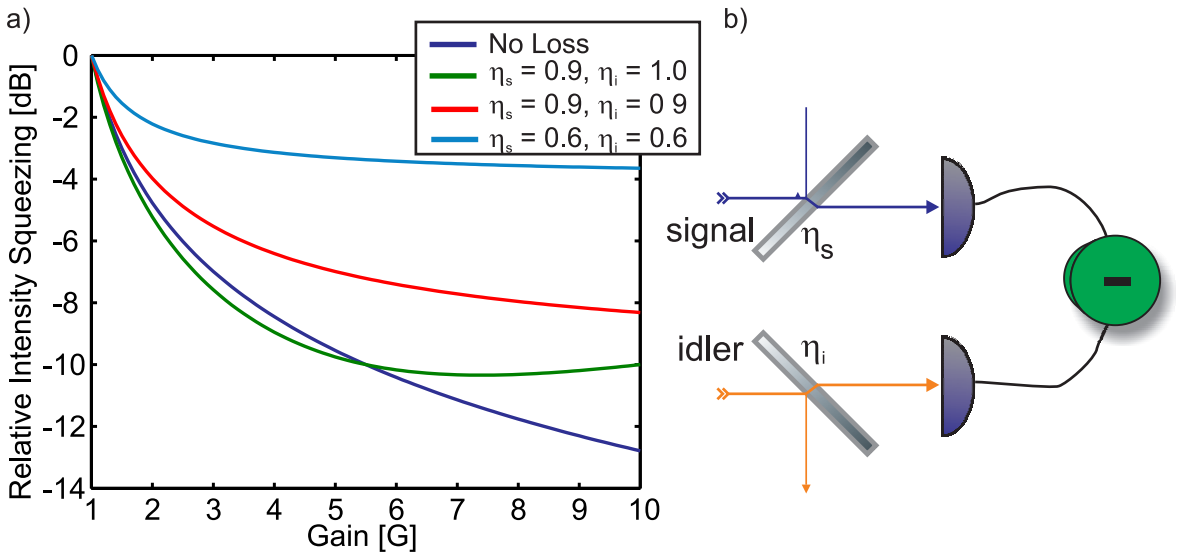

Figure 4.7: (a) Theoretically predicted relative intensity squeezing in the presence of loss. In the presence of loss the amount of squeezing obtained is not monotonically decreasing with increasing gain. (b) Loss in the signal (idler) channel is modelled as a beam splitter of transmissivity $\eta_{s(i)}$ and a vacuum state incident on the reflecting port

channel [39]. The corresponding expression for (4.24) using this model is calculated in the appendix D. Figure 4.7 shows the predicted relative intensity squeezing in the presence of loss. Note that owing to the imbalance of input powers (equation (4.14)) optimal squeezing for low gain is obtained with slight loss on the probe channel. This counter-intuitive result has been pointed out elsewhere [81].

4.3.2 Experimental Results

A large amount of time was devoted to the observation of relative intensity squeezing. After much experimentation, it was determined that phase stability between the pump and seed beams was an extremely crucial parameter and even an almost unnoticeable amount of technical noise on the input beam will be amplified to well above the standard quantum limit. This is discussed in more detail in the next section.

Figure 4.8 displays the experimental configuration with which relative intensity squeez-

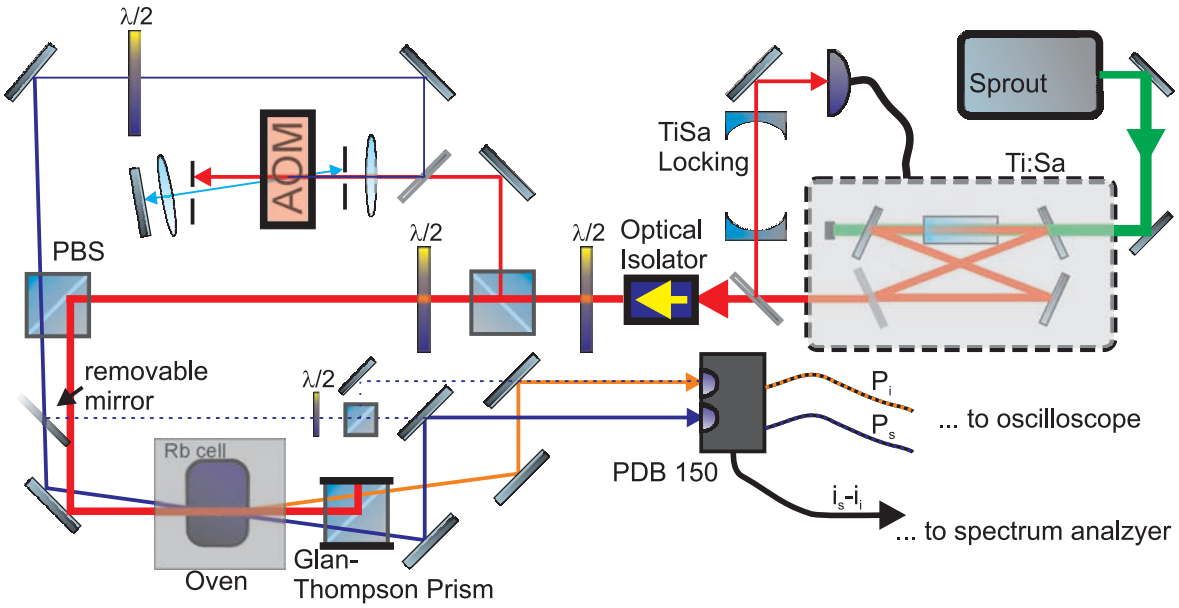

Figure 4.8: The final configuration of the experimental setup to observe relative intensity squeezing. The dotted path accessible by the removable mirror allows for the calibration of the standard quantum limit.

ing was eventually observed. The pump is derived from a Tekhnoscan TIS-777 titanium sapphire ring resonator laser (Ti:Sa) driven by a *Lighthouse Photonics* Sprout 8W 532 nm pumping laser. The Ti:Sa provided up to 1.3W of 795 nm light with extremely narrow line width ($\Delta\nu < 5$ KHz). A small fraction of this light was passed to a Brimrose GPM-400-1600 acousto-optical modulator (AOM). The first-order sideband was shifted by about 1.5 GHz and was counter-propagated back into the AOM to produce a beam phase-stable with an adjustable two photon detuning roughly equal to the ground state splitting frequency of ^{85}Rb of 3.035 GHz. This "double-pass" configuration had the draw-back of limited seed power since the single pass efficiency was $< 20\%$ leading to a double pass efficiency of a few percent. The small active aperture of the acoustic crystal ($\approx 25\mu$rad) and the optical damage threshold of 5W/mm^2 led to a maximum input power of about 10 mW and thus a maximum seed power of about 200 μW. The AOM also introduced elliptical divergence on the beam which required cylindrical lenses to cor-

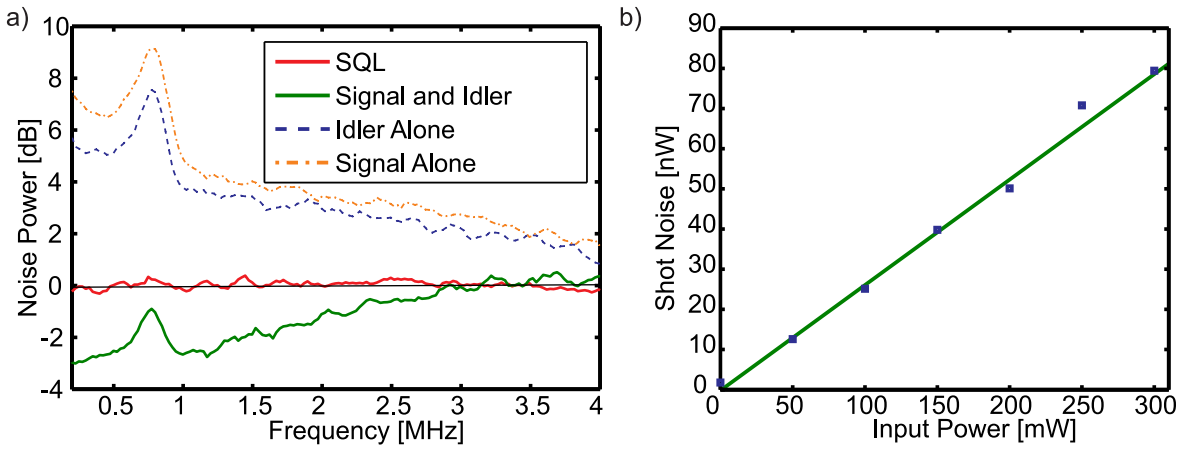

Figure 4.9: (a) Relative intensity squeezing. The dotted curves are the signal and idler beams alone incident on one of the detectors, each of which is much noisier than the measured SQL (red) However, when both beams are simultaneously incident on the detectors, the resultant noise (green) is below the SQL. (b) Calibration of the SQL for our detectors. Linearity of measured noise with respect to optical power implies that the signal is not polluted with classical noise.

rect. Despite these drawbacks, the double-pass AOM configuration was the only method by which we obtained sufficient pump-seed phase stability to observe relative intensity squeezing.

The pump and signal beam were set to orthogonal polarizations via half-wave plates ($\lambda/2$ in the figure) and sent at an angle of about 5 mrad through the 115 °C atomic vapour cell. The pump was isolated after the cell by means of a Glan-Thompson polarizer and the signal and idler beams were separated and directed to a Thorlabs PDB 150C differential detector. The detector was custom designed to make use of Hamamatsu S3883 photodiodes which had a nominal quantum efficiency of 91%. Individual outputs allowed us to observe the output power of each beam separately while the difference photocurrent was monitored on a spectrum analyzer. The SQL was calibrated by sending the seed beam around the cell and adjusting the power to that of the total 4WM output light. An SQL calibration curve for the detector we used is displayed in figure 4.9b.

Figure 4.9a summarizes the results found in the relative intensity experiment. In this plot, the pump power was 760mW and was detuned about 800 MHz red of the $F = 1 \rightarrow F'$ transition. The traces are presented on a logarithmic scale with respect to the measured SQL for the experiment. Here the power of the signal and idler beams was 72 μW and 78 μW respectively and the SQL was calibrated for a coherent state of power 150 μW. The residual absorption of the near-resonant seed (see figure 4.3) led to a signal with higher power than the idler, in contrast to equation (4.14). The intensities of the signal and idler were individually much noisier than the SQL when incident on the detector individually, but when both beams were incident simultaneously the noise was dramatically reduced, reaching as far as 3 dB below the SQL. The noise peak at around 800 kHz was due to technical noise present on the Ti:Sa beam which could not be perfectly cancelled out by the limited common mode rejection ratio of the differential detector. The intensity correlations extended out to 3 MHz and at higher frequencies the difference signal was slightly above the standard quantum limit owing to uncorrelated emission from the atomic ensemble.

4.3.3 The Effect of Technical Noise on Intensity Squeezing

The most important requirement for relative intensity squeezing was a high degree of phase stability between the pump and seed beam and a great deal of time was spent achieving this. An intuitive reason for this is that we are measuring correlations in the sidebands of the relative intensity spectrum (see figure 4.9a). Phase noise manifests itself as modulation of the carrier signal and in the frequency domain, the sidebands then measure a bright, uncorrelated signal in place of vacuum fluctuations.

Originally, the pump beam was coupled into the experiment from a Ti:Sa in a separate laboratory and we generated the seed beam from a separate laser which was phase locked to the pump [82]. While this created a narrow beat frequency between the two

beams and thus a low phase variance, the digital locking signal created spurious sidebands which, when amplified in the 4WM system, overwhelmed the intensity noise. This led to an initial "false positive" for squeezing: We originally configured the SQL by sending the phase-locked signal beam through the atoms, split it on a 50:50 beam splitter, and subtracted the photocurrent as in figure 3.1. However, when the signal was phase locked, the gain property of the 4WM system amplified the lock-induced sidebands and produced a noise level well above the case when the SQL is measured by a beam which did not propagate through the atoms. The measured relative intensity noise between the signal and idler, while far below the falsely-calibrated SQL, was above the true SQL. This excess noise from the atomic gain was identified by shifting the locked pump-signal frequency difference away from the atomic two-photon resonance determined by the hyperfine splitting, and is shown in figure 4.10. In order to circumvent this problem, we moved to the double-pass AOM setup described in the last section. In this configuration, the phase noise is eliminated since each beam stems from the same source and the relative path difference is well within the Ti:Sa laser's coherence length.

An additional source of noise turned out to stem from the fiber coupling the pump light from a separate lab. At high optical powers, the fiber began to introduce uncorrelated noise into to pump beam which could not be subtracted away by the CMRR of the detector. This phenomenon was most likely due to 4WM process within the single-mode which begin to appear around a few hundred mW of power [83]. Figure 4.10b shows the evidence for this noise source: the beam was passed through the fiber for various input powers, attenuated to a fixed level and the sum and difference photocurrent was monitored, as described in figure 4.10. For powers above 500 mW, the fiber-induced technical noise dominated above the shot noise level. The only way to get around this noise source was to obtain, with some reluctance, a new titanium sapphire laser for our lab, which finally allowed us to observe the relative intensity squeezing of figure 4.9.

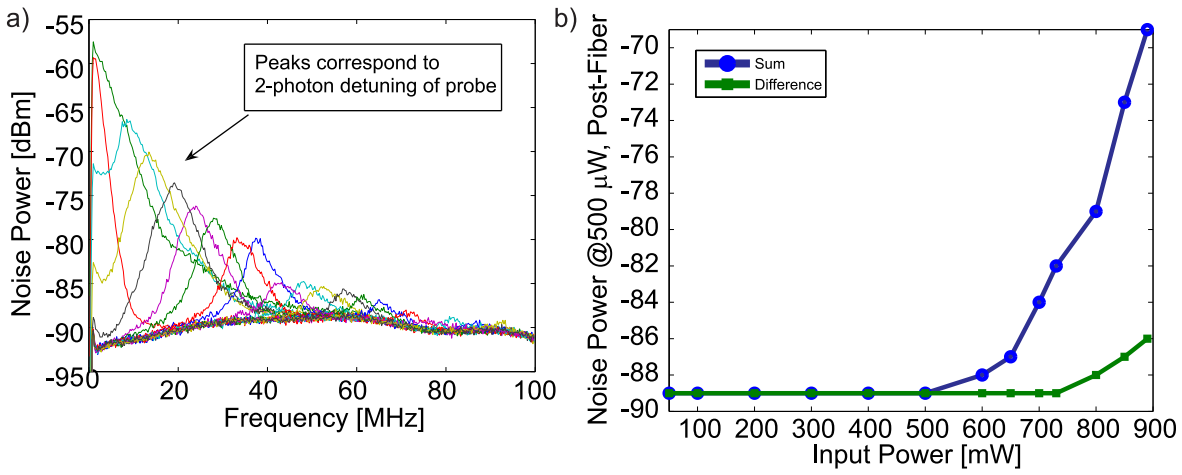

Figure 4.10: (a) The sidebands induced by the optical PLL added significant technical noise to the seed beam. Here each trace represents a different two photon detuning from the Raman transition between ground states $\delta_2 \equiv \omega - \omega_{HF}$. The peak value of each trace corresponds to the chosen value of δ_2. (b) At high optical powers, the fiber coupled Ti:Sa light acquired significant technical noise. Both noises in (a) and (b) destroyed the intensity squeezing.

4.4 Quadrature Squeezing

4.4.1 Basic Theory

Just as the 4WM system produced two-channel correlations between the photon number of the signal and idler fields, the process can also produce correlations in the joint quadrature of the fields. Instead of the non-local photon number, $\langle \Delta(\hat{n}_s - \hat{n}_i)^2 \rangle$, we can observe the non-local joint-quadratures described by equation (2.22). Since the photocurrent in a balanced homodyne detector placed in the signal(idler) channel is directly proportional to the single mode quadrature $\hat{x}_{s(i)}$ via equation (3.1), subtracting the photocurrent from matched homodyne detectors in each channel measures the joint quadrature. By scanning the phase of one detector with respect to another we can measure the two-mode squeezed state at all quadratures and fully characterize the output state.

As in the case of relative intensity squeezing, the quadratures of the individual chan-

nels are noisy, but correlated with one another so that when combined, they can exhibit noise below the standard quantum limit (2.6). The quantity measured in our experiments was the quadrature variance, measured as the noise power in the homodyne detector. Since the mean quadrature value of the squeezed vacuum state is zero, the variance is just the mean-square and we see from (2.24) that

$$\left\langle \Delta \hat{X}_{\pm}^{2} \right\rangle_{sq} = \frac{1}{2} e^{\pm 2\zeta}. \tag{4.25}$$

Squeezing is frequently measured on a logarithmic scale, so that in the ideal case of a pure squeezed vacuum, the variances of the squeezed (S) and anti-squeezed (A) quadratures are equidistant above and below the SQL. In a linear scale, the SQL is often normalized to 1, so that $S = 1/A$. Since the individual quadratures are very noisy[10], the fact that the TMSS is a minimum uncertainty state relies on careful subtraction. In the presence of loss, this subtraction is incomplete and results in extra noise.

The quality of a measured squeezed state can be quantified directly by observing the squeezed and anti-squeezed quadratures and introducing the generalized efficiency η_{sq} [84]. This model supposes that we start with a pure squeezed state and subject it to loss by passing it through an attenuator with transmissivity η_{sq}. By observing an imperfect squeezed state in our experiment, we can then seek the equivalent transmissivity that would give our results, supposing an initially pure squeezed state from the 4WM process. On a linear scale, with squeezing S and anti-squeezing A,

$$\eta_{sq} = \frac{A + S - (AS + 1)}{A + S - 2}. \tag{4.26}$$

Clearly, for an ideal squeezed state ($AS = 1$) $\eta_{sq} = 1$. An important figure of merit is the amount of squeezing required for an efficiency of at least 50% regardless of the anti-squeezing. Solving the above equation for $\eta_{sq} = 1/2$ yields $S = \frac{A}{2A-1}$, which in the

[10]Even for a gain $G = 2$, the variance of an individual channel is thrice the SQL.

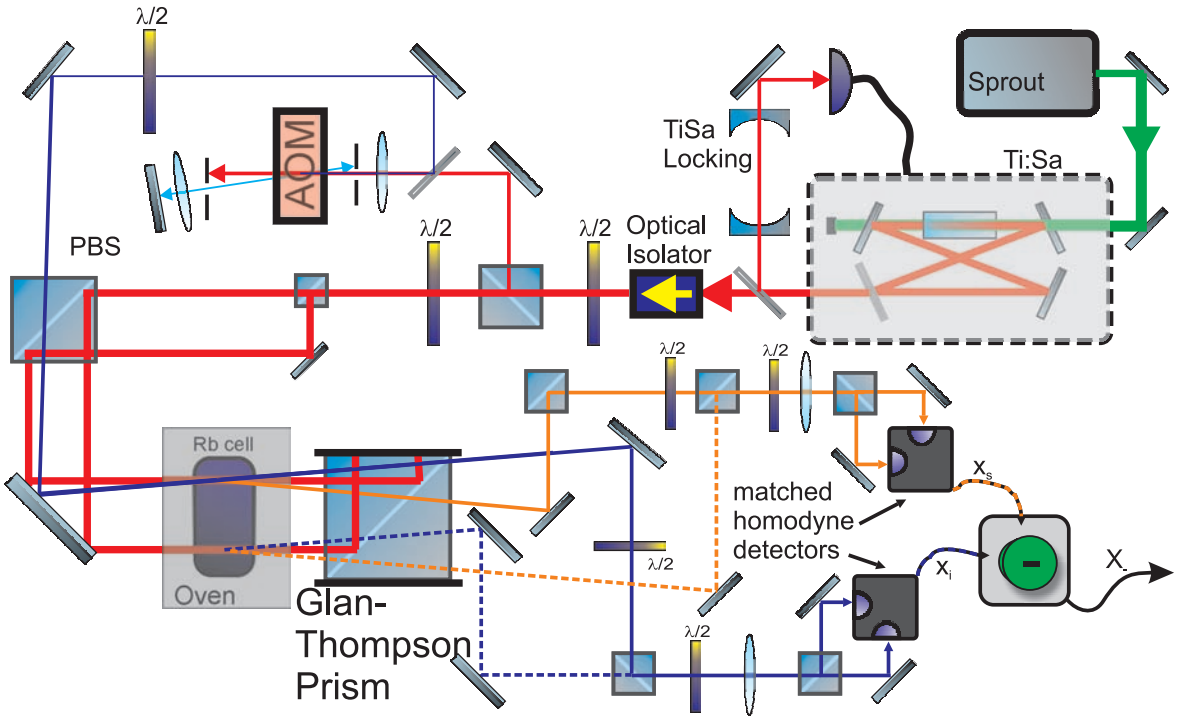

Figure 4.11: The experimental setup for the two-mode squeezing experiment. The local oscillators were produced via a separate 4WM process. The local oscillator and signal beam for each channel were overlapped and sent to individual homodyne detectors. The joint quadratures were extracted by subtracting the outputs of the individual homodyne detectors on a hybrid junction.

limit $A \to \infty$ becomes 1/2 or equivalently -3 dB. Thus any setup displaying at least 3 dB of squeezing displays a squeezed state of efficiency $\eta_{sq} > 0.5$ regardless of anti-squeezing.

4.4.2 Experimental Details

The experimental setup used to produce and detect quadrature squeezing is shown in figure 4.11. In order to mode-match the frequency and transverse mode of the two-mode squeezed vacuum state to the local oscillators required for homodyne detection, we followed the approach of [32] and generated the local oscillators dynamically by seeding a separate 4WM in the same atomic vapour cell. This was crucial during the initial phases

of the experiment since we needed to explore the multidimensional parameter space[11] in search of an suitable operating regime, and the transverse mode of the signal and idler depended to some extent on each of the parameters. Producing the local oscillators in the same 4WM system as the squeezed state thus allowed us to monitor the effect of varying the experimental conditions without realigning the homodyne detection setup. In addition the local oscillators were automatically generated in the correct frequency, forgoing the need for additional lasers or AOMs.

We measured the joint quadratures by subtracting the output of the individual homodyne detectors in each channel on a hybrid junction (M/ACOM H9sma). To observe the phase-dependent quadrature phase, we introduced a delay in the signal channel via a piezo-electric transducer while monitoring the output of the hybrid junction on a spectrum analyzer. The standard quantum limit was calibrated by simply blocking the two-mode squeezed vacuum modes before mixing with the local oscillator.

In order to measure the joint quadratures, it was imperative that the electronic response of the individual homodyne detectors were matched. To this end, we manufactured two identical homodyne detectors with matched surface mount components and an adjustable gain for fine tuning. To compensate for the imbalance in power between the seeded signal and idler beams described in the last section, we attenuated the stronger of the two signals so that the local oscillators had equal power. In this case equation (3.1) gives: $\hat{i}_- = \hat{i}_s - \hat{i}_i = \sqrt{2}\gamma\frac{\hat{x}_s - \hat{x}_i}{\sqrt{2}} = \gamma'\hat{X}_-$.

4.4.3 Experimental Results

Figure 4.12a displays squeezing obtained in the experiment. We obtained 2.9 dB of squeezing with 5.4 dB of anti-squeezing corresponding to an efficiency of $\eta_{sq} = 0.61$. Here, the 800 mW pump was tuned 800 MHz blue of the $F = 1 \rightarrow F'$ transition, and the

[11] This parameter space included formed by pump power, pump detuning, two photon detuning, cell temperature, angle with respect to pump, and beam diameter.

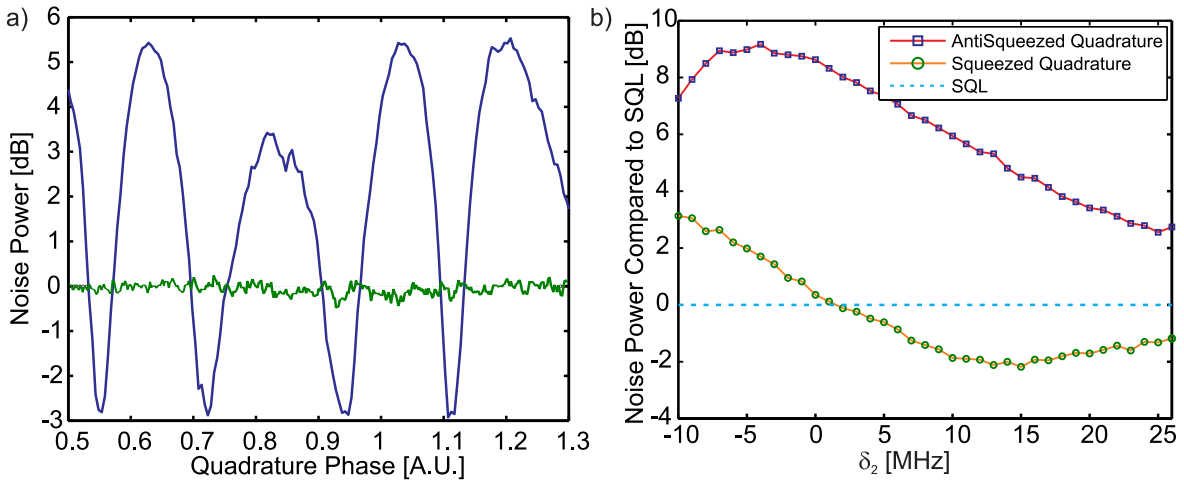

Figure 4.12: The squeezing produced experimentally. (a) We obtained up to -2.9 dB of squeezing corresponding to an efficiency of 0.61. The data here were taken with $\delta = 12$ MHz, $\Delta \approx 800$ MHz, and $P_{pump} = 850$ mW(b) The amount of squeezing obtained depended strongly on the two photon detuning

local oscillators were generated using a 200 mW pump, derived from the same beam. In order to observe significant squeezing, we needed to devote most of the available pump power to the squeezed vacuum signal, leaving only as much pump as necessary to produce the local oscillators.

We found that as for relative intensity squeezing, the most crucial parameter for efficiency in our setup was the two photon detuning δ_2 of the local oscillator with respect to the pump. This is most likely due to the asymmetry in the pump-induced signal beam absorption shown in figure 4.3 and mentioned in the analysis of relative intensity squeezing. An asymmetric loss quickly overwhelmed the squeezing and brought even the squeezed quadrature above the SQL. We explored this by measuring the envelope formed by the maximum and minimum quadrature noise as a function of two photon detuning as summarized in figure 4.12b. The optimal squeezing occurred for δ_2 between 10 and 15 MHz, and for negative detunings, the noise was so great that no squeezing was present at all. We can quantify the thermal noise added to the system by taking the geometric

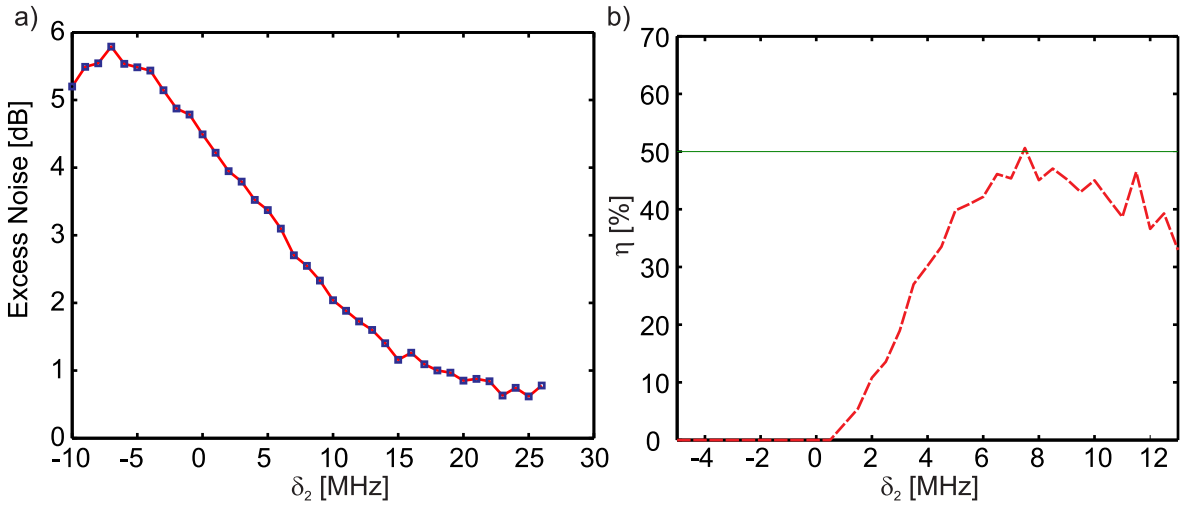

Figure 4.13: (a) By modelling the produced state as a statistical mixture of thermal and squeezed states, the excess noise on the system is plotted. (b) The Efficiency from equation (4.26) is plotted for the corresponding data.

mean of the values in figure 4.12b.Figure 4.13a shows this figure, the behaviour of which closely resembles the pump induced absorption in figure 4.3. From this we can conclude that a major source of the δ_2-dependent degradation in squeezing is the asymmetric Raman absorption profile. The corresponding efficiency of the process as a function of two-photon detuning is displayed in 4.13b. Note that the efficiency for the analysis performed on this set of measurements is less than displayed in figure 4.12a. This is because later alignment and improvements of the experiment yielded a higher degree of squeezing some time after the δ_2-dependence data were taken.

A key figure of merit of the source of squeezed light is the range of frequencies over which the state can be generated. This is important since atom based applications of squeezed light require specific frequencies which may vary from experiment to experiment. The frequency of the output state is tuned directly by the one-photon detuning Δ of the pump from the excited state (see figure 4.1). Figure 4.14a shows the squeezed and anti-squeezed quadrature noise for a one GHz scan of the one-photon detuning from 400 MHz

to 1400 MHz blue of the $F = 1 \rightarrow F'$ transition. From about 650 MHz to 1100 MHz the squeezing is roughly constant. The wide range of tuneability in this setup stems from its off resonant nature. For larger detunings, the squeezing decreases as a result of the decrease in $\chi^{(3)}$ which falls off with Δ. For smaller detunings, the process becomes dominated by additional effects such as pump scattering and losses from the Doppler broadened resonance begin to dominate. The optimal one-photon detuning is thus a compromise between maximizing the nonlinearity and minimizing the loss.

The dependence of temperature on squeezing was also explored. Since the squeezing is related to the gain via equation (4.25) with $\zeta = \cosh^{-1}\left(\sqrt{G}\right)$, the squeezing is expected to scale in the same manner as the gain, which increased up to around 150°C. Figure 4.14b displays the squeezing obtained as a function of temperature. The resultant efficiency is included as the deviation from $\eta_{sq} = 0.5$ for each temperature. Although the magnitude of quadrature squeezing increased with temperature as expected, the anti-squeezed quadrature increased such that the efficiency remained approximately constant for all temperatures. Since the Doppler width scales as $\sqrt{T}$, the inhomogenous broadened line width did not increase dramatically over this range of temperatures. On the contrary, the number density more than doubled over this temperature range and so this sharp dependence on temperature is most likely number-density dependent. From figure 4.4 the gain should increase by approximately a factor of 4 over this range and thus we expect a significant increase in squeezing. However additional noise-adding nonlinear processes increase concordantly with number density and introduce excess noise which reduces the effective efficiency of the squeezed source.

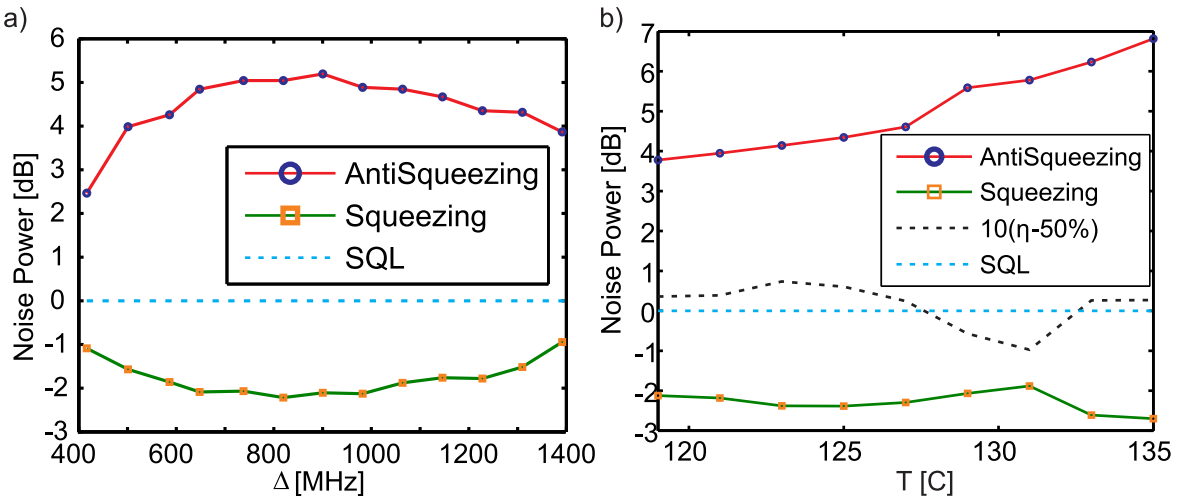

Figure 4.14: (a) The tuneability of the absolute frequency of the squeezing process is plotted by adjusting the one-photon detuning. (b) The effect of temperature on the absolute squeezing, and the efficiency of the resultant state. The black, dotted line shows the deviation of η_{sq} from 0.5, scaled by a factor of 10. The dip in the datum around 131°C was the result of accidental misalignment which was not noticed at the time of the experiment.

Chapter 5

An Atomic Source of Narrowband Single Photons

The historical workhorse of single photon generation is spontaneous parametric down conversion (SPDC) [16]. SPDC photon sources exploit the fact that ideally, photons are always emitted in pairs, into distinct channels. The measurement of a single photon in one channel collapses the state of the other channel to a single photon Fock state. One of the drawbacks of the conventional SPDC approach is that even if the emission wavelength matches that of an electronic transition, the phase-matching bandwidth is much wider than a typical atomic line-width. As a result, even SPDC sources which operate at the desired central wavelength produce photons which have a low probability of atomic interaction owing to spectral mismatch[1]. A natural solution to this problem is to use atoms to generate the quantum state of light rather than a bulk crystal, so that the light then naturally has the correct spectral characteristics to be efficiently mapped into another atomic system.

Our atomic photon source operates on the principle that in the unseeded case, the 4WM system produces a two-mode squeezed vacuum state described in the Fock basis by equation (2.26). A photon in the idler channel then implies the existence of a photon in the signal channel as in SPDC. Defining $G \equiv \cosh^2 \zeta$ as in the previous chapter, we see that the signal channel obeys thermal statistics when the idler channel is traced out:

$$\hat{\rho}_s = \frac{1}{G} \sum_{n=0}^{\infty} \left(\frac{G-1}{G} \right)^n |n\rangle\langle n| . \tag{5.1}$$

An important drawback lies in the fact that conditioned upon one *and only one*

[1]Quantitatively, the typical atomic transition has a line width $\Delta\nu \approx 10^1$ MHz whereas a typical SPDC process has $\Delta\nu \approx 10^7$ MHz.

photon in the idler channel the signal is the single photon Fock state $|1\rangle$. However, the single photon counters employed in our experiment, and indeed in nearly all experiments, do not resolve the number of photons present, but rather the presence of *at least* one photon. The state conditioned on a detection event is thus not truly a pure Fock state, but rather an approximation whose fidelity depends on the squeezing parameter. The renormalized state in the case of at least one photon becomes:

$$\hat{\rho}_s^{cnd} = \frac{1}{G-1} \sum_{n=1}^{\infty} \left(\frac{G-1}{G} \right)^n |n\rangle\langle n| . \tag{5.2}$$

The fidelity of the conditioned state is then:

$$f_{|1\rangle} = \langle 1| \hat{\rho}_s^{cnd} |1\rangle = \frac{1}{G}. \tag{5.3}$$

For optimal fidelity, the gain must be kept low. However, from equation (4.20) the mean photon number in the signal channel is given by $G-1$, and so the experimental count rate decreases with gain. Since photon counting modules exhibit false counts which introduce vacuum and thus lower the fidelity, the gain must be sufficiently high that the true counts greatly outnumber the dark counts. The optimal fidelity is given by the gain that balances the trade-off between maximal single-to-multiple photon events and true-to-false detector counts.

Using the analysis of the previous chapter, we were able to configure the system to produce high quality single photon states. **The basic experimental procedure was as follows:**

1. Operating in the low-gain unseeded regime, the signal channel was mixed with the local oscillator and continuously monitored at the homodyne detector, resulting in a background thermal state.

2. The idler channel registered a photon event, heralding a signal photon at the homodyne detector. This triggered an acquisition card to record the photocurrent for a temporal window about the photon event. This trace corresponded to a single, unprocessed quadrature datum.

3. After collecting a large number of quadrature data, each trace was integrated along the temporal mode of the photon creating a single quadrature point as per equation (3.2). This formed the marginal quadrature distribution.

4. A maximum likelihood estimation of the density matrix corresponding to the marginal distribution was made, as described in section 3.2.1.

5. (Optional) The Wigner function corresponding to the density matrix was computed using equation (2.32).

In order to ensure that the trigger event corresponded to an idler photon and not a pump, background, or signal photon, the trigger channel required significant filtering. This is addressed in section 5.2. An additional challenge arose in that we did not know the temporal wave function $\psi(t)$ of the heralded photon in advance. Without $\psi(t)$, we could not reconstruct the quadratures in step 2 above as described in section 3.1.3. We developed several methods to address this challenge which are described in section 5.3.

5.1 Experimental Design

The full experiment layout is shown in figure 5.1. The pump laser was derived from the Ti:Sa and could be seeded as in the relative intensity squeezing experiment for the purpose of alignment. The system was operated at low gain as per equation (5.3), with cell temperature of 97 °C corresponding to a gain of about 1.1. All of the alignment was performed with a weak seed to provide a measurable signal at each mirror, and the

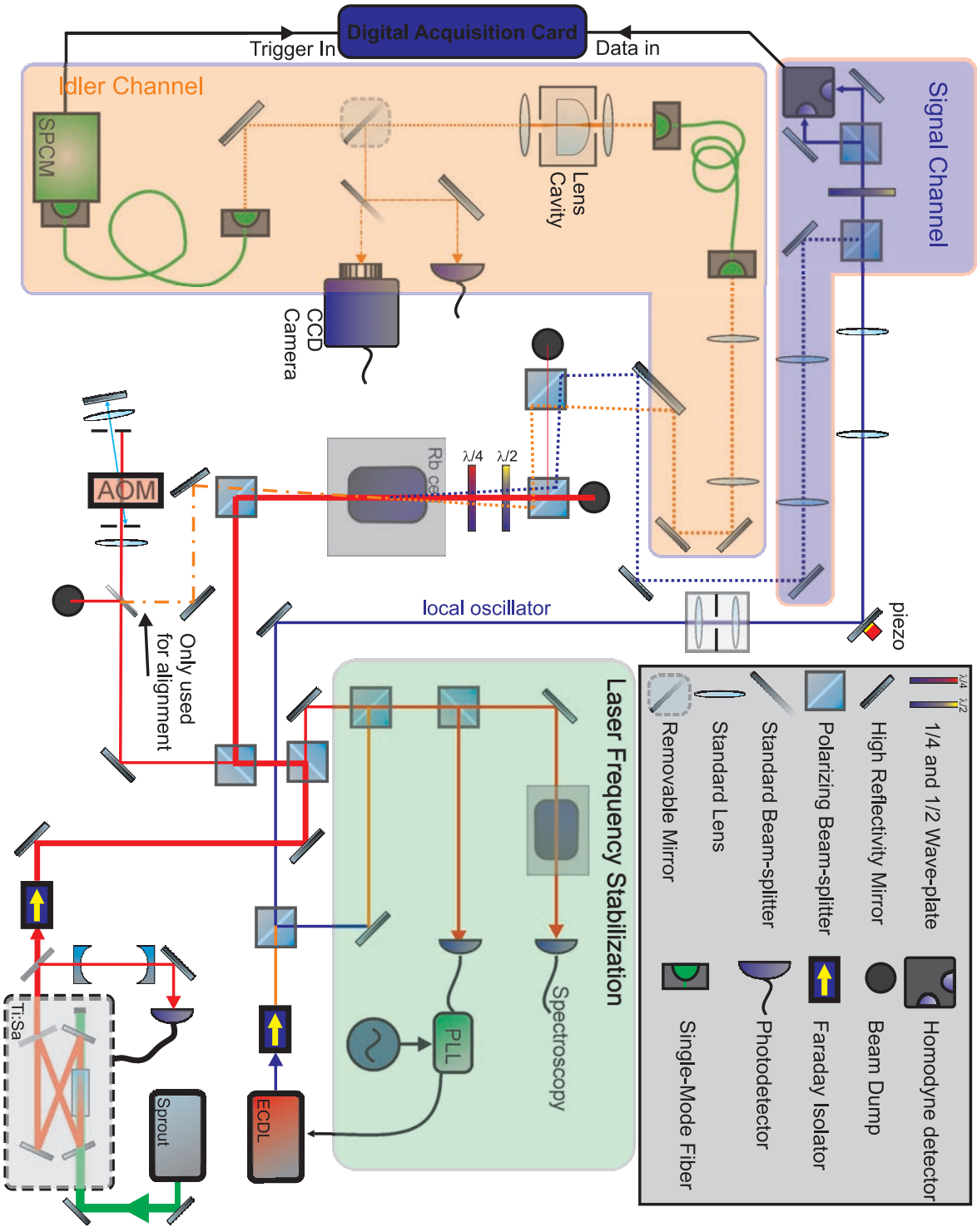

Figure 5.1: Full setup for the generation of narrowband single photons.

seed was blocked during the experimental runs. The signal channel was continuously monitored on a homodyne detector while the output was sent to an Agilent *Acquiris* DP 214 digital acquisition card. The idler channel was subject to a high degree of spectral and spatial filtering (see next section) and sent to a single photon counting module (SPCM). Upon receiving a photon event, the SPCM triggered the acquisition hardware to save all homodyne current within a temporal window of 180 ns for later analysis.

We initially faced the challenge of producing a phase-stable local oscillator for detecting the quadrature of the signal field. We could not seed the process as in the case of quadrature squeezing since we were operating at low gain and the resultant intensity was very weak (on the order of 10 μW), whereas the noise equivalent power of the homodyne detector was on the order of 1 mW. To bypass this problem we phase locked a separate external cavity diode cavity laser (Toptica DL 100) to the Ti:Sa at a frequency separation equal to the hyperfine ground state splitting of ^{85}Rb, thus matching the generated signal field. The self-built optical PLL [82] which was used for an earlier experiment on double-lambda systems [15] allowed up to 20 mW of local oscillator power, with residual phase noise with respect to the pump of less than 10 Hz. A small fraction of this beam was tapped off and sent through an auxiliary Rb cell for purposes of spectroscopy. A weak portion of the pump was also tapped off and mixed with the spectroscopy beam. The resultant beat frequency between the spectroscopy laser and the pump beam allowed us to monitor and set the one photon pump detuning with respect to ^{85}Rb atoms.

To compensate for the slight birefringence in the glass of the atomic vapour cell as well as Faraday polarization rotation from the atoms, a quarter-wave and a half-wave plate were placed at the exit of the cell. The pump was then attenuated by two successive polarizing beam-splitters. The signal and idler channels were allowed to propagate for some distance to allow for spatial filtration of the pump, as discussed in detail in the next section.

Since the 4WM process was spatially multimode [32], the mode selection was non-trivial. The idler channel was sent to a single mode fiber, subjected to spectral filtering, and then to a SPCM-AQR-14 Perkin Elmer single photon counting module (SPCM). Upon detection of a single photon at the SPCM, the signal channel collapsed to well-defined spatio-temporal mode as described by the Klyshko advanced wave model [85, 86]. According to this model, the heralded mode of the signal photon is that of the spatial filter of the idler, namely a single mode fiber which closely approximates a TEM_{00} Hermite-Gaussian mode [87]. Instead of applying spatial filtration directly to the signal channel which would have introduce a loss, we spatially filtered the *local oscillator* which selected an approximate TEM_{00} spatial mode without imposing any loss on the signal. Telescopes in each channel matched the waist and origin of each of the Gaussian modes.

5.2 Filtering out the Pump Field: Monolithic Filter Cavity

Imagine a grain of red sand dispersed throughout pile of black sand the size of a large mountain which is pouring into a container from above over the course of a second. Now imagine we must devise an apparatus which lets only the red grain of sand into a container and rejects all of the others. This was the order of magnitude of filtering required in the experiment to separate the idler photons from the pump beam. Each pump photon which made it through the filters to the SPCM caused a "false trigger" event. Consequentially, the detected state was then the background thermal state instead of the desired $|1\rangle$, lowering the fidelity of the reconstructed data. Clearly we needed far fewer pump photons than idler photons in the trigger channel. Since the mean photon number of the pump beam was on the order of $\langle n \rangle = 10^{16}$, whereas the signal beam had $\langle n \rangle \approx 0.1$ a suppression of over 170 dB was required for a SNR of at least 10:1.

5.2.1 Polarization and Spatial Filtering

Using the fact that the pump photons were orthogonal to the signal and idler, we obtained 50 dB of suppression with two successive polarizing beam splitters. Additionally, the signal and idler beams were at a small angle with respect to the pump, we allowed approximately 1.5 meters of free space propagation to spatially separate signal, idler and pump photons. One might ask why we did not allow much longer free space propagation to obtain arbitrarily large spatial separation. The reason is three-fold: First, the degrading effects of air fluctuations and mechanical motion of mirrors become more pronounced with propagation distance. Second, some pump light is scattered directly into the mode the idler mode and beam propagation, no matter how far, will not filter out this light. Finally, after a propagation distance of several Rayleigh lengths, i.e. the far field, the beam divergence and spatial separation each increase linearly and further propagation will not decrease the mode overlap which reaches an asymptote.

The measure of spatial filtering obtained by propagation was a competition between beam divergence and separation of the beam centres. Since $\theta \ll 1$, the beam separation Δx after a distance z from the atoms was $\Delta x \approx z\theta$. On the other hand the beam width for $z \gg z_R$ (see appendix C, was $w(z) \approx \frac{\lambda}{\pi w_0} z$. The separation between the pump and idler beams was then

$$\Delta x_{p,i} = (\theta - \frac{\lambda}{\pi} \frac{w_{0,p} + w_{0,i}}{w_{0,p} w_{0,i}}) z. \tag{5.4}$$

The first term is the angular separation and the second term represents the beam divergence. Clearly, for the fixed beam waist sizes in our experiment there was a minimum angle possible, below which divergence would cause the beams to overlap after propagation. For our parameters this corresponded to approximately 1 mrad. Figure 5.2 shows the attenuation of the pump beam for our beam parameters. From this our pump attenuation was expected to be at least 70 dB after isolating the idler mode by passing it

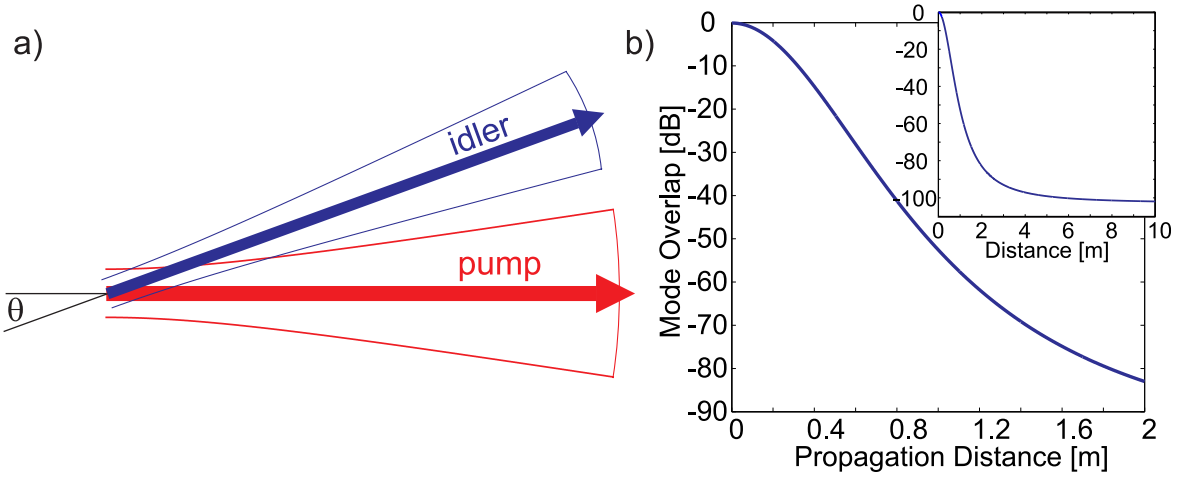

Figure 5.2: Spatial filtering in the setup: (a) shows the competition between beam divergence and spatial separation obtained by beam propagation. In (b) the overlap between the beams as a function of propagation is calculated for the experimental parameters: $w_{0p} = 550\mu$m, $w_{0i} = 400\mu$m, $\theta = 4.2$ mrad. The inset shows the far-field overlap which approaches an asymptotic limit.

through a single mode fiber, neglecting pump photons which were scattered into the fiber mode. We still needed over 50 dB of pump suppression to isolate single photons in the idler channel. To this end, we employed a novel design for a Fabry-Perot filter cavity.

5.2.2 Fabry Perot Filter Cavities

A high quality spectral filter can be made by placing two mirrors separated by distance l, with high reflectivity R (such that $1 - R \ll 1$) along the optical axis as diagrammed in figure 5.3. As light is incident upon the first mirror, a small portion of the field enters the resonator and propagates back and forth between the mirrors. Most light incident on the cavity is reflected, but for certain frequencies, the phase acquired through one complete passage meets the resonance condition:

$$\Delta\phi = kl = q\pi, \text{ with } q \in \mathcal{Z} \tag{5.5}$$

and the internal field constructively interferes with the incident light, quickly building up inside the cavity and allowing for perfect transmission. Since these resonances can be quite narrow, light of a given frequency can be isolated from a noisy background. To understand the transmission profile in more detail, consider a plane wave in the z-direction $E_{in}e^{ikz}$ incident on the cavity in figure 5.3: After the first mirror and traversing the cavity with an intensity loss of $1-\eta^2$, the field becomes $\eta t E_{in}e^{ikL}$, where t is the field transmission related to the intensity reflectivity as $t^2 = 1 - r^2 = 1 - R$. At this point the light could either escape the cavity with amplitude t or bounce back any number of times before exiting, picking up a factor $\eta^2 r^2 e^{2ikL}$ each time it does so. The total field at the output is the sum of each of the escaped field amplitudes:

$$E_{out} = \eta t^2 e^{ikl} \sum_{n=0}^{\infty} \left(\eta^2 R^2 e^{2ikl}\right)^n E_{in} = \frac{\eta t^2 e^{ikl}}{1 - \eta^2 r^2 e^{2ikl}} E_{in} \tag{5.6}$$

where we've identified the geometric series in the summation. The intensity transmission function is defined as $I_{out}/I_{in} = |E_{out}|^2 / |E_{in}|^2$. Using $\left|1 - xe^{i\theta}\right| = (1-x)^2 + 4x\sin^2\theta$ and noting that $kl = nl\omega/c$, n being the index of refraction of the intracavity medium, we arrive at:

$$T(\omega) = \frac{1}{\sigma^2 + F\sin^2\left(\frac{nl}{c}\omega\right)} \tag{5.7}$$

where $F = 4R/(1-R)^2$ is the coefficient of finesse and $\sigma^2 = (1-\eta^2 R)^2/\eta^2(1-R)^2$ quantifies the intracavity loss. Note that $\sigma^2 \geq 1$ with equality holding only for the case of no intracavity loss ($\eta^2 \to 1$).

Equation (5.7) illustrates a number of important features of Fabry-Perot filters. First, the transmission at resonance is σ^{-2} i.e. for a lossless cavity, perfect transmission is obtained, but the maximum obtainable transmission decreases with loss. For high reflectivity, this decrease in maximum transmission is sharp with loss, as shown in figure 5.4.

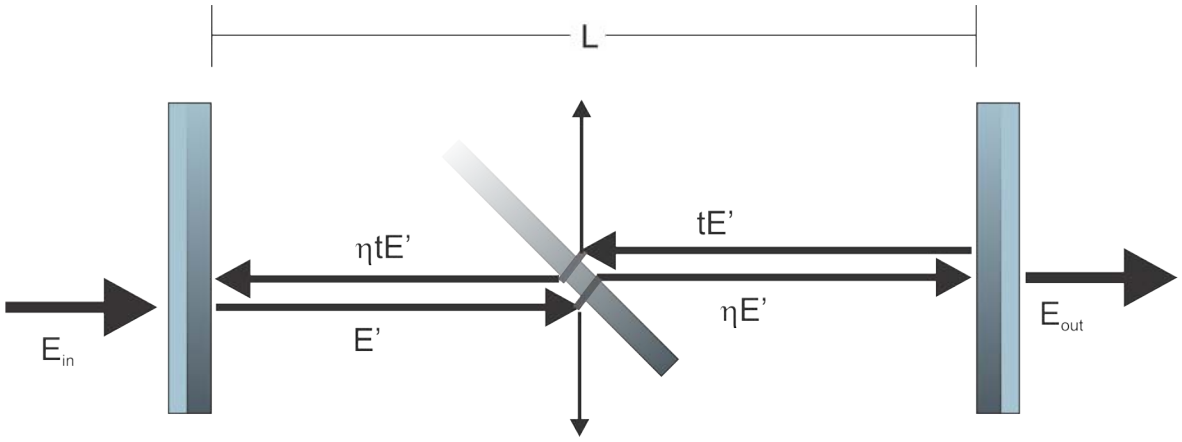

Figure 5.3: Illustration of the model for a simple Fabry-Perot Cavity. Loss in the cavity is modelled as a beam splitter with transmisivity η.

Second, the profile is periodic owing to the $\sin^2(nl\omega/c)$ term in the denominator. The period is known as the *free spectral range* (FSR):

$$FSR \equiv \frac{c}{2nL}. \tag{5.8}$$

Note that the FSR is solely a function of the cavity geometry. Transmission profile for $\eta = 1$ and 0.995 with $R = 0.97$ is shown in figure 5.4.

Near resonance the small angle approximation applies and the transmission profile approaches a Lorentzian with full width at half maximum[2] (FWHM), given by $\Delta\nu = \frac{2}{\pi}\sqrt{F} \times \text{FSR}$. This motivates the definition of the finesse as the ratio between the peak separation and the line width:

$$\mathcal{F} \equiv \frac{FSR}{\Delta\nu}. \tag{5.9}$$

In terms of the loss parameter and the coefficient of finesse, $\mathcal{F} = \frac{2\sqrt{F}}{\pi\sigma}$, so losses degrade the finesse and decrease the "sharpness" of the cavity profile.

[2]For small x, $\sin^2 x \approx x^2$ so $\left(1 + F\sin^2(nl\omega/c)\right)^{-1}$ becomes $\left(1 + (\sqrt{F}\frac{nl}{c})^2\omega^2\right)^{-1}$, a Lorenztian with FWHM $\Delta\omega = 2\pi\Delta\nu = 4\sqrt{F}\frac{c}{2nl} = 4\sqrt{F} \times FSR$.

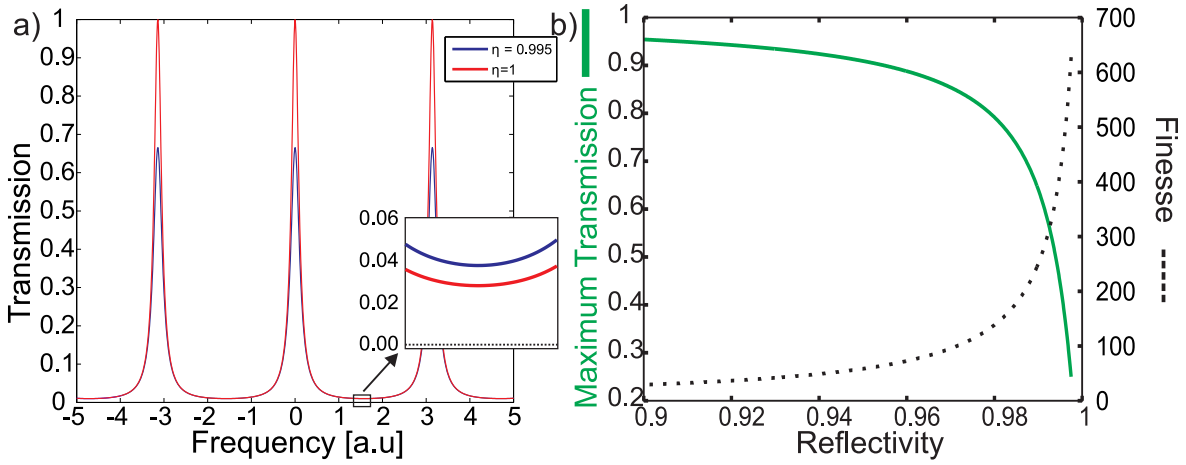

Figure 5.4: (a) Transmission spectrum spectrum for a Fabry-Perot Cavity over several FSRs with (blue) and without (red) loss. The reflectivity was set to $R = .97$ and the loss was $1 - \eta^2 = 0.005$. The lower inset displays the transmission minimum for the *normalized* transmission spectra, showing the degrading effect of loss on the filter (b) The maximum transmission (solid green) and corresponding finesse $\mathcal{F}$ (dotted black) as a function of mirror reflectivity R for a cavity with a round trip loss of 0.005.

A final important note regarding equation (5.7) is that the transmission minimum ideally scales as $\mathcal{F}^{-2}$ so a high finesse is a crucial parameter for the quality of a filter. However, since both finesse and peak transmission scale sharply as $R \to 1$, there is a fundamental trade-off between peak transmission and unwanted mode rejection as diagrammed in figure 5.4. Higher quality filters thus require low optical losses since we require $1 - L \leq R$ for high transmission.

5.2.3 Spherical Fabry-Perot Cavities

The assumption of an incident plane wave in the preceding analysis ensured that wavefront of the internal cavity field matched the mirrors at all points. This idealization can not be met in reality for two reasons. First, imperfections in the cavity surface cause wavefront mismatch and lower the effective fidelity. More fundamentally, plane waves are an idealization: real beams diverge while propagating (see Appendix C), and after

several round trips the mismatch between incident and propagating light destroys the constructive interference causing resonance. For this reason, planar Fabry-Perot cavities are limited to a finesse of about 100.

In order to circumvent this problem, concave mirrors can be used in place of flat mirrors to form a spherical Fabry-Perot cavity. The resonant modes of such a cavity are to close approximation the Hermite-Gauss modes of order (m, n) denoted TEM_{mn} [88]. The resonance condition (5.5) is still valid but for Gaussian modes propagating through a focus, an additional phase is acquired as compared to a plane wave, known as the Gouy Phase. The Gouy phase of a TEM_{mn} mode is

$$\phi_G = (1 + m + n) \tan^{-1} \frac{z}{z_R}. \tag{5.10}$$

Taking the Gouy phase shift into account, the condition for resonance of a TEM_{mn} mode in a spherical Fabry-Perot cavity of length L with radii of curvature r_1 and r_2 becomes [89]

$$\nu_{qmn} = \frac{c}{2L} \left[q + \frac{1 + m + n}{\pi} \arccos \sqrt{(1 - \frac{L}{r_1})(1 - \frac{L}{r_2})} \right], \text{ where } q, m, n \in \mathcal{Z} \tag{5.11}$$

The first term represents the plane wave resonance condition and the second term is the Gaussian beam correction.

While the refocusing effect of the spherical Fabry-Perot mirrors corrects for the beam divergence, the focus can be made too tight such that no Gaussian beam exists for which the radii of curvature at the cavity boundaries match the mirror surfaces. At this point, the resonator is said to be unstable. The condition for cavity stability was studied in [88] in which the cavity was modelled as a series of lenses separated by distance $nL \equiv L'$. In this case, the resonant field is the infinite product of ray-transfer matrices which may or may not diverge. The condition for convergence (and thus for cavity stability) can be

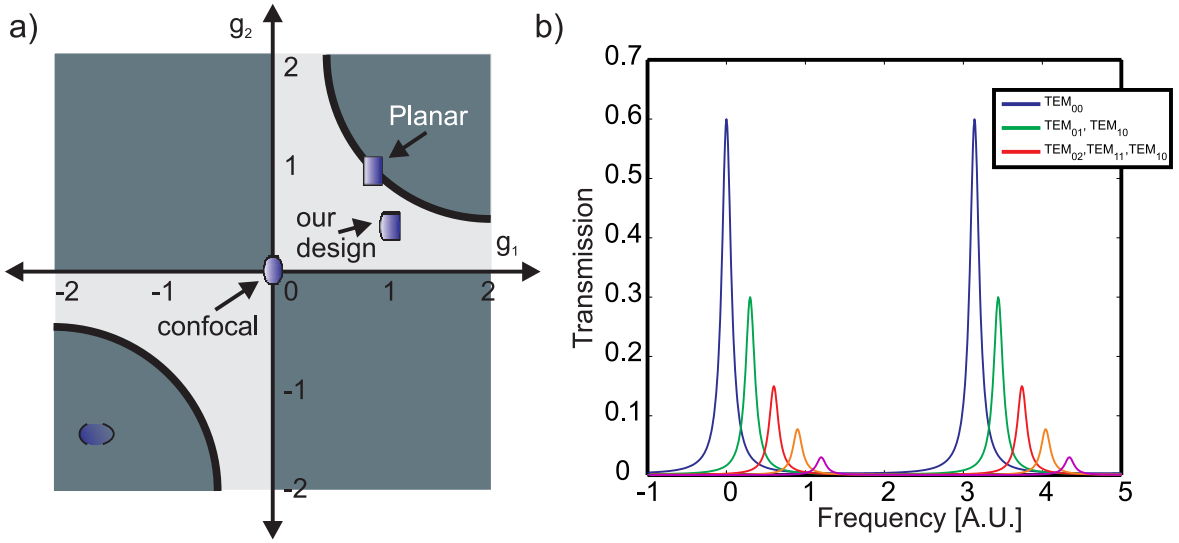

Figure 5.5: (a) Cavity Stability: the lighter region meets the condition (5.12) for resonator stability. Various configurations are displayed at their location on the stability plot. (b) A typical spectrum of a spherical Fabry-Perot cavity with an input that is not perfectly matched to the fundamental cavity mode. Such a spectrum displays the decomposition of the input mode into the basis defined by the cavity.

written as:

$$0 < \left(1 - \frac{L'}{R_1}\right)\left(1 - \frac{L'}{R_2}\right) < 1. \tag{5.12}$$

Defining the coordinates $g_{1(2)} \equiv (1 - nL/R_{1(2)})$, the region of cavity stability can then be visualized as in figure (5.5a).

The resonance condition (5.11) implies that separate transverse modes are resonant to different frequencies. The exceptions are flat mirror ($r \to \infty$) and confocal ($r = L$) cavities for which all transverse modes are degenerate. Confocal cavities are often used to ease the mode-matching process.

5.2.4 Our Design: A Monolithic Non-Confocal Fabry-Perot

Traditionally, filter cavities in quantum optics experiments have fallen into two categories: solid flat-surface Fabry-Perot cavities also known as etalons, and spherical Fabry-Perot cavities formed with separate mirrors. The solid design is highly stable and simple to construct but suffers from limited finesse. Several successive cavities are typically needed to obtain a high degree of filtering. In addition, tuning the resonant frequency is a challenge and is typically accomplished by thermal expansion or tilting the cavity at a small angle with respect to the beam. On the other hand, spherical Fabry-Perot cavities are capable of achieving high finesse and are easily tuned, but the separation between them must be actively stabilized. This is typically achieved by monitoring the transmission frequency of an auxiliary beam and providing feedback to maintain a constant transmission. However, residual phase noise from this process is never fully suppressed and is transferred to the transmitted light. In addition, the locking beam must then be filtered out so that it does not corrupt the signal. When the signal is a single photon, this is a considerable challenge.

Our approach was to employ a hybrid between the two existing paradigms, a monolithic spherical Fabry-Perot filter constructed by coating a standard lens substrate with high-reflectivity coating. This had the advantage of high degree of filtration after a single pass through the cavity while maintaining good transmission of the desired photon. The monolithic design provided long term stability without introducing any optical locking techniques. Operating in the non-confocal regime allowed for additional spatial filtering since pump light in a different spatial mode than the photons will not be matched to the cavity mode and photons which may escape the cavity at the pump frequency will not be in the same spatial mode as the idler photons.

Tuning was accomplished by utilizing thermal expansion of the substrate:

$$\frac{dL}{dT} = \alpha L \tag{5.13}$$

where α is the coefficient of thermal expansion of the substrate. The shift in frequency of the q$^{\text{th}}$ longitudinal mode with temperature can then be found as follows: the condition for resonance is[3] $\nu = q\frac{c}{2nL}$ so that[4]

$$\begin{aligned} \frac{d\nu}{dT} &= \frac{\partial\nu}{\partial L}\frac{dL}{dT} + \frac{\partial\nu}{\partial n}\frac{dn}{dT} \\ &= \frac{\partial}{\partial L}\left(\frac{qc}{2nL}\right)\alpha L + \frac{\partial}{\partial n}\left(\frac{qc}{2nL}\right)\frac{dn}{dT} \\ &= -\frac{qc}{2nL}\left(\alpha + \frac{1}{n}\frac{dn}{dT}\right) \\ &= -\kappa\nu \end{aligned} \tag{5.14}$$

where $\kappa \equiv \alpha + \frac{1}{n}\frac{\partial n}{\partial T}$ is the sum of the thermal expansion coefficient and the fractional change in index of refraction with temperature and is well known for optical materials [90].

Practically, a high value of κ meant easier tuning whereas a low κ meant a higher tolerance to temperature drift. Our design principle was to find the highest κ (and thus fastest tuneability) available such that the temperature fluctuations in our system corresponded to frequency shifts of less than a cavity line-width. Of the possible optical materials, BK7 had the highest κ with $\alpha = 7.4 \times 10^{-6}$ and $\frac{1}{n}\frac{dn}{dT}|_{\lambda=795nm} = 2.5 \times 10^{-6}$ [90]. Given this, $\frac{d\nu}{dT} = 3.7$ GHz/K. Since $\Delta\nu = 0.084$ GHz, we required a temperature stability of 0.023 °C, which was obtainable with current technology. We could then scan over a FSR by change in temperature of 6.24 °C.

We placed the cavity in a standard lens mount (Thorlabs HCS031) with a temperature transducer (Analog Devices AD590) physically inserted into the mount. The detector was

[3] . . . ignoring for now, the Gaussian beam correction since typically, $q \gg m, n$

[4] Actually, $n = n(\nu, T)$, but $\Delta\nu\frac{\partial n}{\partial\nu} \approx 9 \times 10^{-7}$, while $\Delta T\frac{\partial n}{\partial T} \approx 2 \times 10^{-5}$ over a FSR and so the variation of index of refraction with frequency may be safely neglected.

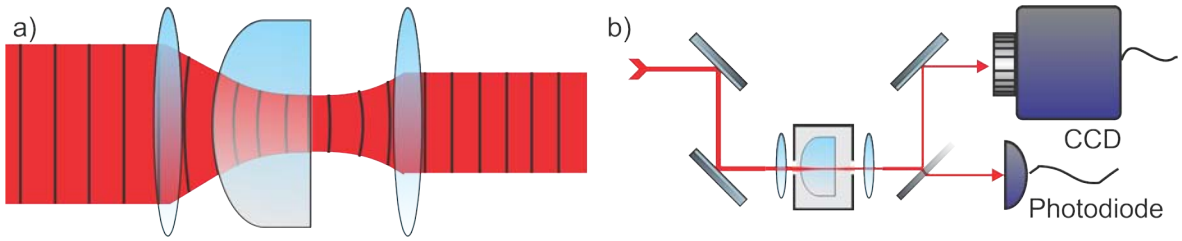

Figure 5.6: (a) Mode-matching to the cavity was achieved by matching the radii of curvature of the Gaussian beam to the cavity mirrors. (b) In order to aid the alignment procedure, the transverse mode structure could be monitored on a CCD camera simultaneously with the cavity intensity transmission on a photodiode.

thermally coupled to a Peltier element with a large aluminum block serving as a heat-sink. The Peltier element was controlled by a PID feedback-loop controller (Thorlabs ITC-110) which maintained a constant substrate temperature to 0.01 °C, which was within the desired tolerance.

The beam was matched to the fundamental mode of the cavity by matching the radius of curvature of the input Gaussian beam to that of the mirror surfaces. Since our cavity was formed from a plano-convex lens, the beam was focused at the planar side ($R(0) = R_1 = \infty$.) We then required the beam to have a radius of curvature at the other surface to be $R(nL) = R_2$. Using equation (C.5) this yielded the required beam waist of the fundamental cavity mode:

$$w_0 = \sqrt{\frac{\lambda nL}{\pi}\sqrt{\frac{R}{nL} - 1}}. \tag{5.15}$$

For our parameters of $R_2 = 40.68$ mm, $n_{BK7} = 1.51$ at $\lambda = 795$ nm, and $L = 5.3$ mm the fundamental mode was a Gaussian beam focused at the planar side of the cavity with waist $w_0 = 64.0\mu$m. Figure 5.6 shows the setup for matching the optical mode to the cavity.

5.2.5 Filter Cavity Performance

Since we needed to isolate the idler photons at frequency ω_i, from both pump and signal photons at frequency $\omega_p \approx \omega_i + 3.04$ GHz and $\omega_s \approx \omega_i + 6.08$ GHz respectively, we required a cavity with simultaneous rejection at these frequency differences from the resonance. To simplify this condition, we decided on a cavity for which each of these frequencies was within a single free spectral range. Based on the availability of lens substrates, we had six lenses coated by Lambda Research Optics, two each of center thickness $d = 4.3$ mm, $d = 5.3$ mm, and $d = 7.5$ mm corresponding to a FSR of 23.1 GHz, 18.7 GHz, and 13.2 GHz respectively. Each lens had a radius of curvature $R_2 = 40.68$ mm and was specified to a surface flatness of $\lambda/10$ at 633 nm. The reflectivity of each surface was $R = .990 \pm 0.0025$ at $\lambda = 795$ nm leading to an ideal finesse of $\mathcal{F} = 312$.

In order to investigate the performance of the filter cavities, we first focused a Gaussian beam with the desired waist at the flat side of the cavity (equation (5.15)), and simultaneously observed the output of the cavity on a photodetector and on a ccd camera as diagrammed in figure 5.6. The detector allowed us to observe the transmission spectrum and the camera displayed the transverse mode of a given transmission peak. The cavity alignment was then optimized by making iterative adjustments to the input focus and incident angle, maximizing the TEM_{00} transmission peak while minimizing all peaks corresponding to higher order modes. We achieved a maximum transmission of 60% while suppressing all higher modes by at least 30 dB.

Figure 5.7 displays a scan of the $d = 4.3$ mm cavity over a full FSR. The FSR was 23.1 ± 0.2 GHz which is consistent with the theoretical value of 23.09 GHz from eq. (5.8). We fit the transmission profile of the TEM_{00} mode to a Lorentzian and found $\Delta\nu = 83.85$ MHz[5]. The ratio of FSR to line-width gave us a cavity finesse of 275 MHz, less than the

[5]This was in actuality a convolution between the laser line-width and the cavity transmission but since the laser was narrowband with respect to the cavity transmission profile ($\Delta\nu_{laser} \approx 100$ kHz $\ll 83.85$ MHz), this contribution was negligible.

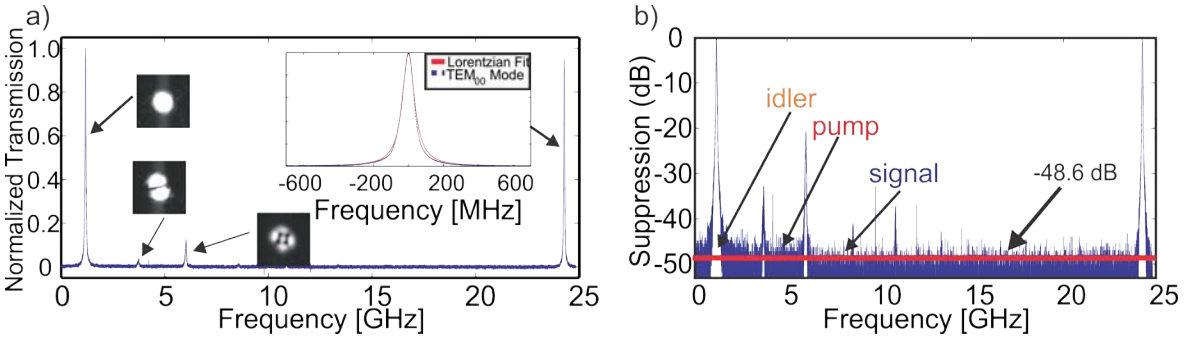

Figure 5.7: (a) The transmission profile of the $d = 4.3$ mm filter cavity over an entire FSR. The plot was normalized to a peak transmission of 55%. Transverse profiles of the first three peaks are shown as they appeared on the ccd camera and are identified as the TEM_{00}, TEM_{01} and TEM_{02} modes. The inset shows a Lorentzian fit to the fundamental peak. (b) The same plot, but on a logarithmic scale to illustrate the rejection of unwanted frequency modes. The spectral location of the idler, pump, and signal photons is displayed.

ideal value as result of loss, surface defects, and imperfect mode matching as discussed above. This imperfect mode-matching lead to several higher order transverse modes apparent in the spectrum, but aside from these narrow peaks, a high degree of isolation at separate frequencies was obtained. We also observed the spectrum on a logarithmic scale in order to quantify the frequency isolation with respect to the idler photons we wanted to isolate. The transmission for off-resonant frequencies was about 48 dB barring discrete higher order resonant frequencies. The transmission of both the pump and signal frequencies were constrained by this noise bound.

We investigated the temperature tuneability by observing the shift in a given resonance peak for varying temperatures, as shown in figure 5.8. The slope was seen to be linear with slope of 3046 MHz/°C. This differed from the theoretically predicted value of 3732 MHz/°C using coefficients from the literature. This discrepancy was most likely due to a combination of inaccuracy in the stated values BK7 (which varied by 20% depending on the source) and the temperature calibration of our sensor. However, our primary

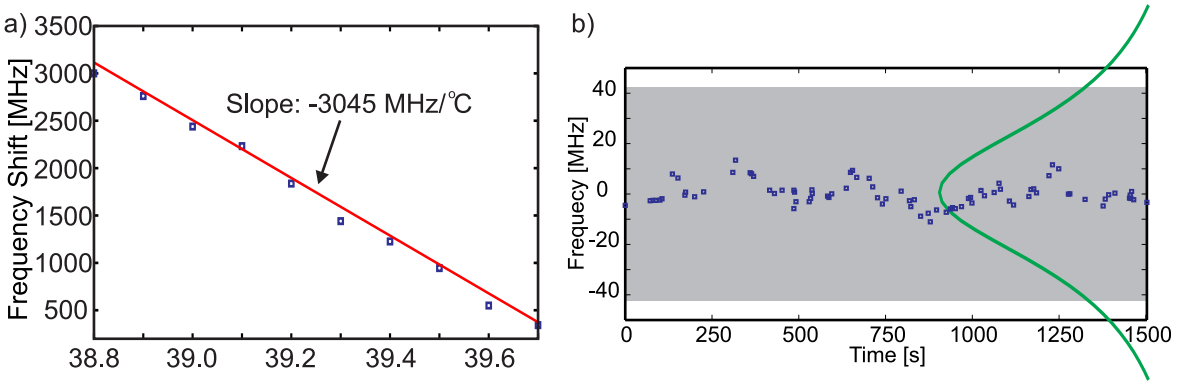

Figure 5.8: (a) The calibration curve for temperature tuning the cavity resonance. Blue dots show the frequency of the transmission peak at a given temperature. The red line is a linear fit with slope -3046 MHz/°C. (b) The long term frequency stability of our system. The transmission frequency (blue squares) was measured over a 25 minute span. The green curve shows the cavity transmission profile for scale, and the shaded area represents the cavity FWHM.

concern was the ability to tune a particular substrate to a given frequency which was possible from this calibration curve. In order to verify the long-term frequency stability of our filter cavities, we monitored the frequency difference of the transmission peak with respect to a separate laser which was stabilized to an atomic transition using saturated absorption spectroscopy. We observed a drift of $\pm 15.5\text{MHz} = 0.18\Delta\nu$ over a two hour span with a maximum drift velocity of $0.04\Delta\nu$/minute. Figure 5.8 displays a 15 minute interval of this measurement.

The slight birefringence in BK7 led to a splitting of transmission peaks for horizontal (s) and vertical (p) polarizations. Since we were using linearly polarized light, we simply aligned the polarization to the fast or slow axis of the substrate in order to maximize the transmission. If we were using circularly polarized photons a material with less birefringence would have been needed. The transmission for s, p and $(s+p)/\sqrt{2}$ polarizations is shown in figure 5.9. Incidentally, this plot served as an accurate measurement of the birefringence of the substrate: Since resonance implied $L = \frac{q_s c}{2n_s\nu_s} = \frac{q_p c}{2n_p\nu_p}$ for each polar-

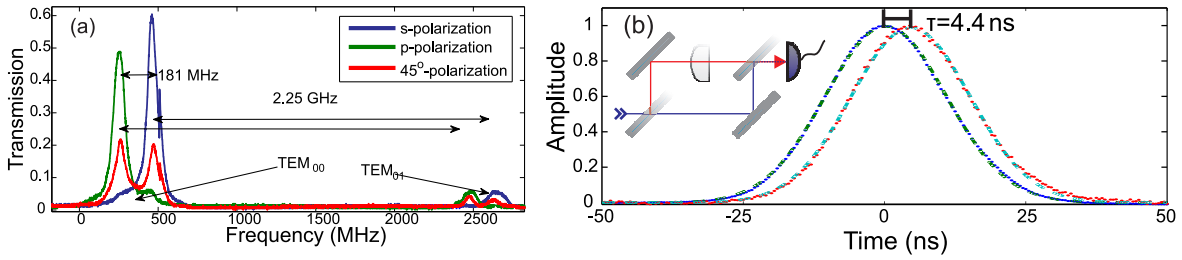

Figure 5.9: (a) The birefringence of the substrate led to separate peaks for s and p polarized light. (b) The slow light effect of the cavity's steep transmission profile gave important timing information for the single photon experiment.

ization, and noting that for small birefringence, the peak for each polarization is the same longitudinal mode number q, we have $n_p\nu_p = n_s\nu_s$ so that $\Delta\nu = \nu_s - \nu_p = \nu_s(1 - \frac{n_s}{n_p}\nu_s)$. The birefringence is thus:

$$\left(1 - \frac{n_s}{n_p}\right) = \frac{\Delta\nu}{\nu}. \tag{5.16}$$

For our substrate, this corresponded to 4.79×10^{-7}.

Since the idler photon passing through our cavity was used to trigger a temporal event, it was important to quantify the cavity-induced delay the photon experienced. To this end, we created a 40 ns pulse of light which was split and sent through equal path lengths, one containing the cavity and the other, free space. The delay, shown in figure 5.9 was found to be 4.4 ns, which corresponded to a free space delay of 1.32 m.

5.3 Inferring the Temporal Mode of the Photon

In order to reconstruct the quadrature value from homodyne detection, we required the temporal profile as in equation (3.2). In previous single photon systems, this mode is well defined from the characteristics of the system. For example, in the case of an optical parametric oscillator the temporal mode is approximately a double-decaying exponential

[20], and in the case of pulsed SPDC, the temporal mode is defined by the pump [19]. In contrast the 4WM source was in some sense uncharted waters The temporal mode was not known *a priori* and we needed to develop methods for inferring it.

5.3.1 Method of Point-Wise Variance

Fock states are noisy. From equation (2.10), the quadrature variance of a the state $|1\rangle$ is thrice that of $|0\rangle$. By monitoring the quadrature variance from the homodyne current as a function of delay from the trigger event, we found we could map out the magnitude of the temporal wave function of the photon $|\psi(t)|$. We did this by discretizing an interval of time surrounding the trigger event into N bins. After taking M samples, each corresponding to an individual trigger event, we computed the variance of each given bin individually. For a vacuum state, the variance should be constant within statistical fluctuations at all times, the value of which defines the standard quantum limit. Similarly, the randomly triggered signal mode should have no variation in variance with time, and the noise level above the standard quantum limit is given by the gain (equation (B.5)). In contrast, the trigger event in the idler channel defines a well defined temporal mode of a given duration, surrounding the event.

The temporal duration of the photon is roughly determined by its bandwidth via $\Delta t_{|1\rangle} \approx (\Delta\nu_{|1\rangle})^{-1}$. Since the width of the gain peak in the 4WM system was observed to be around $2\pi \times 10$ MHz, and since the photon bandwidth is determined by the width of this process, we predicted $\Delta t_{|1\rangle}$ to be around 16 ns. Both the SPCM and the acquisition card we chose had temporal resolution of 0.5 ns thus allowing us to temporally resolve $\psi(t)$ but the finite bandwidth of the detector ($\Delta\nu^{-1} \approx 10$ ns) smoothed out the profile and we observed the convolution of the detector's response function and $\psi(t)$.

We employed the following procedure for measuring the point wise variance: The acquisition card sampled the homodyne current for $N = 180$ bins of duration 500 ps

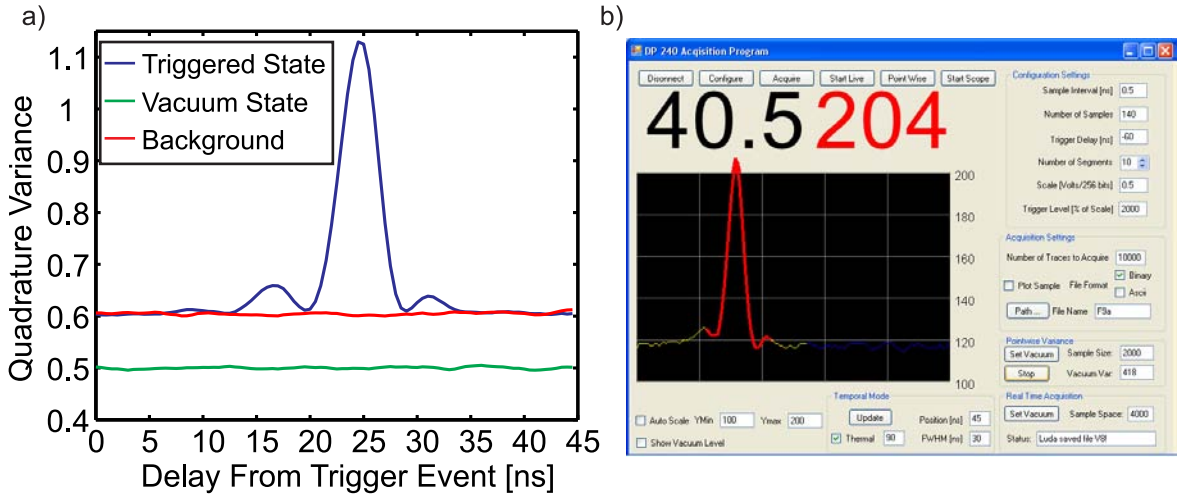

Figure 5.10: (a) Experimentally measured point-wise variance for the single photon experiment. The SQL was set by blocking the input to the homodyne detector. The background was obtained by randomly triggering the acquisition card. (b) We developed custom software to interface with the acquisition card, allowing us to monitor the variance real-time, while aligning the experiment.

around each trigger event and dumped this trace to memory. This was repeated for $M = 10^5$ samples for a given data run. Since the photon counting rate was around 250,000/second, this procedure took approximately 2 seconds. The variance of each bin over the duration over all traces was calculated and formed one point in the point-wise variance trace. Such a plot is shown in figure 5.10a.

In order to align the experiment to maximize the magnitude of the triggered feature, we developed custom software to provide continuous updates of the point-wise variance while aligning the experiment. This was crucial since subtle alignments made major differences in the obtained efficiency. From the point-wise variance, we could obtain an estimate of the fidelity of the retrieved state. Assuming that we have a statistical mixture of a pure Fock state and vacuum from losses: $\hat{\rho} = (1-\eta)\,|0\rangle\langle 0| + \eta\,|1\rangle\langle 1|$ the measured quadrature variance is then $\langle \Delta\hat{q}^2 \rangle = \frac{1-\eta}{2} + 3\frac{\eta}{2}$, whereas for the vacuum state it is just $\langle \Delta\hat{q}_0^2 \rangle = \frac{1}{2}$. If we measure the ratio of vacuum to triggered variance as r, the efficiency

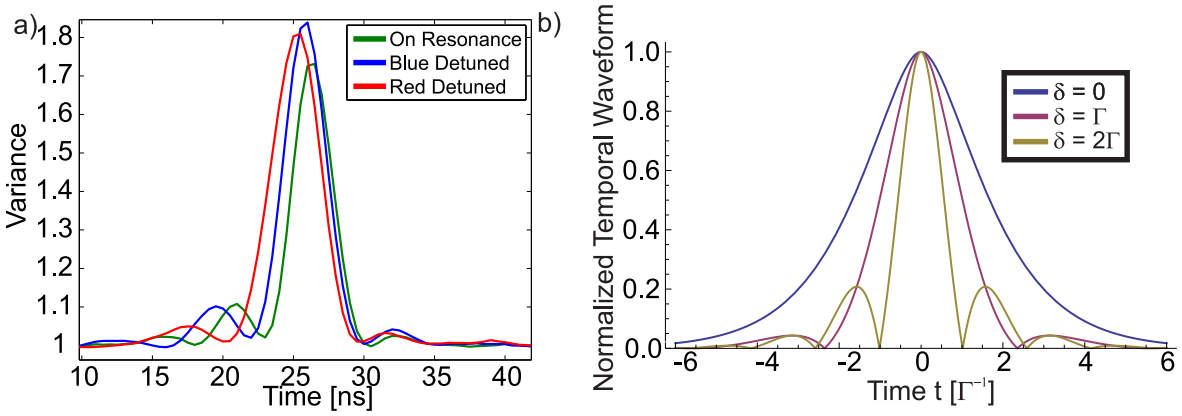

Figure 5.11: (a) The measured temporal profile of the photon for various cavity detunings. (b) The product of a Lorentzian photon spectrum with an off centre Lorentzian cavity profile leads to an oscillatory temporal profile.

is then:

$$\eta = \frac{r-1}{2}. \tag{5.17}$$

Experimentally the above assumptions are not met exactly: there is a finite probability of emitting more than one pair of photons and there is a thermal background present. Since the thermal background is uncorrelated to the trigger events, it adds in quadrature and may be subtracted out. Also, as long as the gain is close to 1, contribution from higher order pairs is small (5.3). This allowed an on-the-fly rough estimate of Fock state fidelity which is displayed on figure 5.10b.

The point-wise variance displayed oscillations with a period of roughly 8 ns. Furthermore, it was found that the temporal profile, the count rate, and the measured fidelity varied sharply with detuning of the idler photon from the resonant frequency of the filter cavity. Figure 5.11a displays the measured point wise variance for several small detunings with respect to the filter cavity. Note that the temporal profile of the photon is given by the Fourier transform of the spectral profile. Assuming a Lorentzian gain

peak, one would naively assume the temporal shape to be the Fourier transform of the Lorentzian, which is the double-decaying exponential $\exp(-\kappa\,|t|)$. However the spectral filtering of the lens-cavity yielded a spectral profile which was the product of the lens-cavity and photon spectra, and the product of two Lorentzian functions is not itself a Lorentzian. Figure 5.11b shows the expected temporal profile of a spectrally-Lorentzian photon passed through a Lorentzian filter of the same width for various relative detunings and oscillations in the temporal mode appear as in the point wise variance. This implies that especially in the case of the idler photon being slightly off cavity resonance, the signal photon's spectral profile is determined in part by the spectral filter.

We found that the magnitude of the point-wise variance along with the inferred efficiency varied dramatically with cavity detuning. For the signal beam blue detuned with respect to cavity resonance the peak variance was maximized and the temporal profile contained minor oscillations. On cavity resonance, the count rate was highest, reaching 10^6 counts/second, and the temporal profile was wider, but the peak variance was reduced compared to the blue detuned case. When red-detuned, the increase in variance due to the photon was barely noticeable above the constant background noise resulting in poor efficiency (not shown in figure 5.11). This behaviour can be understood in terms of our findings for the two-mode squeezing, particularly in figure 4.13. When red detuned, the 4WM process is overwhelmed by Raman absorption, resulting in scattering of uncorrelated photons into the trigger channel. Each of these scattering events results in a "false click" and the signal to noise ratio of the detected photons is reduced. By adjusting the cavity to transmit light which is blue detuned with respect to two-photon resonance, we maximized the probability that the detected photon was from the four-wave mixing process and thus heralded a photon in the signal channel.

From the variance of thermal background as compared to vacuum, we were able to estimate the mean photon number of the 4WM source. From equation (B.5), $\left\langle \Delta\hat{X}^2_{\text{thrm}} \right\rangle / \left\langle \Delta\hat{X}^2_{\text{vac}} \right\rangle \equiv$

$r_{\text{thrm}} = 2\bar{n} + 1$. Our data showed $r_{\text{thrm}} = 1.2$ implying that for our source, $\bar{n} = 0.1$.

5.3.2 Method of Auto-Correlation

An initial question we faced when first analyzing the experiment was whether or not the correlated photons were emitted in a well defined temporal wave-function. To gain insight, we addressed the problem in the following way: suppose we have a single photon which can be in one of infinitely many discrete time bins t_m with some probability ρ_{mm}. Denoting a single photon in the m^{th} bin as $\cdots |0\rangle_{m-1} |1\rangle_m |0\rangle_{m+1} \cdots \equiv |m\rangle$, we can write the density matrix in the orthonormal basis defined by these time-bins as

$$\hat{\rho} = \sum_{m,n} \rho_{mn} |m\rangle \langle n| . \tag{5.18}$$

If the state is fully mixed then the density matrix will contain only diagonal terms. On the other hand, if the photon's temporal wave-function is a pure state $|\psi(t)\rangle = \sum_n c_n |n\rangle$, then the density matrix will contain off-diagonal terms representing the coherence between the different moments in time. We thus sought a method to obtain the temporal density matrix[6]. To this end we discovered a relation between the autocorrelation matrix of the experimentally measured homodyne current and the density matrix. With the autocorrelation matrix $\hat{A}$ defined as

$$A_{ij} = \langle i(t_i) i(t_j) \rangle , \tag{5.19}$$

where the average is taken over all experimental realizations, we have (see Appendix E.2)

$$\hat{A} = \text{Re}\,[\hat{\rho}] + \frac{1}{2}\mathbb{1}. \tag{5.20}$$

[6]Note the distinction here between the usual density matrix in the Fock basis used everywhere else in the thesis and the temporal density matrix defined in this restricted Hilbert space, consisting of a single photon spread out in time.

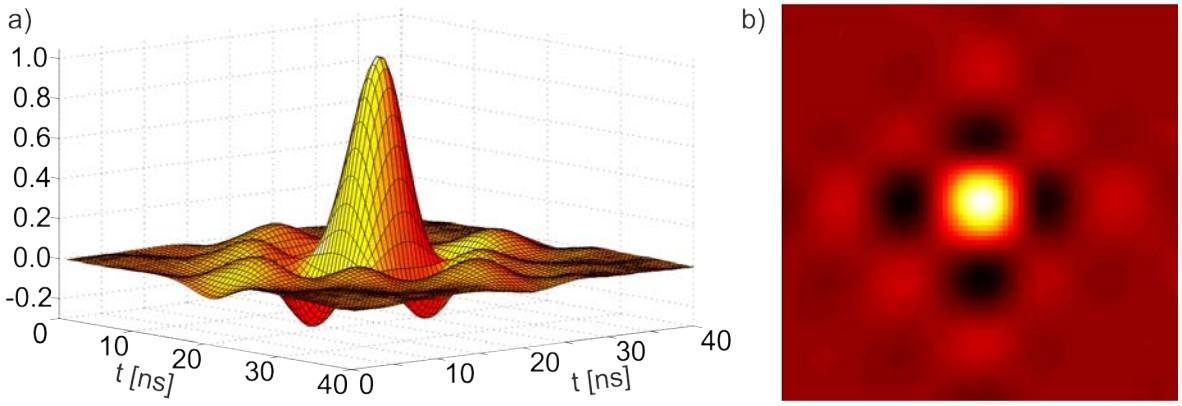

Figure 5.12: (a) The autocorrelation matrix reconstructed from an experimental run. Here the diagonal matrix of the background thermal state has been subtracted off. (b) Density plot of the auto correlation matrix. The high degree of symmetry about the $x-y$ axis implies a pure temporal mode.

Figure 5.12 displays the autocorrelation matrix of the photocurrent we measured in an experimental run. To isolate the photon from the thermal background and the detectors response function, we first calculated the autocorrelation of the (untriggered) background and subtracted it from that of the triggered photon state. This also removed the identity term from equation (5.20) leaving only $\mathrm{Re}[\hat{\rho}]$. From the top view, we found that the central feature of $\hat{A}$ was round in shape, and symmetric about x and y, implying that it could be written as the product of a vector $|\psi\rangle\langle\psi|$, i.e. a pure temporal state. We then diagonalized $\hat{A}$ and found that the matrix had a primary eigenvalue, roughly 50 times larger than any other eigenvalue. The eigenvector corresponding to this eigenvalue thus represents the temporal weighting function ψ. This vector, as well as the corresponding vector found using other approaches is displayed in figure 5.13b.

5.3.3 Method of Genetic Algorithm

Determining the correct temporal mode can be thought of as an optimization problem: given the space of all real weighting functions $\psi_i(t)$ find the particular function that max-

imizes the quality of the reconstructed state. This could mean maximizing the variance of the heralded quadrature distribution, or maximizing the single photon probability $\langle 1|\,\hat{\rho}\,|1\rangle$ of the resultant density matrix. Since the problem is not necessarily convex or linear, many optimization procedures may become stuck at a local maximum. An elegant approach to optimization under these circumstances is the use of a genetic algorithm [91].

Genetic algorithms borrow from the concept of Darwinian evolution [92]. The function to be optimized is parameterized in terms of a bit-sequence called a genome. The fitness of a given genome is evaluated by a fitness function f which returns a real number that increases based on how well suited the genome is to solving the problem. Initially, a population of random genomes is chosen and their fitness is evaluated. Parent genomes are then chosen in pairs which "mate" by producing offspring whose genomes are formed as combinations of the parents' genomes. The process works as a lottery in which the probability of being chosen as a mate increases with f. This "mating procedure" is repeated until a new generation is populated, and the procedure repeats. This is continued until a satisfactory solution is found, or until manual termination of the program. In order to avoid local maxima, random mutations in the genomes occur with some probability at the beginning of each generation.

For the problem of finding the optimal wave function, the genome encoding was chosen as the sum of n Gaussians, with standard deviation ranging from 1 to 2^m, height from $1-2^{s-1}$ to 2^{s-1} and position chosen from 2^t bins evenly spaced across the chosen temporal range of the photon, yielding a $n \times m \times s \times t$-bit genome. The fitness was chosen as a monotonically increasing (polynomial) function of either the variance, or the single photon component of a least-squares fit to a truncated density matrix. The least squares fit was performed by assuming a statistical mixture of photons (no off-diagonal elements) with maximum photon number 3. The marginal distribution of the resultant density matrix was then an analytic expression in 3 unknowns: $\Pr(x) = (1-\eta_1-\eta_2-$

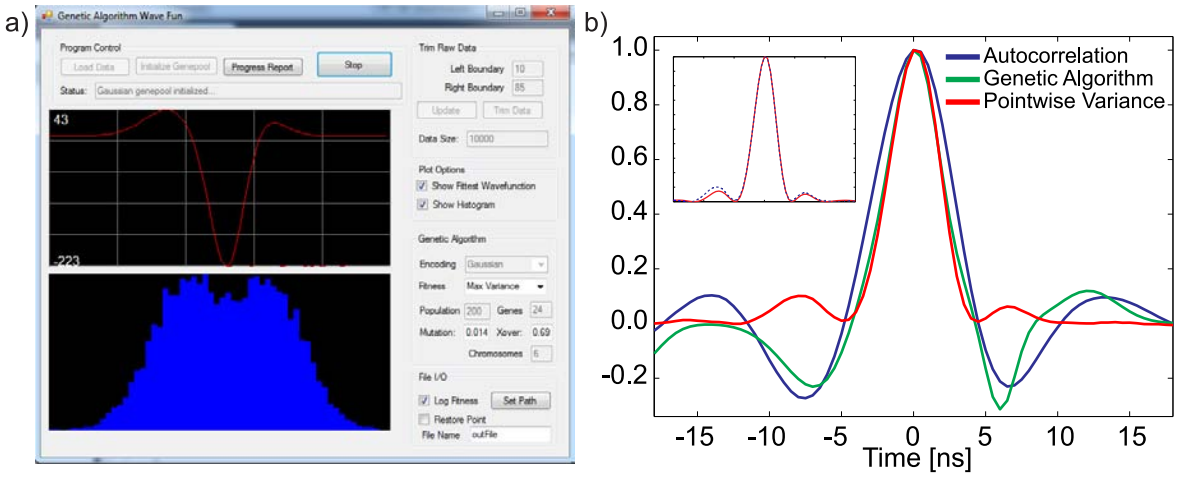

Figure 5.13: (a) The genetic algorithm program estimating the wave function of some experimental data. The upper panel displays the fittest genome and the lower panel shows the marginal quadrature distribution for this temporal mode of this genome. (b) Comparison of the different methods for inferring the temporal wave-function of the photon. Although the point-wise variance is positive-definite, the square of the auto-correlation function closely resembles the point-wise variance as seen in the inset.

$\eta_3)\,\mathrm{Pr}_0(x) + \eta_1\,\mathrm{Pr}_1(x) + \eta_2\,\mathrm{Pr}_2(x) + \eta_3\,\mathrm{Pr}_3(x)$ where $\mathrm{Pr}_n(x)$ is the Fock state marginal distribution. The least squares solution could be written directly and the fitness was then proportional to η_1.

The mating procedure used in the program was based on the "Roulette wheel" selection. Here a random number x between 0 and the total fitness of the population $F = \sum f_i$ is chosen. The fitness of each member of the population is then added until this sum exceeds x, at which point, the last member who's fitness was added is chosen for mating, and the next random number is chosen. This method has the property that even the fittest member of the generation may not be selected. To ensure at least one copy of the fittest gene survives, the principle of "elitism" is employed in which the fittest member is copied automatically to the next generation. Random mutations may then occur with some small probability to the remainder of the population and the process is repeated. Figure 5.13a shows the program in action.

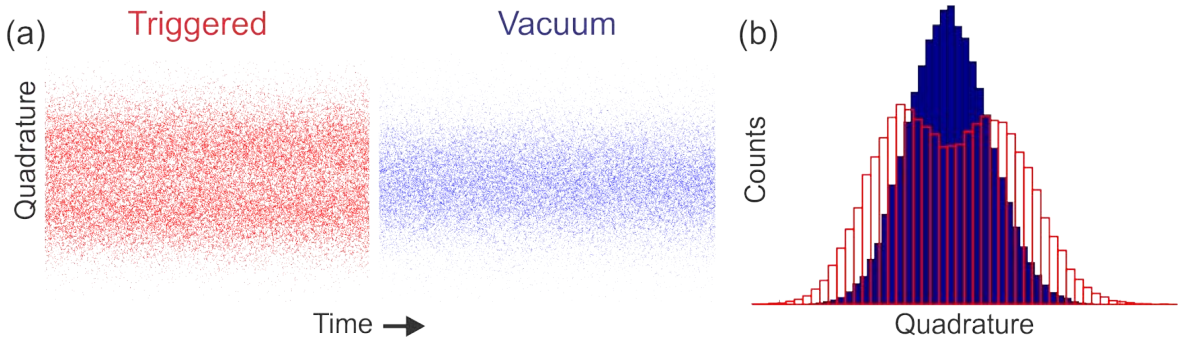

Figure 5.14: (a) Fock (red) and vacuum (blue) quadratures for a given data run. Each trace contains 10^5 points. (b) Marginal histograms for the data in (a).

We found that after a few hundred generations, the solution did not significantly change and that most of the time, a solution was found that closely resembled the temporal profiles inferred by point-wise variance and autocorrelation. On one hand this was good in that it con fired the consistency of the above approaches, but of course was less dramatic than a vastly different mode evolved genetically. We also noted that the profiles that maximized ρ_{11} were slightly different than those that maximized the variance. We attribute this to the fact that in the presence of the noisy thermal state, the maximal variance is obtained not only by including the photon, but also the noisy background at the periphery of $\psi(t)$. In contrast, the least squares method weights the background less since it contains 0 and 2 photon components which are included at the expense of ρ_{11}. Given the wave function found by one of several different methods, we could then proceed to produce the quadrature ensemble and reconstruct the full density matrix of the heralded state.

5.4 Experimental results

5.4.1 Tomographic Reconstruction of Heralded Photon

Given the temporal mode of the heralded photon, we could produce the set of measured quadratures using equation (3.2). We collected 10^5 quadrature samples to form the marginal quadrature distribution which was then analyzed using an iterative maximum likelihood program. Figure 5.14 shows the marginals for the Fock vacuum data. Note that the marginal distribution displayed a clear dip at the origin as expected for the single photon state. In the ideal case, the probability of measuring a quadrature value of zero vanishes, but this is not the case here owing to the mixture of vacuum due to loss and thermal state due to the background. The corresponding density matrix and Wigner function are displayed in figure 5.15. As expected for the single photon, the heralded state showed no quadrature phase dependence. We verified this by scanning the phase of the local oscillator and observing the resultant distribution. This simplified the experiment since small phase shifts due to mechanical vibrations did not affect the measured state.

The high uncorrected single photon fidelity obtained here is notable since it is roughly an order of magnitude higher than that of previous atomic sources. The diagonal density matrix elements were $(\rho_{00}, \rho_{11}, \rho_{22}, \rho_{33}) = (0.424, 0.488, 0.069, 0.019)$, with relative uncertainty given by the standard error of $1/\sqrt{N} = 3\%$ [93]. The relatively high two-photon fraction of 0.069 as compared to SPDC sources for which $\rho_{22} \approx 0.01$ depending on the source [94, 95], was most likely due to several effects. First, in order to obtain high efficiency, we needed to operate at a temperature corresponding to a gain of 1.1. From equation (5.1), the ratio of double to single photon probabilities was $1 - 1/G \approx 9\%$ here. Additionally, Raman scattering of pump photons off atoms flying into the beam contribute a thermal background. The portion of this background which is scattered

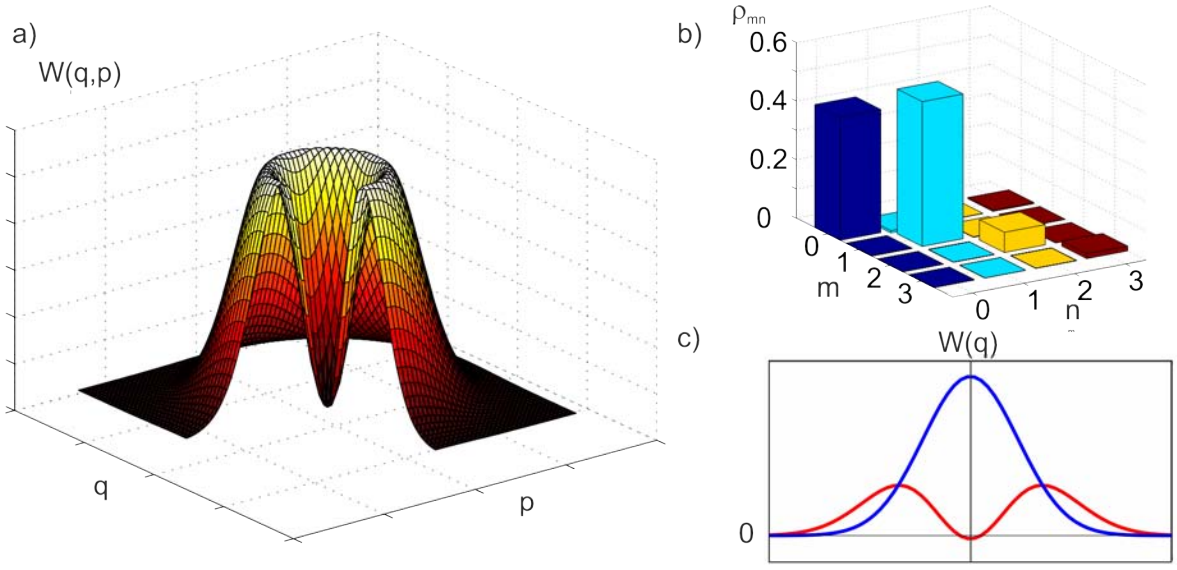

Figure 5.15: (a) The reconstructed Wigner function of the state produced in the experiment, showing the characteristic dip at the origin. (b) The density matrix recovered from the maximum likelihood procedure showing $\rho_{11} = 0.487$. (c) Cross-section of the recovered Wigner function displaying a negative value at the origin due to large single photon and minor three photon components.

into the mode of the signal photons will contribute to the two photon component of the reconstructed density matrix.

5.4.2 Performance of the Source in Terms of Standard Figures of Merit

In contrast to previous experiments on atomic based photon sources, our tomographic reconstruction of the density matrix gave full information of the quantum state emitted from the atoms. This allowed us to calculate common figures of merit for single photon sources defining the state as non-classical as in section 2.5. We found that in the uncorrected reconstructed temporal mode the second order correlation of the field was $g^{(2)}(0) \equiv \langle \hat{a}^\dagger \hat{a}^\dagger \hat{a} \hat{a} \rangle / \left(\hat{n} \right)^2 = 0.51 < 1$ and the Mandel Q-parameter is $Q = -0.32 < 0$ evidencing the nonclassical character of our photon source. The difference between the ideal value of $g^{(2)} = 0$ and our reported figure is primarily due to the higher-number terms resulting from the background thermal state. When we operated the process at much lower gain, corresponding to a temperature of 69°C, our two-photon component was negligible and was bounded above only by the statistical uncertainty of our measurement (0.3%). In this case the second order correlation was bounded above by $g^{(2)}(0) < 0.13$. However, the single photon fidelity was lower at this gain, reaching only 21%. This was most likely due to a poorer signal to background noise ratio as the count rate was significantly reduced at this temperature.

Another figure of merit for a heralded photon source is the conditional cross-correlation function which quantifies the probability that a photon in the trigger channel accompanies a photon at the homodyne detector, compared to the probability that the homodyne detector detects a photon without a trigger event. For continuously monitored homodyne current, this can be written in terms of the quadrature variance of the triggered data $\langle \Delta \hat{X}^2_{\text{trig}} \rangle$ and the thermal background $\langle \Delta \hat{X}^2_{\text{bck}} \rangle$ as [20]

$$g^{(2)}_{\mathrm{si}} = \frac{\langle \Delta \hat{X}^2_{\mathrm{trig}} \rangle - 1/2}{\langle \Delta \hat{X}^2_{\mathrm{bck}} \rangle - 1/2}. \tag{5.21}$$

At lower temperatures we find $g^{(2)}_{\mathrm{si}} = 24.2 > 1$ at zero delay whereas for higher temperatures we measure $g^{(2)}_{\mathrm{si}} = 6.0$.

A noteworthy aspect of our results is that the above values are not corrected for loss, and the system is taken as-is. Our uncorrected photon efficiency, known as the heralding efficiency is an order of magnitude higher than other atomic sources reported in the literature. One reason for this dramatic increase was that we used homodyne detectors which have quantum efficiency as high as 90% as opposed to the less than 50% efficiency of the SPCMs used in previous experiments. Correcting for a modest estimate of optical loss and imperfect detectors yields a lower bound on the photon efficiency: $\rho_{11} > 0.65$. We also worked off atomic resonance which minimized uncorrelated photon emission which typically cause false counts.

Table 5.1 summarizes the current state of the art for single photon sources using various technologies.

Table 5.1: Comparison of $g^{(2)}(0)$ for various single photon technologies

System	Reference	$g^{(2)}(0)$	Retrieval Efficiency
Cold Atomic Cloud	[96, 97]	0.25	0.2
Single Atom in Cavity	[98, 99]	0.06	0.05
Quantum Dot in Cavity	[100]	0.02	0.10
Waveguided SPDC	[101]	0.0007	0.07
Bulk SPDC	[102]	.60	0.0014
4WM in Photonic Crystal Fiber	[103]	0.01	0.18
This Work	[104]	0.5	0.49

5.4.3 Bandwidth and Spectral Brightness

Even with a wide-band source of photons such as standard SPDC, one can always place a narrow spectral filter in the trigger channel, resulting in photons in the signal channel

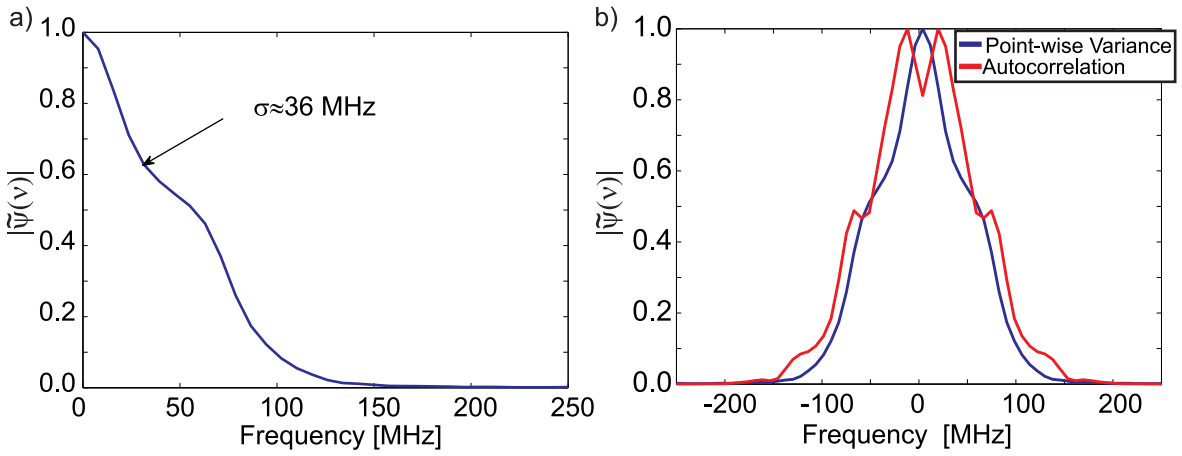

Figure 5.16: (a) The bandwidth of the photon is inferred from the Fourier transform of the temporal mode used to reconstruct the density matrix. The standard deviation of the mode is 36 MHz. (b) The spectral shape of the autocorrelation mode is more complicated, owing to modulation terms.

with a bandwidth of the spectral filter [85]. However this comes at a cost: the probability of a generating a photon per unit frequency is a property of the source, not the filter. As a result, the production of narrowband light comes with a greatly reduced production rate. This is quantified by the spectral brightness $S(\nu)$, giving the counts per second, per unit bandwidth. Given a source of spectral brightness $S(\nu)$, the bandwidth may be narrowed with a filter to $\Delta\nu_f$ yielding a production rate of $S(\nu)\Delta\nu_f$.

The bandwidth of a source may be obtained by observing the Fourier transform of the temporal mode [30]. Roughly speaking, a wave-form with temporal duration σ_t, will have a angular frequency spread of σ_t^{-1}. For a Gaussian waveform, this relation is exact and the temporal pulse is said to be transform limited. Figure 5.16a shows the bandwidth of the temporal mode used to reconstruct the quadrature data presented in figure 5.15. Note the waveform is not transform limited, so the frequency domain profile falls off more slowly than a Gaussian. The e^{-2} width was found to be 36 MHz. Given the count-rate of about 250,000 counts/second, this corresponded to $S(\nu) \approx 7000 \frac{\text{cts}/s}{MHz}$. The

Fourier transform of the autocorrelation of the point wise variance principle eigenvector is also shown in figure 5.16. Owing to the extra oscillations present in the time domain, the maximum is shifted from 0 frequency.

Table 5.2 displays a sample of photon sources with the highest spectral brightness to date, including our 4WM based source.

Table 5.2: Comparison of high spectral brightness sources

Group	System	Reference	$\Delta\nu$ [MHz]	λ_0 [nm]	$S(\nu) \times 10^3$ $\frac{\text{counts}}{\text{MHz s}}$
O. Benson	OPO	[105]	3	860	130
V. Vuletic	Cavity QED	[30]	1.1	795	45.4
J.-W. Pan	OPO	[21]	5	795	36
This Work	4WM in Rb	[104]	36	795	7.0
Michler	Q. Dot	[23]	1000	907	5.9
Gisin	SPDC	[106]	1200	1550	3.1
E. Polzik	OPO	[20]	8	860	1.5

Chapter 6

Engineering Arbitrary Superposition States of Light and Matter

In the last chapter we described our implementation of a narrowband source of a particular quantum state: the single photon Fock state $|1\rangle$. We could also consider creating more complex quantum states which are compatible with atomic ensembles. We can write any single mode state consisting of N photons in the Fock basis. The most general such state is:

$$|\psi\rangle = \sum_{n}^{N} c_n |n\rangle , \tag{6.1}$$

where ideally, $N \to \infty$.

In this chapter we will describe how we accomplished an arbitrary superposition of 0, 1, and 2 photons using a conventional SPDC source and how we did a similar experiment with our narrowband source. Creating the superposition state with an atomic ensemble opens up a new exciting possibility: the ability to engineer arbitrary superposition states of atomic excitations.

6.1 Arbitrary State Up To N=2: $\alpha |0\rangle + \beta |1\rangle + \gamma |2\rangle$

Both SPDC and 4WM produce a two-mode squeezed state which can be written in the Fock basis as in equation (2.26). By heralding on precisely n photons in the trigger channel, we collapse the signal channel to the Fock state $|n\rangle$. Suppose however that we interfere the idler with an auxiliary state with some mean photon number. Now when we detect n photons in the idler channel we don't know if n are from the idler, or $n-1$ from the idler and 1 from the auxiliary state, and so on. We are thus left with a coherent

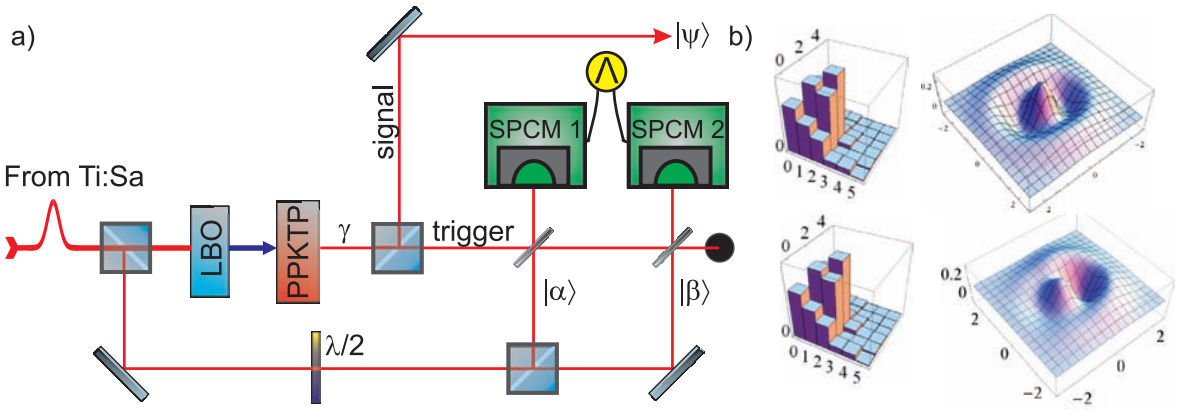

Figure 6.1: (a) The setup for observing an arbitrary superposition of $|0\rangle$, $|1\rangle$, and $|2\rangle$ states. A pulsed Ti:Sa drives a LBO crystal to produce a second harmonic pulse which in turn drives SPDC in a PPKTP crystal. This creates a two mode squeezed state. The trigger (idler) mode is interfered with two coherent state pulses $|\alpha\rangle$ and $|\beta\rangle$. Upon two-fold coincidence, the signal state is collapsed to equation (6.2). (b) A pair of states acquired in the setup. The upper state is $|\psi\rangle = \frac{8}{3\sqrt{2}}|0\rangle + \frac{1}{2}|2\rangle$. The lower state is: $|\psi\rangle = \left(\frac{18}{5\sqrt{2}} - i\frac{3}{2}\right)|0\rangle + \frac{5}{4}|1\rangle + \frac{1}{2}|2\rangle$.

superposition of n photons in the signal channel. The weighting and relative phase of the superposition state may be manipulated by adjusting the auxiliary field.

Figure 6.1a shows our implementation of this scheme for creating an arbitrary state up to $N = 2$. An SPDC process driven by a pulsed Ti:Sa laser was used to produce a two-mode squeezed state parameterized by $\gamma \equiv (\frac{\sinh\zeta}{\cosh\zeta})^2$ is in equation(2.26). Two auxiliary coherent states $|\alpha\rangle$ and $|\beta\rangle$ were tapped off from the same laser. The magnitudes of α, β, and γ were chosen so that the probability of having more than two photons in the system at a given time was negligible. In order to maintain phase stability between these states and the SPDC trigger photons, calcite beam displacers were used [36] in place of standard beamsplitters (not shown in the figure). Conditioned on a simultaneous click in both SPCMs, the state $|\psi\rangle$ was recorded using optical homodyne tomography. This dual-coincidence could correspond to three possibilities: **A:** both photons originated from the SPDC process implying that the signal state is $|2\rangle$. This occurs with probability

$\Pr_2 \propto \gamma^2$. **B:** Precisely one photon came from SPDC, the other from a coherent state, leaving the signal channel in state $|1\rangle$. Owing to Hong-Ou-Mandel interference [7], the probability of $|\alpha\rangle$ being detected on the first SPCM vanishes, so that the probability of this occurring is $\Pr_1 \propto \beta\gamma$. **C:** Both photons came from the auxiliary coherent states, so that the signal channel is vacuum. The probability of this is proportional to the coherent state amplitudes.

Since the photons from the coherent states and the SPDC were made indistinguishable through mode-matching and narrow filtering of the PPKTP output, each of these possibilities are indistinguishable, yielding a coherent superposition state. The constants of proportionality in the above are calculated to be [107]:

$$|\psi\rangle = \left(-\frac{\alpha^2}{2\sqrt{2}} + \frac{\alpha\beta}{2}\right)|0\rangle + \frac{\beta\gamma}{2}|1\rangle + \frac{\gamma^2}{2}|2\rangle\,. \tag{6.2}$$

The conditioned states were reconstructed using optical homodyne tomography. Figure 6.1b displays a sample of the density matrices and corresponding Wigner functions produced in the experiment by varying α, β, and γ. In each case, the density matrix corrects for a loss of 55% by means of iterative maximum likelihood. A gallery of the produced states is presented in [36].

6.2 Extension to Narrowband Light: $\alpha|0\rangle + \beta|1\rangle$

The above experiment succeeded in creating arbitrary superpositions of Fock states. However, the light produced was not compatible with atomic-based experiments and quantum information protocols. Aside from the wavelength of 791 nm, the bandwidth of the light was 383 GHz despite spectral filtering of the trigger. Since our 4WM system can be seen as a narrow-band alternative to SPDC, a natural step was to engineer arbitrary states as in our SPDC experiment with this new source.

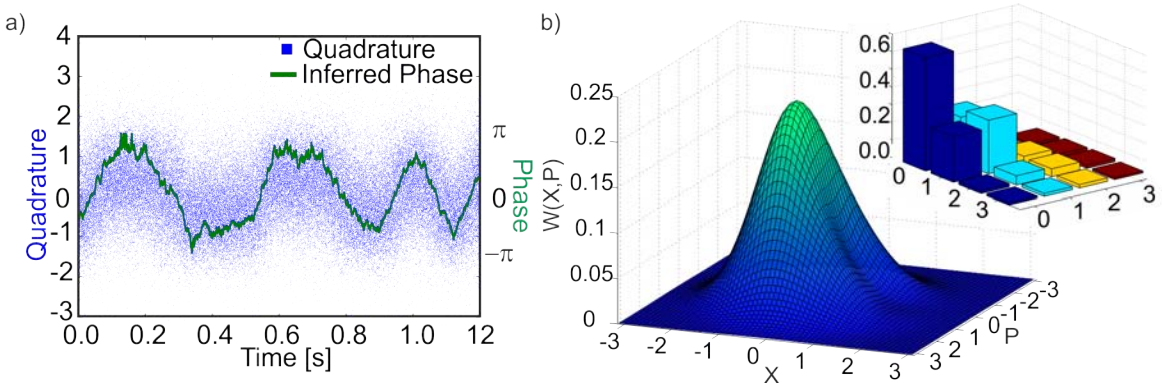

Figure 6.2: (a) The local oscillator phase was inferred by observing the mean quadrature value at a particular time. (b) The obtained density matrix corrected for a transmission of $\eta = 0.75$.

As a proof of principle demonstration, we sought to produce a coherent superposition state of $|0\rangle$ and $|1\rangle$. In order to achieve this, we weakly seeded the trigger channel with a coherent state which had mean photon number on the same order of magnitude as the squeezed vacuum output $\bar{n} \approx G - 1 \approx 0.2$. The experimental setup was identical figure 5.1 except that the seed from the double passed AOM was unblocked and highly attenuated. Now, a trigger event could either be due to the coherent seed (amplitude α) or from the 4WM process (probability $(G-1)/G$). The gain was kept sufficiently low so that the probability of stimulating a second photon from the seed was much less than the probability of spontaneous emission. The coherent state was calibrated to give the same count rate as the unseeded 4WM process.

Unlike the Fock state generation, the coherent superposition of vacuum and photon state was not phase insensitive and for each value, a corresponding quadrature phase was required. To accomplish this, we noted that for the state $|\psi\rangle = \alpha|0\rangle + \beta|1\rangle$, the mean quadrature is $\left\langle \hat{X}_\theta \right\rangle = \frac{|\alpha\beta|}{\sqrt{2}} \cos\theta'$ where $\theta' = \theta - \arg(\alpha^*\beta)$ is the difference between the local oscillator phase and the relative phase of α and β. By tracking the mean quadrature value throughout the course of the measurement, we extracted the phase of the local

oscillator with respect to the generated state. Specifically, we took a running average over several hundred successive measurements yielding a well defined mean quadrature over the corresponding time interval $\bar{X}_t$. The phase was then extracted as $\theta_t = \cos^{-1}(\bar{X})$. One such phase tracking measurement is shown in figure 6.2a.

The reconstructed density measurement of an experimental run for an approximately equal superposition of $|0\rangle$ and $|1\rangle$ is shown in figure 6.2b. The density matrix was found to contain strong coherence terms providing evidence that a coherent superposition, rather than a statistical mixture was created. Quantitatively, we found the density matrix correcting for an estimated loss of 25% to have $\rho_{00} = .64$, $\rho_{11} = .25$, and $\rho_{01} = .24i - .03$, whereas for a pure superposition state $(|0\rangle + e^{i\phi}|1\rangle)/\sqrt{2}$, $\rho_{00} = \rho_{11} = |\rho_{01}| = 0.5$. The Wigner function shows a coherent displacement as well as a non-Gaussian "dimple" near the origin owing to the single photon component. Analogous to expression (4.26) for squeezing efficiency, we can consider the generalized efficiency of the single-rail optical qubit. As before, the efficiency is the transmissivity of an absorbing medium though which a pure state propagates to obtain the experimentally measured state. In terms of the density matrix elements, this is [108]:

$$\eta_{qubit} = \frac{\rho_{11}}{1 - |\rho_{01}|^2 / \rho_{11}}. \tag{6.3}$$

For the state above, the corresponding efficiency is 0.32. It is expected that this preliminary result can be improved upon with increased visibility between the seed and 4WM modes.

6.3 Coherent Superpositions of Collective Atomic Excitations

The fact that our system can be seen as an "atomic SPDC process" opens up an interesting possibility: Compared to bulk materials at room temperature, the ground state

coherence of atomic vapours is extremely long lived. This has already been utilized to store heralded single atomic excitations [26, 27], following the protocol of Duan, Lukin, Cirac, and Zoller [109]. By employing the conditional measurements on the heralding photon, we could prepare arbitrary superposition states of collective atomic excitations. We could then read-out this atomic state in the form of a corresponding optical superposition state.

6.3.1 The DLCZ protocol

The DLCZ protocol outlines a technique for long distance quantum communication by employing entanglement swapping between intermediate nodes. At the heart of the DLCZ protocol is the concept of collective enhancement of photon generation owing to constructive interference.

The basic idea is outlined in figure 6.3. We start with an ensemble of Λ configuration three-level atoms, with meta-stable states $|g\rangle$ and $|e\rangle$ and excited state $|x\rangle$. The ensemble is prepared in the ground state $|g\rangle$: $|\Psi_0\rangle = |g_1 g_2 \dots g_n\rangle$. A weak, off-resonant "write" pulse is applied to the sample which, with some probability, scatters a "Stokes" photon into a solid angle covered by an SPCM. At this point there is a single excitation amongst the atoms. The detector is placed a distance from the ensemble such that it is fundamentally uncertain as to which atom emitted the Stokes photon[1] and the resultant state is a superpositions all permutations of a single excitation to state $|e\rangle$. This states known as a collective spin excitation (CSE) $|\Psi_e\rangle = N^{-1/2}\left(e^{i\phi_1}|e_1 g_2 \dots g_N\rangle + \dots + e^{i\phi_N}|g_1 g_2 \dots e_N\rangle\right)$, where the phase terms account for the momentum kick acquired in the Raman scattering. This excitation is now stored in the atoms and is ready to be read out.

This read-out is accomplished by means of a strong on-resonance "read" pulse which

[1]Operationally, this is accomplished by making the distance to the detector much larger than the cloud dimensions. The angle between photons emitted from opposite sides of the cloud is thus sufficiently small so that two photons emitted from any part of the cloud show good interference visibility.

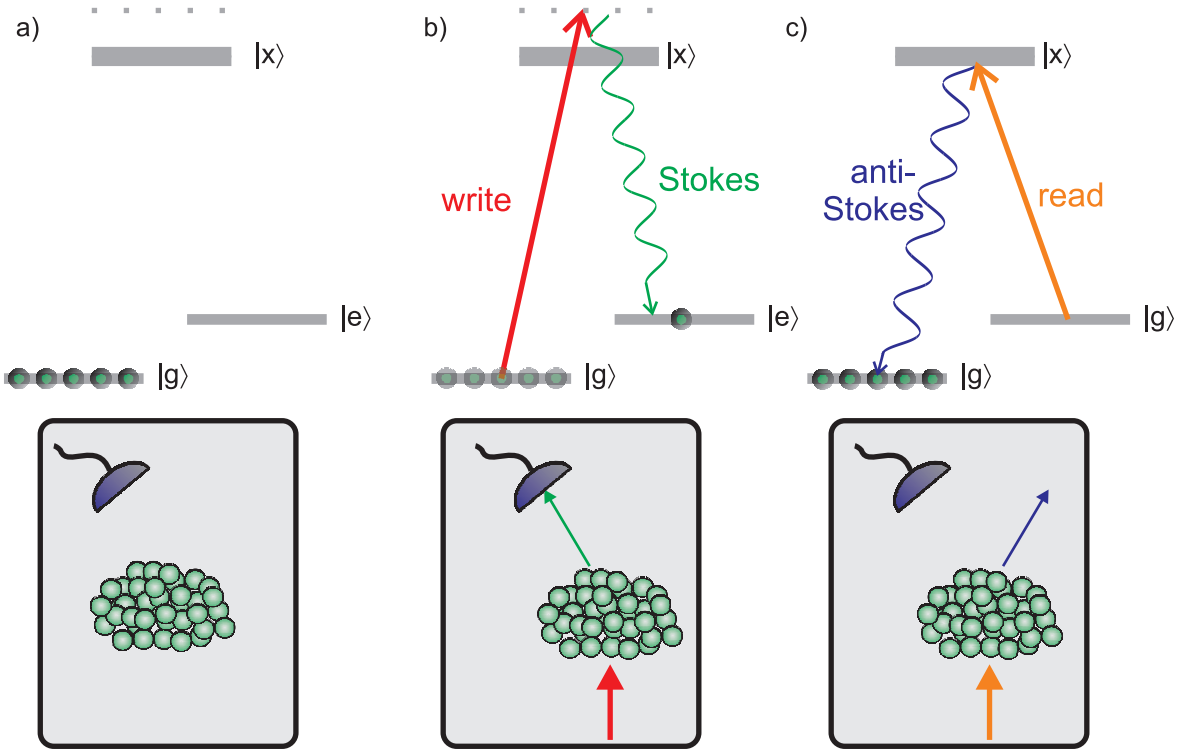

Figure 6.3: Basic sketch of the DLCZ idea. (a) An ensemble of 3-level atoms in Λ configuration are prepared in state $|g\rangle$. A fixed SPCM monitors the atoms for fluorescence. (b) An off resonant "write pulse" creates a scattered "Stokes" photon from the ensemble, creating a single collective excitation in state $|e\rangle$. (c) Some time later, a resonant "write" pulse pumps the atom back into state $|g\rangle$. The scattered "anti-Stokes" photon is emitted with high probability into the direction which satisfies phase-matching.

converts the atomic excitation back into optical form via Raman scattering of an "anti-Stokes" photon. Owing to collective interference from the accumulation of the phase factors, there is a strong enhancement of probability of the anti-Stokes photon being emitted in the phase-matched direction. Specifically, the CSE may be written as:

$$|\Psi_e\rangle = \frac{1}{\sqrt{N}} \sum_{n=1}^{N} e^{i(\mathbf{k}_s - \mathbf{k}_w)\cdot \mathbf{r}_n} |g_1 \dots e_n \dots g_N\rangle \tag{6.4}$$

where $\mathbf{k}_{s(w)}$ is the k-vector of the Stokes (write) photon. The creation of a CSE can also be written in terms of a collective atomic creation operator:

$$|\Psi_e\rangle = \hat{S}^\dagger |g_1 \dots g_N\rangle . \tag{6.5}$$

After application of the read pulse, the anti-Stokes scattering event occurs with some probability, causing another momentum kick $\mathbf{k}_a - \mathbf{k}_r$. With $\Delta\mathbf{k} \equiv \mathbf{k}_s + \mathbf{k}_a - \mathbf{k}_w - \mathbf{k}_r$, the state some short time after the arrival of the read pulse is:

$$|\Psi_e\rangle = \frac{\sum_{n=1}^{N} e^{i(\mathbf{k}_s - \mathbf{k}_w)\cdot \mathbf{r}_n} |g_1 \dots e_n \dots g_N\rangle \otimes |0_{as}\rangle + \left[\sum_{n=1}^{N} e^{i\Delta\mathbf{k}\cdot\mathbf{r}_n}\right] |g_1 \dots g_N\rangle \otimes |1_{as}\rangle}{\sqrt{N + \left|\sum_n e^{i\Delta k \cdot r_n}\right|^2}}, \tag{6.6}$$

where $|n_{as}\rangle$ represents the number of anti-Stokes emissions. From this we can infer the probability per unit time of emitting an anti-Stokes photon, as a function of emission direction, which determines $\Delta\mathbf{k}$. Since $\lim_{N\to\infty} \sum_{n=1}^{N} e^{i\Delta\mathbf{k}\cdot\mathbf{r}_n} = \delta^{(3)}(\Delta\mathbf{k})$, the probability that the anti-Stokes direction satisfies $\Delta\mathbf{k} = 0$ goes as $1 - \frac{1}{N}$. Since for typical experiments $N \approx 10^{13}$, this probability is effectively unity.

The above dynamics can be described by the Hamiltonian [110]

$$\hat{H} = \chi \left(\hat{a}^\dagger \hat{S}^\dagger + \hat{a}\hat{S}\right) \tag{6.7}$$

where $\hat{a}$ is the annihilation operator in the Stokes mode. Note that this Hamiltonian is identical to that of SPDC, but describes a two-mode state between the Stokes channel and collective atomic state.

6.3.2 Arbitrary Superpositions of Collective Spin Excitations

The experiments described in chapter 4 can be viewed as an instantaneous write-in read-out DLCZ experiment, with the pump acting as both the read and write fields, the Stokes as the trigger and the anti-Stokes as the signal. The results of section 6.2 thus served as a proof of principle demonstration of the creation of a superposition of collective atomic excitations. While these experiments unitized only the first order terms in the Hamiltonian (6.7), higher order terms can be employed as was done for SPDC in section 6.1, and the engineering of collective spin excitations can be extended to higher N. One way of achieving this is to employ multiple partial photon subtractions as outlined in figure 6.4. The trigger photon passes through N stages each consisting of a low-reflectivity beam splitter with reflection coefficient r_i and an incident coherent state with amplitude α_i. At each stage, an SPCM monitors the reflected port of the beam-splitter, and an additional SPCM monitors the final transmitted port. The state $|\psi\rangle$ is heralded upon each reflected-port SPCM clicking and the absence of a click in the final transmitted port.

To see how this prepares an arbitrary state, note first that each stage the click could come from the coherent state (so that $|\psi_{i+1}\rangle \rightarrow |\psi_i\rangle$) with probability amplitude $(1 - r_i^2)\alpha \approx \alpha$, or from $|\psi_i\rangle$ in which case $|\psi_{i+1}\rangle \rightarrow \hat{a}\,|\psi_i\rangle$, with amplitude r_i. Thus each partial photon subtraction stage performs the operation $\hat{A}_i = (\alpha_i + r_i\hat{a})$. After N of these operations the state is transformed to:

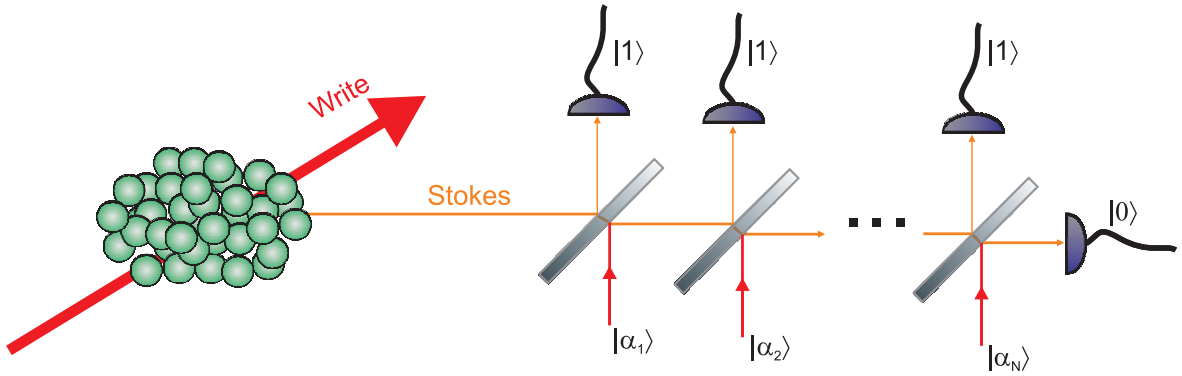

Figure 6.4: Scheme for generating the state $\sum_{n=0}^{N} c_n |n\rangle$. There are N stages each consisting of a low-reflection beam splitter and an incident coherent state. The state is heralded upon a click in each of the upper detectors and a null-detection in the right-most detector.

$$\begin{aligned} |\psi\rangle &= \prod_{i=1}^{N} \hat{A}_i |\psi_{in}\rangle \\ &= (\alpha_1 + r_1\hat{a})(\alpha_2 + r_2\hat{a}) \cdots (\alpha_N + r_N\hat{a}) |\psi_{in}\rangle \\ &= \left(\beta_0 + \beta_1\hat{a} + \cdots + \beta_N\hat{a}^N\right) |\psi_{in}\rangle , \end{aligned} \tag{6.8}$$

where $\beta_i = \beta_i(r_1, \ldots, r_N, \alpha_1, \ldots, \alpha_N)$ are the coefficients of the resultant polynomial.

With the input state written in the basis $|\text{Stokes field}\rangle_s \otimes |\text{Atomic Excitations}\rangle_a$ given by $|\psi_{in}\rangle = \sum_n \gamma^n |n\rangle_s |n\rangle_a$, and null detection on the final SPCM, the atomic state collapses to:

$$\begin{aligned} |\psi\rangle_a &= \langle 0|_s \sum_{n,m} \beta_m \hat{a}^m \gamma^n |n\rangle_s |n\rangle_a \\ &= \sum_{m,n<m} \gamma^n \beta_m \sqrt{\frac{m!}{(m-n)!}} \langle 0|m-n\rangle_s |n\rangle_a \\ &= \sum_n \gamma^n \beta_n \sqrt{n!} |n\rangle_a \\ &= \sum_n c_n |n\rangle_a , \end{aligned} \tag{6.9}$$

where the c_n are functions of (r_i, α_i) through the β_i. For a given set $\{c_i\}$ we can then find the unique $\{r_i, \alpha_i\}$ which determine these values. We know that these values exist from the fundamental theorem of algebra[2]. We thus have, at least in principle, a method to create *any* collective atomic state. Technically, this will be limited by the dark count rate and quantum efficiency of the detector. Also, for increasing N, the mean photon number in each state must be kept sufficiently low to ensure only N photons are present for a given realization. Thus even with perfect detectors, states with large photon numbers will be ultimately limited by the lifetime of the experimenter[3].

[2]The FTA states that an n^{th} order polynomial has n roots. Since here $\sum_n \beta_n \hat{a}^n = \prod_i (\alpha_i + r_i \hat{a})$, the $\{r_i, \alpha_i\}$ are just the roots of the polynomial $\sum_n \beta_n \hat{a}^n$.

[3]Or, at the very least, the duration experimenter's funding.

Chapter 7

Conclusions and Outlook

The work presented in this thesis has both practical and fundamental aspects. On one hand, the generation of narrow-band non-classical light resonant to atomic Rubidium is of high practical value. For example, storage and retrieval of non-classical light is a far more convincing test of a quantum memory than a classical signal at the single photon level, and atom based single photon nonlinearities [111] could form quantum logic gates. In addition, a qubit formed from such a photon may be used in the myriad atom-based examples for optical quantum computing. On the other hand, this work has looked at the unexplored area of controllably manipulating superposition states of CSEs. This allows us to begin to explore the isomorphism between the optical and collective-atomic Hilbert spaces and provides a new testbed for quantum information protocols.

The natural next step in terms of the practicality of the non-classical light source is to interface single photons with atomic ensembles, and perform simple operations. A introductory proof-of-principle demonstration will be to observe linear absorption from a cold atom trap. Owing to the one-photon tuneability of the source, simple spectroscopy could be performed with individual light quanta. Once suitable light-atom coupling is achieved, a future step will involve storing and retrieving a single photon state from the atomic gradient echo memory (GEM) [73] in our laboratory. GEM allows for high retrieval efficiencies of over 80% so that the non-classical character of the stored light may be observed after retrieval. One challenge associated with this will be to match the frequency of the quantum memory to that of the photons. This can be overcome in two steps. In order to match the relatively narrow bandwidth (on the order of 1 MHz) of our current GEM setup, an additional spectral filter in the trigger channel can be employed.

The high spectral brightness of our photon source allows us to achieve this filtration while maintaining a high experimental repetition rate. In order to operate the memory and the source at the same absolute frequency, each pump laser can be locked to an atomic line by means of saturated absorption spectroscopy.

Another interesting experiment to perform would be that of heralded photon amplification. In this experiment, a single photon generated in the atomic source would be fed into another 4WM setup or into the same cell. A photon click gated to be synchronized with the arrival of the seed photon would herald the creation of a two photon Fock state. Since we operate with gain $G = 1.1$ in our setup, this will occur at a rate approximately 10 times less than the single photon count rate. Nevertheless, the high single photon count rates achieved (300,000 s^{-1} or higher) allow us to prepare Fock states up to $|4\rangle$. This could form an alternative to measuring $n > 1$ Fock states by $n-$fold photo detection in the trigger channel.

In terms of collective atomic superposition states, the immediate next step is to observe a transient collective superposition state using the protocol of [36] as outlined in section 6.3.2 but with continuous wave read/write fields. The next step will be more challenging. To fully utilize the long-lived ground state coherence of atomic ensembles, we will have to move to the pulsed regime, where we prepare the atomic superposition state, wait for some time, and then verify the atomic state via optical homodyne detection. One difficulty of this will be to scatter, with high probability, a Stokes photon in the trigger channel. In traditional DLCZ experiments, the probability of scattering into a particular spatial mode is low, and the experiment is repeated many times before a successful "write" event heralds an atomic excitation. The gain must then be sufficiently high to record an acceptable experimental count rate, but not so high as to increase the number of generated excitations. Another challenge will be to obtain the high retrieval efficiency in the pulsed regime, which was achieved in this work in the CW regime. So far,

our experiment has achieved a heralding efficiency approximately an order of magnitude higher than previous works, but this may be largely on account of the CW "4WM-regime" in which we work.

The underlying accomplishment of this work was the introduction of a new source of narrowband photons, which was built on the recent demonstrations of high quality multi-spatial mode squeezed light [32, 66]. Combining the high efficiency of this source with the idea of DLCZ opens up a territory in exploring the isomorphism between the optical and collective atomic Hilbert spaces. Owing to the novelty of the system, there are many potential avenues to explore and we can't say for certain what will be discovered. Although my time with the experimental setup is sadly over, it is now in the hands of the next generation of graduate students in our lab, and ultimately the future success or failure of the above ideas is in their able hands. I am confident that we have only seen the beginning of the experiments which come out of this technology. I look forward to reading about it in the future.

Appendix A

Properties of the Two Mode Sqeezing Operator

The operator (2.21) stems from the Hamiltonian:

$$\hat{H} = i\hbar\left(\gamma\hat{a}^\dagger\hat{b}^\dagger - \gamma^*\hat{a}\hat{b}\right) \tag{A.1}$$

The evolution of for example $\hat{a}$ is then given by:

$$\begin{aligned}\frac{d\hat{a}}{dt} &= \frac{1}{i\hbar}\left[\hat{H},\hat{a}\right] \\ &= \frac{1}{i\hbar}\left[i\hbar\left(\gamma\hat{a}^\dagger\hat{b}^\dagger - \gamma^*\hat{a}\hat{b}\right),\hat{a}\right] \\ &= \gamma\left[\hat{a}^\dagger,\hat{a}\right]\hat{b}^\dagger \\ &= -\gamma\hat{b}^\dagger.\end{aligned} \tag{A.2}$$

Similarly,

$$\begin{aligned}\frac{d\hat{b}^\dagger}{dt} &= \frac{1}{i\hbar}\left[i\hbar\left(\gamma\hat{a}^\dagger\hat{b}^\dagger - \gamma^*\hat{a}\hat{b}\right),\hat{b}^\dagger\right] \\ &= -\gamma^*\hat{a}\left[\hat{b},\hat{b}^\dagger\right] \\ &= -\gamma^*\hat{a}.\end{aligned} \tag{A.3}$$

Differentiating (A.2) and substituting (A.3) yeilds:

$$\frac{d^2\hat{a}}{dt^2} = |\gamma|^2\,\hat{a} \rightarrow \hat{a} = A\cosh(|\gamma t|) + B\sinh(|\gamma t|). \tag{A.4}$$

For the initial conditions we have $\hat{a}(0) = A$, $d\hat{a}(0)/dt = |\gamma|\,B = -|\gamma|\,\hat{b}^\dagger$. Letting $\zeta = \gamma t$ and choosing ζ to be real[1] we arrive at the squeezing transformation for $\hat{a}$. The corresponding transformation for $\hat{b}$ follows from direct substitution, and $\hat{a}^\dagger$, $\hat{b}^\dagger$ follow by taking the Hermitian conjugate of above:

[1]Experimentally, this corresponds to choosing particular overall reference phase of the local oscillator.

$$\begin{aligned}
\hat{a} &\to \hat{a}\cosh(\zeta) - \hat{b}^\dagger \sinh(\zeta) \\
\hat{b} &\to \hat{b}\cosh(\zeta) - \hat{a}^\dagger \sinh(\zeta) \\
\hat{a}^\dagger &\to \hat{a}^\dagger \cosh(\zeta) - \hat{b}\sinh(\zeta) \\
\hat{b}^\dagger &\to \hat{b}^\dagger \cosh(\zeta) - \hat{a}\sinh(\zeta).
\end{aligned} \tag{A.5}$$

The joint quadrature operators (2.22) have simple transformation properties. For example:

$$\begin{aligned}
\hat{S}^\dagger \hat{X_+} \hat{S} &= \frac{\hat{S}^\dagger \hat{X}_a \hat{S} + \hat{S}^\dagger \hat{X}_b \hat{S}}{\sqrt{2}} \\
&= \frac{\hat{S}^\dagger \hat{a} \hat{S} + \hat{S}^\dagger \hat{a}^\dagger \hat{S}}{2} + \frac{\hat{S}^\dagger \hat{b} \hat{S} + \hat{S}^\dagger \hat{b}^\dagger \hat{S}}{2} \\
&= \frac{\hat{a}\cosh(\zeta) - \hat{b}^\dagger \sinh(\zeta) + \hat{a}\cosh(\zeta) - \hat{b}^\dagger \sinh(\zeta)}{2} \\
&\quad + \frac{\hat{a}\cosh(\zeta) - \hat{b}^\dagger \sinh(\zeta) + \hat{a}\cosh(\zeta) - \hat{b}^\dagger \sinh(\zeta)}{2} \\
&= \frac{\hat{a} + \hat{a}^\dagger + \hat{b} + \hat{b}^\dagger}{2} \left(\cosh(\zeta) - \sinh(\zeta)\right). \\
&= \frac{\hat{X}_a + \hat{X}_b}{\sqrt{2}} e^{-\zeta} \\
&= \hat{X}_+ e^{-\zeta}
\end{aligned} \tag{A.6}$$

and by the same analysis:

$$\begin{aligned}
\hat{X}_- &\to \hat{X}_- e^{\zeta} \\
\hat{P}_+ &\to \hat{P}_- e^{\zeta} \\
\hat{P}_- &\to \hat{P}_+ e^{-\zeta}
\end{aligned} \tag{A.7}$$

Appendix B

Properties of the Thermal State

Defining the parameter $\gamma \equiv \frac{G-1}{G}$, we can write the thermal state density matrix as:

$$\hat{\rho}_{\rm th} = \frac{1}{G}\sum_{n=0}^{\infty} \gamma^n \left|n\right\rangle\!\left\langle n\right| . \tag{B.1}$$

The mean photon number $\bar{n} \equiv \langle \hat{n} \rangle$ is then:

$$\begin{aligned}
\bar{n} &= {\rm Tr}\left[\hat{\rho}_{\rm th}\hat{n}\right] \\
&= \frac{1}{G}\sum_{m,n} \gamma^n \left\langle m|n\right\rangle \left\langle n\right| \hat{n} \left|m\right\rangle \\
&= \frac{1}{G}\sum_{n,m} \gamma^n \hat{m}\delta_{mn} \\
&= \frac{1}{G}\sum_{n} n\gamma^n \\
&= \frac{1}{G}\frac{\gamma}{(1-\gamma)^2} \\
&= G-1,
\end{aligned} \tag{B.2}$$

where we've noted that $(1-\gamma)^{-1} = G$ and the sum $\sum_n nx^n = \frac{x}{(1-x)^2}$ was computed as $\sum_n nx^n = x\frac{d}{dx}\sum_n x^n = x\frac{d}{dx}\frac{1}{1-x} = \frac{x}{(1-x)^2}$. Similarly we can compute $\sum_n n^2x^n = \frac{x(1+x)}{(1-x)^3}$. Continuing along these lines we find:

$$\begin{aligned}
\left\langle \hat{n}^2 \right\rangle &= \mathrm{Tr}\left[\hat{\rho}_{th}\hat{n}^2\right] \\
&= \frac{1}{G}\sum_{m,n}\gamma^n m^2 \delta_{mn} \\
&= \frac{1}{G}\sum_{n} n^2\gamma^n \\
&= \frac{1}{G}\frac{\gamma(1+\gamma)}{(1-\gamma)^3} \\
&= (G-1)(2G-1),
\end{aligned} \tag{B.3}$$

so that $\langle \Delta\hat{n}^2 \rangle$ is

$$\begin{aligned}
\left\langle \Delta\hat{n}^2 \right\rangle &= \left\langle \hat{n}^2 \right\rangle - \bar{n}^2 \\
&= (G-1)(2G-1) - (G-1)^2 \\
&= G(G-1) \\
&= \bar{n}^2 + \bar{n}.
\end{aligned} \tag{B.4}$$

In a similar manner we can compute $\left\langle \Delta\hat{X}^2 \right\rangle$ for the thermal state. From the symmetry of the Wigner function, $\left\langle \hat{X} \right\rangle_{\mathrm{th}} = 0$ so that $\left\langle \Delta\hat{X}^2 \right\rangle = \left\langle \hat{X}^2 \right\rangle_{\mathrm{th}}$. Thus

$$\begin{aligned}
\left\langle \Delta\hat{X}^2 \right\rangle &= \frac{1}{G}\sum_{n}\gamma^n \left\langle n\right| \hat{X}^2 \left|n\right\rangle \\
&= \frac{1}{2G}\sum_{n}\gamma^n(2n+1) \\
&= \frac{1}{G}\frac{\gamma}{(1-\gamma)^2} + \frac{1}{2G}\frac{1}{1-\gamma} \\
&= (G-1) + \frac{1}{2} \\
&= \frac{2\bar{n}+1}{2}.
\end{aligned} \tag{B.5}$$

Note that this is the just the quadrature variance of the Fock state $|n\rangle$.

Appendix C

Some Properties of Gaussian Beams

Since lasers generally consist of a gain medium inside a spherical resonator, the transverse intensity profile given by a mode of such a resonator[1], namely a Hermite-Gauss Mode of order m, n denoted TEM_{mn} [112]. The fundamental mode TEM_{00} has a cylindrically symmetric Gaussian transverse profile which may be written as:

$$I(r) = I_0 e^{-2\left(\frac{r}{w(z)}\right)^2}. \tag{C.1}$$

The quantity w_0 is known as the beam waist and describes the radius at which the intensity drops by a factor of e^{-2}. Owing to diffraction, the $w(z)$ has a minimum value and diverges as $z \to \infty$. Although the waist increases, the profile remains Gaussian as per equation (C.1). For convenience, $z = 0$ corresponds to the minimum waist: $w_0 \equiv w(0)$.

A key parameter is the distance z over which the beam has diffracted to $\sqrt{2}w_0$. This distance, known as the Rayleigh range is given by:

$$z_R \equiv \frac{\pi w_0^2}{\lambda}. \tag{C.2}$$

The general dependence of the waist as a function of z can be written in terms of z_R as:

$$w(z) = w_0\sqrt{1 + \left(\frac{z}{z_R}\right)^2}. \tag{C.3}$$

Note that for distances well outside the Rayleigh range, the divergence is linear: $w(z) \approx \theta_0 z$, with

[1] i.e. a solution to the Maxwell equations subject to the spherical boundary conditions.

$$\theta_0 = \frac{\lambda}{\pi w_0}. \tag{C.4}$$

Unlike a plane wave, the phase front of a TEM mode is not constant across any plane z apart from the origin. Instead, the constant phase fronts are approximately spherical with radius:

$$R(z) = z\left(1 + \left(\frac{z_R}{z}\right)^2\right). \tag{C.5}$$

As compared to their plane-wave counterparts, Gaussian beams acquire an additional phase factor over an on-axis propagation distance z. This factor known as the Gouy phase shift is given for a TEM_{mn} by:

$$\phi_G = (1 + m + n)\tan^{-1}\frac{z}{z_R}. \tag{C.6}$$

Appendix D

Relative Intensity Squeezing in the Presence of Loss (3.7)

The mean photon number of the seeded signal field after the 4WM process is

$$\begin{aligned}
\langle \hat{n}_s \rangle &= \langle \alpha, 0 | \, \hat{S}^\dagger \hat{a}_s^\dagger \hat{a}_s \hat{S} \, | \alpha, 0 \rangle \\
&= \langle \alpha, 0 | \, \hat{S}^\dagger \hat{a}_s^\dagger \hat{S} \hat{S}^\dagger \hat{a}_s \hat{S} \, | \alpha, 0 \rangle \\
&= \langle \alpha, 0 | \left(\hat{a}_s^\dagger \cosh(\zeta) - \hat{a}_i \sinh(\zeta) \right) \left(\hat{a}_s \cosh(\zeta) - \hat{a}_i^\dagger \sinh(\zeta) \right) | \alpha, 0 \rangle \\
&= \langle \alpha | \, \hat{n}_s \, | \alpha \rangle \cosh^2(\zeta) + \langle \alpha | \alpha \rangle \sinh^2(\zeta) \\
&= |\alpha|^2 \cosh^2(\zeta) + \sinh^2(\zeta),
\end{aligned} \tag{D.1}$$

where we've inserted the identity operator $S^\dagger S$ in the second step.

Along the same lines we compute:

$$\langle n_i \rangle = (1 + |\alpha|^2) \sinh^2(\zeta). \tag{D.2}$$

We compute $\langle n_s^2 \rangle$ via $\langle \alpha | \, \hat{S}^\dagger \hat{a}_s^\dagger \hat{S} \hat{S}^\dagger \hat{a}_s \hat{S} \hat{S}^\dagger \hat{a}_s^\dagger \hat{S} \hat{S}^\dagger \hat{a}_s \hat{S} \, | \alpha \rangle$ to obtain

$$\left\langle n_s^2 \right\rangle = |\alpha|^2 \left(1 + |\alpha|^2\right) \cosh^4(\zeta) + \left(3 |\alpha|^2 + 1\right) \cosh^2(\zeta) \sinh^2(\zeta) + \sinh^4(\zeta), \tag{D.3}$$

so that

$$\begin{aligned}
\left\langle \Delta \hat{n}_s^2 \right\rangle &= \left\langle \hat{n}_s^2 \right\rangle - \langle \hat{n}_s \rangle^2 \\
&= |\alpha|^2 \left(1 + |\alpha|^2\right) \cosh^4(\zeta) + 3 |\alpha|^2 \cosh^2(\zeta) \sinh^2(\zeta) + \cosh^2(\zeta) \sinh^2(\zeta) \\
&\quad + \sinh^4(\zeta) - |\alpha|^4 \cosh^4(\zeta) - 2 |\alpha|^2 \cosh^2(\zeta) \sinh^2(\zeta) - \sinh^4(\zeta) \\
&= |\alpha|^2 \cosh^2(\zeta)(\cosh^2(\zeta) + \sinh^2(\zeta)) + \cosh^2(\zeta) \sinh^2(\zeta).
\end{aligned} \tag{D.4}$$

so that for large α, this becomes $\langle \Delta \hat{n}_s \rangle^2 = |\alpha|^2 G(2G-1)$. We calculate the variance for the idler channel in the same manner to obtain:

$$\left\langle n_i^2 \right\rangle = (1+|\alpha|^2)\cosh^2(\zeta)\sinh^2(\zeta) + (1+3|\alpha|^2+|\alpha|^4)\sinh^4(\zeta), \tag{D.5}$$

and

$$\langle \Delta \hat{n}_i \rangle^2 = |\alpha|^2 \sinh^2(\zeta)(\cosh^2(\zeta)+\sinh^2(\zeta)) + \cosh^2(\zeta)\sinh^2(\zeta). \tag{D.6}$$

Note that in the case of no seed, $\langle \Delta \hat{n}_s \rangle^2 = \langle \Delta \hat{n}_i \rangle^2 = \cosh^2(\zeta)\sinh^2(\zeta)$.

Similarly we find

$$\langle \hat{n}_s \hat{n}_i \rangle = (1+3|\alpha|^2+|\alpha|^4)\cosh^2(\zeta)\sinh^2(\zeta)(1+|\alpha|^2)\sinh^4(\zeta) \tag{D.7}$$

so that using eqs. (D.1) and (D.2),

$$\mathrm{cov}(\hat{n}_s \hat{n}_i) = \langle \hat{n}_s \hat{n}_i \rangle - \langle \hat{n}_s \rangle \langle \hat{n}_i \rangle = \cosh^2(\zeta)\sinh^2(\zeta)(1+2|\alpha|^2). \tag{D.8}$$

We can now combine equations D.4, D.6, and D.8 to obtain the solution to equation (4.22):

$$\begin{aligned}
\langle \Delta(\hat{n}_s - \hat{n}_i) \rangle^2 &= \langle \Delta \hat{n}_s \rangle^2 + \langle \Delta \hat{n}_i \rangle^2 - 2(\langle \Delta(\hat{n}_s \hat{n}_i) \rangle - \langle \hat{n}_s \rangle \langle \hat{n}_i \rangle) \qquad \text{(D.9)} \\
&= |\alpha|^2 \cosh^4(\zeta) + |\alpha|^2 \sinh^2(\zeta)\cosh^2(\zeta) + \sinh^2(\zeta)\cosh^2(\zeta) \\
&\quad + |\alpha|^2 \sinh^4(\zeta) + |\alpha|^2 \sinh^2(\zeta)\cosh^2(\zeta) + \sinh^2(\zeta)\cosh^2(\zeta) \\
&\quad -2\sinh^2(\zeta)\cosh^2(\zeta) - 4|\alpha|^2 \sinh^2(\zeta)\cosh^2(\zeta) \\
&= |\alpha|^2 (\cosh^4(\zeta) - 2\cosh^4(\zeta)\sinh^2(\zeta) + \sinh^4(\zeta)) \\
&= |\alpha|^2 (\cosh^2(\zeta) - \sinh^2(\zeta))^2 \\
\langle \Delta(\hat{n}_s - \hat{n}_i) \rangle^2 &= |\alpha|^2 .
\end{aligned}$$

To calculate the effect of losses, we model a loss in a given channel as a beamsplitter with transmissivity $t = \sqrt{\eta}$ as diagrammed in figure 4.7b. The action of the beamsplitters on a channel is given by the unitary beamsplitter formula [39]:

$$\begin{aligned} \hat{B}^\dagger \hat{a}_s \hat{B} &= t_s \hat{a}_s + r_s \hat{a}_{vac,s} \\ \hat{B}^\dagger \hat{a}_i^\dagger \hat{B} &= t_i \hat{a}_i^\dagger + r_i \hat{a}_{vac,i}^\dagger \end{aligned} \tag{D.10}$$

and so on, where $\hat{a}_{vac,s(i)}$ is the (vacuum) mode incident on the unused side of the signal (idler) beamsplitter. These additional modes now must be taken into account so that the state in (4.19) becomes:

$$|\psi\rangle = \hat{B}_s \hat{B}_i \hat{S}_{si} \hat{D}(\alpha)_s \left|0\right\rangle_s \left|0\right\rangle_i \left|0\right\rangle_{vac,s} \left|0\right\rangle_{vac,i}. \tag{D.11}$$

We can calculate the transformed quantities from the previous section in the same way. For example, equation (D.1) becomes:

$$\begin{aligned} \langle\psi| \hat{a}_s^\dagger \hat{a}_s |\psi\rangle &= \langle 0_{vac,s} 0_{vac,i} \alpha_s 0_i| \hat{S}_{si}^\dagger \hat{B}_i^\dagger \hat{B}_s^\dagger \hat{a}_s^\dagger \hat{B}_s \hat{B}_s^\dagger \hat{a}_s \hat{B}_s \hat{B}_i \hat{S}_{si} |0_{vac,s} 0_{vac,i} \alpha_s 0_i\rangle \\ &= \langle 0_{vac,s} \alpha_s 0_i| \hat{S}_{si}^\dagger (t\hat{a}_s^\dagger + r\hat{a}_{vac,s}^\dagger)(t\hat{a}_s + r\hat{a}_{vac,s}) \hat{S}_{si} |0_{vac,s} \alpha_s 0_i\rangle \langle 0_{vac,i}|0_{vac_i}\rangle \\ &= t_a^2 \langle \alpha_s 0_i| \hat{S}_{si}^\dagger \hat{n}_s \hat{S}_{si} |\alpha_s 0_i\rangle \\ &= \eta_s \langle \hat{n}_s \rangle_{\hat{S}} \end{aligned} \tag{D.12}$$

with $\langle \hat{n}_s \rangle_{\hat{S}}$ being the quantity already calculated in equation D.1. We similarly express the other previously calculated quantities in terms of the beamsplitter coefficients:

$$\begin{aligned}
\langle \hat{n}_s \rangle_{\hat{S}} &\rightarrow \eta_s \langle \hat{n}_s \rangle_{\hat{S}} \\
\langle \hat{n}_i \rangle_{\hat{S}} &\rightarrow \eta_i \langle \hat{n}_i \rangle_{\hat{S}} \\
\left\langle \hat{n}_s^2 \right\rangle_{\hat{S}} &\rightarrow \eta_s^2 \left\langle \hat{n}_s^2 \right\rangle_{\hat{S}} + \eta_s(1-\eta_s) \langle \hat{n}_s \rangle_{\hat{S}} \\
\left\langle \hat{n}_i^2 \right\rangle_{\hat{S}} &\rightarrow \eta_i^2 \left\langle \hat{n}_i^2 \right\rangle_{\hat{S}} + \eta_i(1-\eta_i) \langle \hat{n}_i \rangle_{\hat{S}} \\
\langle \hat{n}_s \hat{n}_i \rangle_{\hat{S}} &\rightarrow \eta_s \eta_i \langle \hat{n}_s \hat{n}_i \rangle_{\hat{S}} ,
\end{aligned} \tag{D.13}$$

yielding the following parameters used to calculate equation 4.24:

$$\begin{aligned}
\langle \Delta \hat{n}_s \rangle^2 &\rightarrow \eta_s^2 \langle \Delta \hat{n}_s \rangle^2 + \eta_s(1-\eta_s) \langle n_s \rangle \\
\langle \Delta \hat{n}_i \rangle^2 &\rightarrow \eta_i^2 \langle \Delta \hat{n}_i \rangle^2 + \eta_i(1-\eta_i) \langle n_i \rangle \\
\langle \hat{n}_s \hat{n}_i \rangle - \langle \hat{n}_s \rangle \langle \hat{n}_i \rangle &\rightarrow \eta_s \eta_i (\langle \hat{n}_s \hat{n}_i \rangle - \langle \hat{n}_s \rangle \langle \hat{n}_i \rangle).
\end{aligned} \tag{D.14}$$

Again, $G \approx 10$ and $|\alpha|^2 \approx 10^{10} \gg G$ so that we neglect terms which do not include α^1 and consider the relative intensity squeezing in the case of losses. Equation (4.22) is now normalized to $\eta_s |\alpha|^2 G + \eta_i |\alpha|^2 (G-1)$ to include these losses.

[1] i.e. the contributions from the (nondisplaced) vacuum input

Appendix E

Deferred Derivations of Equations Stated in Text

E.1 Derivation of equation (3.7)

By the Wiener-Khintchine theorem the measured spectrum is the Fourier transform of the autocorrelation of the temporal signal

$$S(\nu) = \int_{-\infty}^{\infty} \left\langle \hat{i}(t)\hat{i}(t+\tau) \right\rangle e^{2i\pi\nu\tau} d\tau \tag{E.1}$$

We can write the autocorrelation in terms of equation (3.3) to find

$$\begin{aligned} \left\langle \hat{i}(t)\hat{i}(t+\tau) \right\rangle = \gamma^2 \left\langle \int_{-\infty}^{\infty}\int_{-\infty}^{\infty} \hat{q}(t')\hat{q}(t'')r(t'-t)r(t-t''+\tau)dt'dt'' \right\rangle \\ +2\gamma \left\langle \int_{-\infty}^{\infty} \hat{q}(t')r(t-t')dt'\hat{i}_e(t) \right\rangle + \left\langle \hat{i}_e(t)\hat{i}_e(t+\tau) \right\rangle . \end{aligned} \tag{E.2}$$

Noting that the quantum noise is uncorrelated with the electronic noise and that $\langle q(t)\rangle = \langle i_e(t)\rangle = 0$, the second term vanishes. Also since for the vacuum state[1] $\hat{q}(t')\hat{q}(t'')) = \delta(t'-t'')$, (E.2) becomes:

$$\left\langle \hat{i}(t)\hat{i}(t+\tau) \right\rangle = \gamma^2 \int_{-\infty}^{\infty} r(t)r(t+\tau)dt + \langle i_e(t)i_e(t+\tau)\rangle \tag{E.3}$$

so that equation (E.1) is:

$$\begin{aligned} S(\nu) &= \gamma^2 \int_{-\infty}^{\infty}\int_{-\infty}^{\infty} r(t)r(t+\tau)e^{2i\pi\nu\tau}dtd\tau + \int_{-\infty}^{\infty} \left\langle \hat{i}_e(t)\hat{i}_e(t+\tau) \right\rangle d\tau \\ &= \gamma^2 \left|\tilde{r}(\nu)\right|^2 + S_e(\nu) \end{aligned} \tag{E.4}$$

[1] We measure the vacuum state by simply not putting any light into the signal port of the beam-splitter in figure 3.2.

where the convolution theorem was used in the second line. This shows that the spectrum is simply the sum of the electronic noise spectra and the Fourier transform of the response function scaled by the homodyne gain.

Next, from equation (3.4):

$$\begin{aligned}
\left\langle \hat{Q}^2_{\text{meas}} \right\rangle &= \gamma^2 \int_{-\infty}^{\infty} \int_{-\infty}^{\infty} \hat{q}(t')\hat{q}(t'')\psi'(t')\psi'(t'')dt'dt'' + \left\langle \hat{Q}^2_{\text{e}} \right\rangle \\
&= \gamma^2 \int_{-\infty}^{\infty} \left|\psi'(t)\right|^2 dt + \left\langle \hat{Q}^2_{\text{e}} \right\rangle \\
&= \gamma^2 \int_{-\infty}^{\infty} \left|\tilde{\psi}'(\nu)\right|^2 + \left\langle \hat{Q}^2_{\text{e}} \right\rangle \\
&= \gamma^2 \int_{-\infty}^{\infty} \left|\tilde{\psi}(\nu)\right|^2 \left|\tilde{r}(\nu)\right|^2 + \left\langle \hat{Q}^2_{\text{e}} \right\rangle
\end{aligned} \tag{E.5}$$

where Parseval's theorem was employed from line 2 to line 3. Now we can write $\left\langle \hat{Q}_{\text{e}} \right\rangle$ as the Fourier transform of the auto-convolution of $\hat{i}_e(t)\psi(t)$, i.e.

$$\hat{Q}^2_e = \int_{-\infty}^{\infty} s_e(\nu) \left|\tilde{\psi}(\nu)\right|^2 d\nu. \tag{E.6}$$

Finally, since $\left\langle \hat{Q}_{\text{meas}} \right\rangle = 0$, we have $\left\langle \Delta\hat{Q}^2_{\text{meas}} \right\rangle = \left\langle \hat{Q}^2_{\text{meas}} \right\rangle$. We can then combine equations (E.4), (E.5), and (E.6) to find:

$$\left\langle \Delta\hat{Q}^2_{meas} \right\rangle = \int_{-\infty}^{\infty} S(\nu) \left|\tilde{\psi}\right|^2 d\nu. \tag{E.7}$$

Inasmuch as $S(\nu)$ is constant, we can pull it out of the integral and find for some frequency ν_0 in this range:

$$\frac{\left\langle \Delta\hat{Q}^2_e \right\rangle}{\left\langle \Delta\hat{Q}^2_{meas} \right\rangle} = \frac{S_e(\nu_0) \int_{-\infty}^{\infty} \left|\tilde{\psi}\right|^2 d\nu}{S(\nu_0) \int_{-\infty}^{\infty} \left|\tilde{\psi}\right|^2 d\nu} = \frac{S_e(\nu_0)}{S(\nu_0)}. \tag{E.8}$$

E.2 Derivation of the Autocorrelation Matrix in Relation to $\hat{\rho}$

Consider a single photon which can occupy any single time bin. We write the state of a photon occupying a given time bin in terms of the creation operator:

$$\hat{a}_i^\dagger \ldots |0\rangle_{i-1} |0\rangle_i |0\rangle_{i+1} \ldots = \ldots \sqrt{1} |0\rangle_{i-1} |1\rangle_i |0\rangle_{i+1} \ldots \equiv |i\rangle . \tag{E.9}$$

The corresponding annihilation operator is defined similarly. We can then write the quadrature operator for a given temporal mode as:

$$\hat{X}_i = \frac{\hat{a}_i + \hat{a}_i^\dagger}{\sqrt{2}}. \tag{E.10}$$

For simplicity, we write two photons in a given mode as $|2_i\rangle$ and no photons in any mode as $|\bar{0}\rangle$. Combining the homodyne relation (3.1) with the auto-correlation current (5.19), we assume perfect detector resolution and find,:

$$\begin{aligned} A_{ij} &\propto \left\langle \hat{X}_i \hat{X}_j \right\rangle \\ &= \mathrm{Tr}\left[\sum_{m,n} \rho_{mn} |m\rangle\langle n| \hat{X}_i \hat{X}_j \right] \\ &= \sum_{m,n,k} \rho_{mn} \langle k|m\rangle \langle n| \hat{X}_i \hat{X}_j |k\rangle \\ &= \sum_{m,n} \rho_{mn} \langle n| \hat{X}_i \hat{X}_j |m\rangle \end{aligned} \tag{E.11}$$

We then need to compute the term $\langle n| \hat{X}_i \hat{X}_j |m\rangle$. Since $\langle n|m\rangle = \delta_{mn}$, many terms will not contribute to the sum:

$$\begin{aligned} \langle n| \hat{X}_i \hat{X}_j |m\rangle &= \frac{1}{\sqrt{2}} \langle n| \hat{X}_i \left[\delta_{jm} |0\rangle + \sqrt{2}\delta_{jm} |2_m\rangle + (1-\delta_{jm}) |jm\rangle \right] \\ &= \frac{1}{2} \langle n| \left[\delta_{jm} |i\rangle + 2\delta_{im}\delta_{jm} |m\rangle + (1-\delta_{jm})(\delta_{ij} |m\rangle + \delta_{im} |j\rangle) \right] \\ &= \frac{1}{2} \left(\delta_{jm}\delta_{ni} + 2\delta_{im}\delta_{jm}\delta_{nm} + (1-\delta_{jm})(\delta_{ij}\delta_{mn} + \delta_{im}\delta_{jn}) \right) \\ &= \frac{1}{2} \left(\delta_{jm}\delta_{ni} + 2\delta_{im}\delta_{jm}\delta_{nm} + \delta_{ij}\delta_{mn} + \delta_{im}\delta_{jn} - \delta_{jm}\delta_{ij}\delta_{mn} - \delta_{jm}\delta_{im}\delta_{jn} \right) \end{aligned} \tag{E.12}$$

We can then proceed with the sum (E.11):

$$\sum_{m,n} \rho_{mn} \langle n| \hat{X}_i \hat{X}_j |m\rangle = \tag{E.13}$$
$$\frac{1}{2} \sum_{m,n} (\delta_{jm}\delta_{ni}\rho_{mn} + 2\delta_{im}\delta_{jm}\delta_{nm}\rho_{mn} + \delta_{ij}\delta_{mn}\rho_{mn} + \delta_{im}\delta_{jn}\rho_{mn} - \delta_{jm}\delta_{ij}\delta_{mn}\rho_{mn} - \delta_{jm}\delta_{im}\delta_{jn}\rho_{mn}) =$$
$$\frac{1}{2} \sum_{n} (\delta_{ni}\rho_{jn} + 2\delta_{ij}\delta_{nj}\rho_{jn} + \delta_{ij}\rho_{nn} + \delta_{jn}\rho_{in} - \delta_{ij}\delta_{jn}\rho_{jn} - \delta_{ij}\delta_{jn}\rho_{jn}) =$$
$$\frac{1}{2} (\rho_{ji} + 2\delta_{ij}\rho_{jj} + \delta_{ij}\mathrm{Tr}\,[\hat{\rho}] + \rho_{ij} - \delta_{ij}\rho_{jj} - \delta_{ij}\rho_{jj}) =$$
$$\frac{\rho_{ij} + \rho_{ji}}{2} + \frac{1}{2}\delta_{ij}.$$

Since the density matrix is self-adjoint, $\rho_{ij} + \rho_{ji} = 2\mathrm{Re}\,[\rho_{ij}]$. Thus

$$\hat{A} \propto \mathrm{Re}\,[\hat{\rho}] + \frac{1}{2}\mathbb{1}, \tag{E.14}$$

with the constant of proportionality given by the electronic transfer function of the homodyne detector.

Bibliography

[1] D. A. Steck. Rubidium 85 D Line Data (revision 2.1.4, 23 December 2010). `http://steck.us/alkalidata`.

[2] W. E. Lamb. Anti-Photon. *Applied Physics B: Lasers and Optics*, 60:77–84, 1995. 10.1007/BF01135846.

[3] A. Einstein, B. Podolsky, and N. Rosen. Can Quantum-Mechanical Description of Physical Reality Be Considered Complete? *Phys. Rev.*, 47:777–780, May 1935.

[4] J. F. Clauser, M. A. Horne, A. Shimony, and R. A. Holt. Proposed Experiment to Test Local Hidden-Variable Theories. *Phys. Rev. Lett.*, 23:880–884, October 1969.

[5] A. Aspect, P. Grangier, and G. Roger. Experimental Tests of Realistic Local Theories via Bell's Theorem. *Phys. Rev. Lett.*, 47:460–463, August 1981.

[6] R. Hanbury Brown and R. Q. Twiss. Correlation between Photons in two Coherent Beams of Light. *Nature*, 177(4497):27–29, January 1956.

[7] C. K. Hong, Z. Y. Ou, and L. Mandel. Measurement of Subpicosecond Time Intervals Between Two Photons by Interference. *Phys. Rev. Lett.*, 59:2044–2046, November 1987.

[8] A. Elitzur and L. Vaidman. Quantum Mechanical Interaction-Free Measurements. *Foundations of Physics*, 23:987–997, 1993. 10.1007/BF00736012.

[9] M. D. Reid and P. D. Drummond. Quantum Correlations of Phase in Nondegenerate Parametric Oscillation. *Phys. Rev. Lett.*, 60:2731–2733, June 1988.

[10] D. J. Wineland, J. J. Bollinger, W. M. Itano, F. L. Moore, and D. J. Heinzen. Spin Squeezing and Reduced Quantum Noise in Spectroscopy. *Phys. Rev. A*, 46:R6797–R6800, December 1992.

[11] J. Abadie *et al.* A Gravitational Wave Observatory Operating Beyond the Quantum Shot-Noise Limit. *Nature Physics*, 7(12):962–965, September 2011.

[12] G. Moore. Cramming More Components Onto Integrated Circuits. *Electronics*, 38(8), April 1965.

[13] R. P. Feynman. Simulating Physics with Computers. *International Journal of Theoretical Physics*, 21:467–488, 1982. 10.1007/BF02650179.

[14] M. A. Nielsen and I. L. Chuang. *Quantum Computation and Quantum Information*. Cambridge Series on Information and the Natural Sciences. Cambridge University Press, 2000.

[15] A. MacRae, G. Campbell, and A. I. Lvovsky. Matched Slow Pulses Using Double Electromagnetically Induced Transparency. *Opt. Lett.*, 33(22):2659–2661, November 2008.

[16] C. K. Hong and L. Mandel. Experimental Realization of a Localized One-Photon State. *Phys. Rev. Lett.*, 56:58–60, January 1986.

[17] P. G. Kwiat, K. Mattle, H. Weinfurter, A. Zeilinger, A. V. Sergienko, and Y. Shih. New High-Intensity Source of Polarization-Entangled Photon Pairs. *Phys. Rev. Lett.*, 75:4337–4341, December 1995.

[18] Enrico Pomarico, Bruno Sanguinetti, Nicolas Gisin, Robert Thew, Hugo Zbinden, Gerhard Schreiber, Abu Thomas, and Wolfgang Sohler. Waveguide-based opo source of entangled photon pairs. *New Journal of Physics*, 11(11):113042, 2009.

[19] A. I. Lvovsky, H. Hansen, T. Aichele, O. Benson, J. Mlynek, and S. Schiller. Quantum State Reconstruction of the Single-Photon Fock State. *Phys. Rev. Lett.*, 87:050402, July 2001.

[20] J. S. Neergaard-Nielsen, B. M. Nielsen, H. Takahashi, A. I. Vistnes, and E. S. Polzik. High Purity Bright Single Photon Source. *Optics express*, 15(13):7940–9, June 2007.

[21] H. Zhang, X.-M. Jin, J. Yang, H.-N. Dai, S.-J. Yang, T.M. Zhao, J. Rui, Y. He, X. Jiang, F. Yang, G.-S. Pan, Z.-S. Yuan, Y. Deng, Z.-B. Chen, X.-H. Bao, S. Chen, B. Zhao, and J.-W. Pan. Preparation and Storage of Frequency-Uncorrelated Entangled Photons from Cavity-Enhanced Spontaneous Parametric Downconversion. *Nature Photonics*, 5(October):628–632, 2011.

[22] J. Fan and A. Migdall. A Broadband High Spectral Brightness Fiber-Based Two-Photon Source. *Opt. Express*, 15(6):2915–2920, March 2007.

[23] A. Ulhaq, S. Weiler, S. M. Ulrich, M. Rossbach, R. Jetter, and P. Michler. Cascaded Single-Photon Emission from the Mollow Triplet Sidebands of a Quantum Dot. *Nature Photonics*, 6:238 – 242, 2012.

[24] R. E. Slusher, L. W. Hollberg, B. Yurke, J. C. Mertz, and J. F. Valley. Observation of Squeezed States Generated by Four-Wave Mixing in an Optical Cavity. *Phys. Rev. Lett.*, 56:788–788, February 1986.

[25] L.-A. Wu, H. J. Kimble, J. L. Hall, and H. Wu. Generation of Squeezed States by Parametric Down Conversion. *Phys. Rev. Lett.*, 57:2520–2523, November 1986.

[26] C. H. van der Wal, M. D. Eisaman, A. Andre, R. L. Walsworth, D. F. Phillips, A. S. Zibrov, and M. D. Lukin. Atomic Memory for Correlated Photon States. *Science*, 301(5630):196–200, 2003.

[27] A. Kuzmich, W. P. Bowen, A. D. Boozer, A Boca, C. W. Chou, L-M Duan, and H. J. Kimble. Generation of Nonclassical Photon Pairs for Scalable Quantum Communication with Atomic Ensembles. *Nature*, 423(6941):731–4, June 2003.

[28] P. Kolchin. Electromagnetically-Induced-Transparency-Based Paired Photon Generation. *Phys. Rev. A*, 75:033814, March 2007.

[29] S. Du, P. Kolchin, C. Belthangady, G. Y. Yin, and S. E. Harris. Subnatural Linewidth Biphotons with Controllable Temporal Length. *Phys. Rev. Lett.*, 100:183603, May 2008.

[30] J. K. Thompson, J. Simon, H. Loh, and V. Vuletič. A High-Brightness Source of Narrowband, Identical-Photon Pairs. *Science*, 313(5783):74–77, 2006.

[31] C. F. McCormick, V. Boyer, E. Arimondo, and P. D. Lett. Strong Relative Intensity Squeezing by Four-Wave Mixing in Rubidium Vapor. *Optics letters*, 32(2):178–80, January 2007.

[32] V. Boyer, A. M. Marino, R. C. Pooser, and P. D. Lett. Entangled Images from Four-Wave Mixing. *Science*, 321(5888):544–547, 2008.

[33] A. I. Lvovsky and M. G. Raymer. Continuous-Variable Optical Quantum-State Tomography. *Rev. Mod. Phys.*, 81:299–332, March 2009.

[34] T. Fernholz, H. Krauter, K. Jensen, J. F. Sherson, A. S. Sørensen, and E. S. Polzik. Spin Squeezing of Atomic Ensembles via Nuclear-Electronic Spin Entanglement. *Phys. Rev. Lett.*, 101:073601, August 2008.

[35] J. Appel, E. Figueroa, D. Korystov, M. Lobino, and A. I. Lvovsky. Quantum Memory for Squeezed Light . *Physical Review Letters*, 100(9):093602 (4), March 2008.

[36] E. Bimbard, N. Jain, A. MacRae, and A. I. Lvovsky. Quantum-Optical State Engineering up to the Two-Photon Level. *Nature Photonics*, 4(April):243–247, 2010.

[37] T. Opatrný, N. Korolkova, and G. Leuchs. Mode Structure and Photon Number Correlations in Squeezed Quantum Pulses. *Phys. Rev. A*, 66:053813, November 2002.

[38] R. de la Madrid. The Role of the Rigged Hilbert Space in Quantum Mechanics. *European Journal of Physics*, 26(2):287, 2005.

[39] U. Leonhardt. *Measuring the Quantum State of Light*. Cambridge University Press, 1997.

[40] E. Schrödinger. Der Stetige Übergang von der Mikro- zur Makromechanik. *Naturwissenschaften*, 14:664–666, 1926.

[41] R.J. Glauber. Coherent and Incoherent States of Radiation Field. *Phys. Rev.*, 131:2766–2788, 1963.

[42] F. T. Arecchi. Measurement of the Statistical Distribution of Gaussian and Laser Sources. *Phys. Rev. Lett.*, 15:912–916, December 1965.

[43] K. Mølmer. Optical Coherence: A Convenient Fiction. *Phys. Rev. A*, 55:3195–3203, April 1997.

[44] T. Rudolph and B. C. Sanders. Requirement of Optical Coherence for Continuous-Variable Quantum Teleportation. *Phys. Rev. Lett.*, 87:077903, July 2001.

[45] H.-A. Bachor and T. C. Ralph. *A Guide to Experiments in Quantum Optics, Second Ed.* Wiley, 2005.

[46] W. Vogel and D.-G. Welsch. Ch. 3: Quantum States of Bosonic Systems. In *Quantum Optics*, pages 100–103. Wiley, 2001.

[47] E. Wigner. On the Quantum Correction For Thermodynamic Equilibrium. *Phys. Rev.*, 40:749–759, June 1932.

[48] E. C. G. Sudarshan. Equivalence of Semiclassical and Quantum Mechanical Descriptions of Statistical Light Beams. *Phys. Rev. Lett.*, 10:277–279, April 1963.

[49] L. Mandel and E. Wolf. Ch. 11: Coherent states of the electromagnetic field. In *Optical Coherence and Quantum Optics*, pages 540–555. Cambridge University Press, 1995.

[50] R. Daendliker. The Concept of Modes in Optics and Photonics. *Proceedings of the Sixth International Conference on Education and Training in Optics and Photonics*, 3831:193–198, 2000.

[51] C. Gerry and P. Knight. *Introductory Quantum Optics*. Cambridge University Press, 2005.

[52] G. Orwell. *Animal Farm*. Secker and Warburg (London), 1945.

[53] M. Hillery. Classical Pure States Are Coherent States. *Phys. Lett. A*, 111:409–411, October 1985.

[54] X. T. Zou and L. Mandel. Photon-Antibunching and Sub-Poissonian Photon Statistics. *Phys. Rev. A*, 41:475–476, January 1990.

[55] Y. Takeno, M. Yukawa, H. Yonezawa, and A. Furusawa. Observation of -9 dB Quadrature Squeezing with Improvement of Phase Stability in Homodyne Measurement. *Opt. Express*, 15(7):4321–4327, April 2007.

[56] P. Hobbs. *Building Electro-Optical Systems: Making It All Work*. Wiley, 2000.

[57] M. B. Gray, D. A. Shaddock, C. C. Harb, and H.-A. Bachor. Photodetector Designs for Low-Noise, Broadband, and High-Power Applications. *Review of Scientific Instruments*, 69(11):3755–3762, 1998.

[58] H.-P. Yuen and V.-W.-S. Chan. Noise in Homodyne and Heterodyne Detection. *Opt. Lett.*, 8(3):177–179, March 1983.

[59] R. Kumar, E. Barrios, A. MacRae, E. Cairns, E. Huntington, and A. I. Lvovsky. Versatile Wideband Balanced Detector for Quantum Optical Homodyne Tomography. *Arχiv [physics.ins-det]*, 1111.4012, November 2011.

[60] G. T. Herman. *Image Reconstruction From Projections: The Fundamentals of Computerized Tomography*. Academic Press, 1980.

[61] D. T. Smithey, M. Beck, M. G. Raymer, and A. Faridani. Measurement of the Wigner Distribution and the Density Matrix of a Light Mode Using Optical Homodyne Tomography: Application to Squeezed States and the Vacuum. *Phys. Rev. Lett.*, 70:1244–1247, March 1993.

[62] U. Leonhardt and M. G. Raymer. Observation of Moving Wave Packets Reveals Their Quantum State. *Phys. Rev. Lett.*, 76:1985–1989, March 1996.

[63] J. .S. Neergaard-Nielsen. *Generation Oo Single Photons and Schrödinger Kitten States of Light*. PhD thesis, University of Copenhagen, July 2008.

[64] K. B. Petersen and M. S. Pederson. The Matrix Cookbook. `http://matrixcookbook.com`.

[65] J. Reháček, Z. Hradil, E. Knill, and A. I. Lvovsky. Diluted Maximum-Likelihood Algorithm for Quantum Tomography. *Physical Review A*, 75(4):1–5, April 2007.

[66] A. M. Marino, R. C Pooser, V. Boyer, and P. D. Lett. Tunable Delay of Einstein-Podolsky-Rosen Entanglement. *Nature*, 457:859–862, February 2009.

[67] E. Hecht. *Optics, fourth ed.* Addison Wesley, 2002.

[68] R. W. Boyd. *Nonlinear Optics, third ed.* Academic Press, 2008.

[69] C. W Thiel. Four-Wave Mixing and its Applications. `http://www.physics.montana.edu/students/thiel/docs/FWMixing.pdf`.

[70] A. MacRae. Double Electromagnetically Induced Transparency. Master's thesis, University of Calgary, August 2008.

[71] R. Y. Chiao, E. Garmire, and C. H. Townes. Self-Trapping of Optical Beams. *Phys. Rev. Lett.*, 13:479–482, October 1964.

[72] Q. Glorieux, L. Guidoni, S. Guibal, J.-P. Likforman, and T. Coudreau. Strong Quantum Correlations in Four Wave Mixing in ^{85}Rb Vapor. volume 7727, page 772703. SPIE, 2010.

[73] M. Hosseini, G. Campbell, B. M. Sparkes, P. K. Lam, and B. C. Buchler. Unconditional Room-Temperature Quantum Memory. *Nature Physics*, 7(March):794–798, 2011.

[74] L. Barbier and M. Cheret. Energy Pooling Process in Rubidium Vapour. *Journal of Physics B: Atomic and Molecular Physics*, 16(17):3213, 1983.

[75] A. M. Akulshin, R. J. McLean, A. I. Sidorov, and P. Hannaford. Coherent and Collimated Blue Light Generated by Four-Wave Mixing in Rb Vapour. *Opt. Express*, 17(25):22861–22870, December 2009.

[76] A. Vernier, S. Franke-Arnold, E. Riis, and A. S. Arnold. Enhanced frequency up-conversion in rb vapor. *Opt. Express*, 18(16):17020–17026, August 2010.

[77] A. Heidmann, R. J. Horowicz, S. Reynaud, E. Giacobino, C. Fabre, and G. Camy. Observation of Quantum Noise Reduction on Twin Laser Beams. *Phys. Rev. Lett.*, 59:2555–2557, November 1987.

[78] V. Boyer, A. M. Marino, and P. D. Lett. Generation of Spatially Broadband Twin Beams for Quantum Imaging. *Phys. Rev. Lett.*, 100:143601, April 2008.

[79] P. H. Souto Ribeiro, C. Schwob, A. Maître, and C. Fabre. Sub-Shot-Noise High-Sensitivity Spectroscopy with Optical Parametric Oscillator Twin Beams. *Opt. Lett.*, 22(24):1893–1895, December 1997.

[80] J. Gao, F. Cui, C. Xue, C. Xie, and P. Kunchi. Generation and Application of Twin Beams From an Optical Parametric Oscillator Including an α-cut KTP Crystal. *Opt. Lett.*, 23(11):870–872, June 1998.

[81] M. Jasperse, L. D. Turner, and R. E. Scholten. Relative Intensity Squeezing by Four-Wave Mixing With Loss: an Analytic Model and Experimental Diagnostic. *Opt. Express*, 19(4):3765–3774, February 2011.

[82] J. Appel, A. MacRae, and A. I. Lvovsky. A Versatile Digital GHz Phase Lock for External Cavity Diode Lasers. *Measurement Science and Technology*, 20(5):055302, May 2009.

[83] O. Okusaga, J. Cahill, and W. Zhou. Optical Fiber Induced Noise in RF-photonic Links. In *Avionics, Fiber- Optics and Photonics Technology Conference (AVFOP), 2011 IEEE*, pages 55 –56, October 2011.

[84] W. Wasilewski, A. I. Lvovsky, K. Banaszek, and C. Radzewicz. Pulsed Squeezed Light: Simultaneous Squeezing of Multiple Modes. *Phys. Rev. A*, 73:063819, June 2006.

[85] D. N. Klyshko. Two-Photon Light: Influence of Filtration and a New Possible EPR Experiment. *Physics Letters A*, 128(3):133–137, 1988.

[86] D. N. Klyshko. Combined EPR and Two-Slit Experiments: Interference of Advanced Waves. *Physics Letters A*, 132(6):299–304, 1988.

[87] D. Marcuse. Gaussian Approximation of the Fundamental Modes of Graded-Index Fibers. *J. Opt. Soc. Am.*, 68(1):103–109, January 1978.

[88] H. Kogelnik and T. Li. Laser Beams and Resonators. *Appl. Opt.*, 5(10):1550–1567, October 1966.

[89] M. Hercher. The Spherical Mirror Fabry-Perot Interferometer. *Appl. Opt.*, 7(5):951–966, May 1968.

[90] Gorachand Ghosh. Sellmeier Coefficients and Dispersion of Thermo-Optic Coefficients for Some Optical Glasses. *Appl. Opt.*, 36(7):1540–1546, March 1997.

[91] M. Buckland. *AI Techniques for Game Programming*. The Premier Press Game Development Series. Premier Press, 2002.

[92] C. Darwin and G. Beer. *The Origin of Species*. Oxford World's Classics. Oxford University Press, 1859,1998.

[93] R. J. Barlow. *Statistics: A Guide to the Use of Statistical Methods in the Physical Sciences*. Wiley, 1989.

[94] S. R. Huisman, N. Jain, S. A. Babichev, F. Vewinger, A.-N. Zhang, S.-H. Youn, and A. I. Lvovsky. Instant Single-Photon Fock State Tomography. *Optics Letters*, 34(18):2739 – 2741, September 2009.

[95] M. D. Eisaman, J. Fan, A. Migdall, and S. V. Polyakov. Invited Review Article: Single-Photon Sources and Detectors. *Review of Scientific Instruments*, 82(7):071101, 2011.

[96] C. W. Chou, S. V. Polyakov, A. Kuzmich, and H. J. Kimble. Single-Photon Generation from Stored Excitation in an Atomic Ensemble. *Phys. Rev. Lett.*, 92:213601, May 2004.

[97] D. N. Matsukevich, T. Chanelière, S. D. Jenkins, S.-Y. Lan, T. A. B. Kennedy, and A. Kuzmich. Deterministic Single Photons via Conditional Quantum Evolution. *Phys. Rev. Lett.*, 97:013601, July 2006.

[98] J. McKeever, A. Boca, A. D. Boozer, R. Miller, J. R. Buck, A. Kuzmich, and H. J. Kimble. Deterministic Generation of Single Photons from One Atom Trapped in a Cavity. *Science*, 303(5666):1992–1994, 2004.

[99] M. Hijlkema, B. Weber, H. P. Specht, A. Webster, S. C. Kuhn, and G. Rempe. Unconditional Room-Temperature Quantum Memory. *Nature Physics*, 3(March):253–255, 2007.

[100] A. Bennett, D. Unitt, P. Atkinson, D. Ritchie, and A. Shields. High Performance Single Photon Sources from Photolithographically Defined Pillar Microcavities. *Opt. Express*, 13(1):50–55, January 2005.

[101] T. Zhong, X. Hu, F. N. C. Wong, K. K. Berggren, T. D. Roberts, and P. Battle. High-Quality Fiber-Optic Polarization Entanglement Distribution at 1.3 μm Telecom Wavelength. *Opt. Lett.*, 35(9):1392–1394, May 2010.

[102] Q. Wang, W. Chen, G. Xavier, M. Swillo, T. Zhang, S. Sauge, M. Tengner, Z.-F. Han, G.-C. Guo, and A. Karlsson. Experimental Decoy-State Quantum Key

Distribution with a Sub-Poissionian Heralded Single-Photon Source. *Phys. Rev. Lett.*, 100:090501, March 2008.

[103] A. Ling, J. Chen, J. Fan, and A. Migdall. Mode Expansion and Bragg Filtering for a High-Fidelity Fiber-Based Photon-Pair Source. *Opt. Express*, 17(23):21302–21312, November 2009.

[104] A. MacRae, T. Brannan, R. Achal, and A. I. Lvovsky. Tomography of a high-purity narrowband photon from a transient atomic collective excitation. *Phys. Rev. Lett.*, 109:033601, Jul 2012.

[105] M. Scholz, L. Koch, and O. Benson. Statistics of Narrow-Band Single Photons for Quantum Memories Generated by Ultrabright Cavity-Enhanced Parametric Down-Conversion. *Physical Review Letters*, 102(6):1–4, February 2009.

[106] M. Halder, A. Beveratos, R. Thew, C. Jorel, H. Zbinden, and N. Gisin. High Coherence Photon Pair Source for Quantum Communication. *New Journal of Physics*, 10(2):023027, February 2008.

[107] N. Jain. Quantum Optical State Engineering at the Few-Photon Level. Master's thesis, University of Calgary, October 2009.

[108] D. Berry, A. I. Lvovsky, and B. C. Sanders. Interconvertibility of single-rail optical qubits. *Optics letters*, 31(1):107–9, January 2006.

[109] L. M. Duan, M. D. Lukin, J.I. Cirac, and P. Zoller. Long-Distance Quantum Communication with Atomic Ensembles and Linear Optics. *Nature*, 414(6862):413–8, November 2001.

[110] N. Sangouard, C. Simon, H. de Riedmatten, and N. Gisin. Quantum Repeaters Based on Atomic Ensembles and Linear Optics. *Review of Modern Physics*,

83(1):33–80, March 2011.

[111] Z.-B. Wang, K.-P. Marzlin, and B. C. Sanders. Large Cross-Phase Modulation Between Slow Co-Propagating Weak Pulses in ^{87}Rb. *Physical Review Letters*, 97(6):063901 (4), August 2006.

[112] Peter Milonni and Joseph Eberly. *Lasers*. Wiley, 1988.